5-2019

Micro- to Macro-Scale Structural and Lithological Architecture of Basal Nonconformities: Implications for Fluid Flow and Injection Induced Seismicity

Garth Hesseltine
Utah State University

MICRO- TO MACRO-SCALE STRUCTURAL AND LITHOLOGICAL ARCHITECTURE OF BASAL NONCONFORMITIES: IMPLICATIONS FOR FLUID FLOW AND INJECTION INDUCED SEISMICITY

by

Garth Hesseltine

A thesis submitted in partial fulfilment
of the requirements for the degree

of

MASTER OF SCIENCE

in

Geology

Approved:

_____	_____
James P. Evans, Ph.D. Major Professor	Kelly K. Bradbury, Ph.D. Committee Member
_____	_____
Anthony R. Lowry, Ph.D. Committee Member	Richard S. Inouye, Ph.D. Vice Provost for Graduate Studies

UTAH STATE UNIVERSITY
Logan, Utah

2019

ABSTRACT

Micro- to Macro-Scale Structural and Lithological Architecture of Basal Nonconformities: Implications for Fluid Flow and Injection Induced Seismicity

by

Garth Hesseltine, Master of Science

Utah State University, 2019

Major Professor: Dr. James P. Evans
Department: Geology

Rising incidents of induced seismicity in the United States, related to the injection of wastewater into sedimentary rocks in the subsurface, is a growing concern. Induced earthquakes generally nucleate along faults in Precambrian crystalline rocks within the continental crust, and understanding potential fluid pathways and/or barriers is crucial. I investigate the structure, lithology, and heterogeneity of nonconformities and highlight their possible role in the transmission of fluids and pore-fluid pressures into the crystalline basement. Structural mapping, photogrammetry, X-ray diffraction mineralogy, X-ray fluorescence geochemistry, petrography, in-situ permeability, and characterization of weathering and rock strength classification studies were used to analyze, at microscopic to megascopic scales, rocks proximal to nonconformities in New Mexico, Colorado, and Michigan. Fracture maps were analyzed using the FracPaQ toolbox to estimate fracture-related permeability of the rocks.

The nonconformities observed in this study consist of variably deformed, weathered, and altered Precambrian igneous and metamorphic crystalline basement overlain by Paleozoic sedimentary rocks cut by outcrop- to map-scale faults. The nonconformity at the New Mexico sites includes a phyllosilicate-rich weathered horizon atop deformed crystalline basement. Heterogeneity observed in the fracture and joint networks within the crystalline basement contributes to permeability heterogeneity and anisotropy. The crystalline basement adjacent to the nonconformity at the Colorado site is relatively fresh and unweathered and overlain by low permeability sandstones. The nonconformity and underlying slates in the Michigan drillcore are overprinted by hydrothermal alteration and carbonate mineralization, which provides evidence of hydrological communication between sedimentary and crystalline basement rocks. The nonconformities display a range of structural, lithological, and geochemical styles and characteristics which vary over relatively small spatial extents. Hydrological models indicate nonconformity features observed in this study likely impact the way fluids behave proximal to nonconformities and the transmission of fluid and pore-fluid pressures into the crystalline basement. We identify features that may account for permeability heterogeneity and anisotropy proximal to nonconformities including the presence of a weathered horizon, faults, geomechanical and lithological disparities, and miscellaneous alteration and deformation structures.

(126 pages)

PUBLIC ABSTRACT

Micro- to Macro-Scale Structural and Lithological Architecture of Basal Nonconformities: Implications for Fluid Flow and Injection Induced Seismicity

Garth Hesseltine

Rising incidents of earthquakes caused by human activity in the United States, known as induced earthquakes, is a growing concern. Induced earthquakes may occur when fluid and/or wastewater is injected several kilometers beneath the Earth's surface into sedimentary rocks. Fluids and pressures can migrate from the sedimentary rocks, which are typically friendlier to fluid flow, into underlying less friendlier crystalline rocks along fluid pathways weakening and possibly reactivating preexisting faults. Understanding potential fluid pathways and/or barriers from the sedimentary rocks to crystalline rocks is crucial. I investigate the structure, composition, and heterogeneity of rocks near the contact between the sedimentary and crystalline rocks, known as nonconformities, and highlight their possible role in the transmission of fluids and pore-fluid pressures into the crystalline basement.

To characterize nonconformities, we examined outcrop analogs and drillcore of nonconformities in New Mexico, Colorado, and Michigan. Geochemical, structural, and hydrological techniques were used to analyze the nonconformities at microscopic to megascopic scales. The nonconformities observed in this study consist of variably deformed, weathered, and altered igneous and metamorphic crystalline basement overlain

by sedimentary rocks cut by outcrop- and map-scale faults. The nonconformity at the New Mexico sites includes a clay-rich weathered horizon atop deformed and jointed crystalline basement. Heterogeneity observed in the fracture and joint networks within the crystalline basement contributes to permeability heterogeneity and anisotropy. The crystalline basement adjacent to the nonconformity at the Colorado site is relatively fresh and unweathered and overlain by low permeability sandstones. The nonconformity and underlying slates in the Michigan drillcore are overprinted by hydrothermal alteration and carbonate mineralization, which provides evidence of hydrological communication between sedimentary and crystalline rocks. The nonconformities display a range of structural, hydrological, and geochemical styles and characteristics which vary over relatively small spatial extents. The geological and hydrogeological histories and complexities of nonconformity analogs provide valuable information to understand how fluids, past, and present, interact with the contact. This study introduces some of the factors that may control fluid flow adjacent to nonconformities and their possible significance to the interplay of deformation, fluid flow, and induced seismicity.

ACKNOWLEDGMENTS

This research was supported by the U.S. Geological Survey NEHRP Grant #2015-0137. This research was also supported by the GDL Foundation Fellowship, Utah State University's Geology Department J. Stewart Williams Graduate Fellowship, Geological Society of America Student Research grant, Utah State University's Graduate Research and Collaborative Opportunities Program grant, and Utah State University's Geology Department.

Garth Hesseltine

CONTENTS

Page

LIST OF TABLES

LIST OF FIGURES

INTRODUCTION

The structural and hydrological properties of sedimentary and crystalline rocks are typically studied as separate rock types and separate topics, and individually much is known (Brace, 1980; Lucia, 1983; Brace, 1984; Clauser, 1992; Nelson, 1994; Barton et al., 1995; Lucia, 1999; Nelson, 2009). However, there is a knowledge gap associated with our understanding of the mechanical and hydrologic behaviors of the sedimentary rock – crystalline rock basement interfaces, known as nonconformities. Our primary goal is to further our understanding of the structural and permeability architecture and heterogeneity of nonconformities and their influence on fluid pressure migration into the crystalline basement. The lack of data on the characteristics of nonconformities may affect hydro-geomechanical and numerical models of subsurface flow, which are crucial for applications in basal reservoir fluid injection, carbon sequestration, and induced seismicity (e.g., Zhang et al., 2013, 2016; Chang & Segall, 2017; Ortiz et al., 2018), and exploration of crystalline basement-rock hosted hydrocarbon and unconformity-type uranium deposits (Raffensperger & Garven, 1995; Cui et al., 2012). The objective of this research is to provide a fundamental geological, hydrological, and mechanical understanding of nonconformities. We utilized a multi-faceted approach that involved structural, hydrological, geomechanical, and geochemical techniques in characterizing and evaluating the rock properties and the interaction between mechanical, hydrological, and chemical processes proximal to the interface. We hypothesize that the hydrologic nature of nonconformities varies as a function of lithology, deformation, alteration, weathering, and mechanical properties.

I determine the structural, lithological, and hydrological architecture of the nonconformity zones of several sites by examining the nature of fluid-rock interactions and physical rock properties as proxies to understand better how these might affect modern day fluid flow (e.g., Ortiz et al., 2018). Exposures of altered nonconformities provide essential geological and hydrological analogs of rocks that may be encountered in the subsurface and of what may happen when concentrated fluids interact at the interface. We identified key stratigraphic units based on hydrological and geomechanical properties and developed conceptual geologic and permeability models. The structural and hydrological data will be central to a better understanding of the geological processes associated with induced seismicity, hydrocarbon accumulation in basement reservoirs, and uranium mineralization proximal to the sedimentary rock – crystalline basement interface.

BACKGROUND AND SIGNIFICANCE

Hydrogeological models of fluid injection and induced seismicity typically incorporate limited geological data from outcrop or laboratory studies to constrain the hydraulic properties of the rock. Modeling the interface as a thin, discrete boundary between two units may be an inadequate representation of nonconformity heterogeneities and their impacts on fluid flow. Nonconformities may exhibit a range of structural and lithological geometries and properties, and these might affect the nature of injection-related fluid flow proximal to and across the interface.

Induced Seismicity and the Importance of Nonconformities

Understanding the structural and hydrological properties of basal nonconformities is vital for several applications in basal reservoir fluid injection and carbon sequestration. Knowledge of the properties of the interface zone can help mitigate the risk of induced seismicity by assigning fundamental geomechanical properties to numerical flow models that are currently lacking necessary data (National Research Council, 2013; Ellsworth, 2013). Induced seismicity is a growing public concern, and has significantly increased in the U.S. (Ellsworth, 2013; Ellsworth et al., 2015), and studies have linked fluid injection with induced seismicity in Colorado, Oklahoma, Kansas, Texas, Arkansas, Ohio, California, New Mexico, Colorado, and Virginia (Healy et al., 1968; Frohlich, 2012; Horton, 2012; Kim, 2013; Keranen et al., 2013, 2014; Rubinstein et al., 2014; Walsh & Zoback, 2015; Ellsworth et al., 2015; Hornbach et al., 2015; Goebel et al., 2016). The U.S. Geological Survey seismic hazard forecast for the central and eastern United States, (Petersen et al., 2016), included for the first time hazards associated with induced

earthquakes. Models indicate that north central Oklahoma has a similar chance of experiencing damaging induced earthquakes as parts of California do from natural earthquakes (Petersen et al., 2016).

For injection to induce seismicity pore fluid pressures need to be transmitted to seismogenic faults (e.g., Healy et al., 1968; Shapiro & Dinske, 2009; Keranen et al., 2014), and/or the injection of fluids needs to alter the stress state acting on seismogenic faults through poroelastic (e.g., Deng et al., 2016), thermoelastic, and/or mass effects (Ellsworth, 2013; Rubinstein & Mahani, 2015). The Mohr-Coulomb failure criterion that likely models brittle fault reactivation is given by:

$$\tau_{crit} = \mu\sigma_n - P \qquad (1).$$

Where τ_{crit} is the shear stress, μ is the coefficient of internal friction, σ_n is the normal stress, and P is pore fluid pressure. Fault zones are typically envisioned as consisting of fault core, damage zone, and protolith with unique mechanical and hydrological properties (Chester & Logan, 1986; Caine et al., 1996; Evans et al., 1997). Faults can act as conduits and/or barriers to flow or conduit-barrier systems (Caine et al., 1996; Evans et al., 1997). In the brittle zone, the structural and permeability architecture of faults and fault zones are a primary control on fluid flow (Caine et al., 1996). We assume the crust is critically stressed (Townend & Zoback, 2000) and minor increases in pore fluid pressure along crystalline basement faults, resulting from fluid injection, can facilitate failure and reactivation of pre-existing structures (Horton, 2012; Keranen et al., 2013, 2014; Walsh & Zoback, 2015).

The magnitudes and orientations of the stresses play a critical role in determining which faults and fractures are barriers or conduits to flow (Min et al., 2004; Hennings et

al., 2012; Ranjram et al., 2015). Stress field orientation and magnitude are a primary control on which structures are optimally oriented, or structures that are oriented at an angle to the deviatoric stress field that favors Coulomb failure. In the Suban Gas Field in Indonesia, which consists primarily of carbonate and crystalline metamorphic rock reservoirs, the stress field orientation was the primary control on permeability and reservoir performance (Hennings et al., 2012). Fractures zones in the strike-slip stress regime, with high shear to normal stress ratio, had a higher permeability (Hennings et al., 2012). For increased pore-fluid pressures to reach crystalline basement faults and validate the reduced effective frictional strength mechanism, the fluids must cross from the sedimentary rocks into the crystalline basement traversing the nonconformity and related features along preexisting structures.

Role of Nonconformities in Resource Concentration

Unconformity-type uranium deposits and crystalline rock hosted hydrocarbon deposits shed light on the structural complexity, hydraulic interconnectivity, and permeability heterogeneity associated with basal nonconformities. Unconformity-type uranium deposits are some of the most significant and highest-grade uranium deposits in the world, primarily located in Canada and Australia, and account for approximately a third of the world's uranium resources (Jefferson et al., 2007). The uranium deposits are hosted in the crystalline basement and sedimentary units that straddle the nonconformity (Jefferson et al., 2007). Uranium-rich fluids circulating proximal to the interface reached reducing conditions facilitating uranium mineralization (Jefferson et al., 2007). The most extensive uranium deposits occur in the Athabasca Basin in Canada, where the

nonconformity is characterized by a regolith of variable thickness (Jefferson et al., 2007). Regolith, as defined by Pain et al. (1991), is bedrock which has been altered by processes at or near the surface. Similar to other unconformity-related mineral deposits, the Athabasca uranium deposits are commonly structurally controlled by faults that offset the basal nonconformity (Jefferson et al., 2007). These deposits are mainly concentrated near graphite-rich zones (Jefferson et al., 2007) that provide ideal reducing conditions for uranium precipitation (Hoeve & Sibbald, 1978).

Hydrocarbons hosted in fractured basement reservoirs result from the lateral migration of hydrocarbons through preferential pathways into structural basement highs or structural traps proximal to basal nonconformities (Gutmanis, 2009). The recently discovered Sverdrup field and related complexities in offshore Norway contain hydrocarbons that may have migrated several tens of km from the source rock through fractured basement highs (Jørstad, 2012; Hartz et al., 2013). The Sverdrup field is estimated to contain over one billion barrels of recoverable oil and includes recoverable hydrocarbon in fractured and weathered crystalline basement reservoirs (Jorstad, 2012; Hartz et al., 2013). Fractured and weathered crystalline basement hydrocarbon reservoirs are found throughout the world, including in the United States, China, Venezuela, Egypt, Vietnam, and the United Kingdom (Hubbert & Willis, 1955; Landes et al., 1960; Younes et al., 1998; Petford & McCaffrey, 2003; Cuong & Warren, 2009; Tong et al., 2012; Trice, 2014). Fracture networks in the crystalline basement are a primary control on reservoir performance (Trice, 2014).

Currently, we have an incomplete understanding of the hydromechanical properties of nonconformities and lack physical data required to provide constraints and

inputs for hydro-geomechanical models. Studying the hydrological heterogeneities and structural architecture of basal nonconformities, resulting from alteration, deformation, and paleoweathering, will help us understand the hydrologic connectivity of the basal reservoir and underlying crystalline basement, and the migration of fluids and pore pressures proximal to the interface, and provide insight on critical geological processes. Inadequate knowledge of the subsurface structure and conditions during fluid injection projects may lead to underestimates of the risk of pore-fluid pressure transmission into the crystalline basement and induced seismicity. Detailed studies on the geological and hydrogeological architectures of nonconformities in the Mid-Continental US provide valuable information to understand how fluids, past, and present, interact with the nonconformity.

Research Questions

To further our understanding of the structural and permeability architecture of nonconformities and the processes and controls on injection-related seismicity, and the development of resources that accumulate at or near nonconformities, I address four primary questions in this thesis.

- What are some of the structural and permeability architectures of nonconformities that may be encountered in the subsurface? What impacts do lithology, geometry, deformation, alteration, and weathering have on the properties and nature of the nonconformity?
- What are the permeability anisotropies of nonconformities and how do they vary in magnitude and scale?
- Does the presence of a weathered horizon at the interface affect the hydrogeological properties? What are the dominant features and characteristics of the weathered horizon and what are the root-shape features extending from the interface into the regolith? Is the weathered horizon overprinted by subsequent alteration associated with fluid flow, and/or diagenesis?
- What role have fluids had in alteration of the rocks proximal to nonconformities? What insights can be gleaned from these alterations about fluid interaction at the interface?

METHODS

To characterize the nonconformity zone, we combine structural, sedimentological, geochemical, geomechanical, and hydrological techniques to evaluate controls on permeability and hydraulic connectivity of the basal reservoir and underlying crystalline basement rock. Field sites and whole-rock drill cores were selected to encompass a wide variety of structural and lithological features. Outcrops were chosen where the basal contact between sedimentary rock and crystalline rock were well exposed. Our objective was to utilize outcrops and drillcore to determine possible scenarios that may be encountered in the subsurface. A combination of field and laboratory work was done to characterize the nonconformity and the deformation and alteration features (e.g., faults and fractures) that transverse the interface at microscopic to megascopic scales. I examine the influence of these factors on the nature of the nonconformity.

Field Methods

Fieldwork was focused in the Rocky Mountain region, which is an ideal study area because of the abundance of well-exposed nonconformity outcrops, drillcore availability, and the variability of the rocks above and below the contact. Our main field site is located west of Las Vegas, New Mexico in the Sangre de Cristo Mountains. The nonconformity lies adjacent to New Mexico State Route 65 for approximately 5 km and is well-exposed in several localities (Kerner, 2015; Lindline et al., 2015; Hesseltine et al., 2016). The nonconformity includes an undulating contact and regolith horizon, a variety of deformation and alteration structures, and a range of protoliths (Kerner, 2015; Lindline et al., 2015; Hesseltine et al., 2016). Our second field site north of Durango, Colorado

consists of a relatively undeformed and unaltered contact with the Devonian Ignacio Formation overlying the Precambrian Baker's Bridge Granite. We sampled rock across and adjacent to the interface for laboratory analysis. Additionally, we examined four drillcores that cut a sedimentary rock - Precambrian slate interface, which were acquired in a mineral exploration project in the western Upper Peninsula of Michigan.

Localities were selected based on lithology, structure, alteration, and deformation features. Samples encompassed the full range of alteration and diagenetic features (e.g., silicification, authigenic and clay mineralogy, weathering, bleaching, and mineral precipitation and dissolution) and deformation features (e.g., faults, fractures, deformation bands, fault cores, damage zones, fault gouges, slickenlines, cataclasites, foliations, and deformation bands) observed proximal to the interface. In New Mexico, samples were chosen to encompass the full range of weathering observed in the crystalline basement rock.

Photographs were taken at multiple scales for image analysis. Images in the field were printed using a portable printer to allow mapping of structural features and sample locations in the field. Outcrop-scale structural mapping, photogrammetry, and horizontal and vertical fault and fracture transects were used to characterize fault and fracture geometry, connectivity, orientation, density, deformation, mineralization, and morphology. Fracture maps were constructed at multiple stations, to capture interface heterogeneity. In-situ rock properties at analog field sites including the degree of weathering and alteration and strength of rock were determined using the classification systems from International Society for Rock Mechanics Commission on Standardization of Laboratory and Field Tests (1978) (Table 1a-c). At the Durango site, in-situ rock

Table 1 Weathering and strength classification systems. (From ISRM Commission on Standardization of Laboratory and Field Tests, 1978). **(A)** Degree of weathering and alteration. **(B)** Rock strength grade and estimation of uniaxial compressive strength. **(C)** Weathering terminology.

Term	Description	Grade
Fresh	No visible sign of rock material weathering; perhaps slight discoloration on major discontinuity surfaces.	I
Slightly Weathered	Discoloration indicates weathering of rock material and discontinuity surfaces. All the rock material may be discolored by weathering and may be somewhat weaker externally than in its fresh condition.	II
Moderately Weathered	Less than half of the rock material is decomposed and/or disintegrated to a soil. Fresh or discolored rock is present either as continuous framework or as corestones	III
Highly Weathered	More than half of the rock material is decomposed and/or disintegrated to a soil. Fresh or discolored rock is present either as a discontinuous framework or as corestones.	IV
Completely Weathered	All rock material is decomposed and/or disintegrated to soil. The original mass structure is still largely intact.	V
Residual Soil	All rock material is converted to soil. The mass structure ad material fabric are destroyed. There is a large change in volume, but the soil has not been significantly transported.	VI

Description	Field Identification	Grade	Approx. range of uniaxial compressive strength (Mpa)
Extremely weak rock	Indented by thumbnail	R0	0 - 1.0
Very weak rock	Crumbles under firm blows with point of geological hammer, can be peeled by a pocket knife	R1	1.0 - 5.0
Weak rock	Can be peeled by a pocket knife with difficulty, shallow indentions made by firm blow with point of geological hammer	R2	5.0 - 25
Medium strong rock	Cannot be peeled with a pocket knife, specimen can be fractured with a single firm blow of geological hammer	R3	25 - 50
Strong rock	Specimen requires more than one blow of geological hammer to fracture it	R4	50 - 100
Very strong rock	Specimen requires many blows of geological hammer yo fracture it	R5	100 - 250
Extremely strong rock	specimen can only be chipped with geological hammer	R6	> 250

Term	Description
Fresh	No visible sign of weathering of the rock material
Discolored	The color of the original fresh rock material is changed
Decomposed	The rock is weathered to the condition of soil in which the original material fabric is still intact, but some or all of the mineral grains are decomposed
Disintegrated	The rock is weathered o the condition of soil in which material fabric is still intact. The rock is friable, but the mineral grains are not decomposed

permeability of the overlying sedimentary rock was determined and calculated using a TinyPerm II Portable Air Permeameter, and the associated permeability calibration given by:

$$\mathrm{K} = \exp\text{^}\frac{T-12.8737}{-0.8206} \qquad (2).$$

Where *T* is the TinyPerm II value, and *K* is permeability in millidarcy (mD). A total of five TinyPerm *T* measurements were taken at each location, and high and average *T* and *K* were recorded and calculated. The permeability values obtained with the TinyPerm II Portable Air Permeameter were below the recommended minimum threshold for the provided calibrated conversion factors; however, they are still included in the results.

Laboratory Methods

Petrographic, geochemical, and structural analyses on core and field samples were used to characterize structural, lithological, weathering, and alteration features proximal to the interface at microscopic to megascopic scales. A combination of X-Ray powder diffraction (XRD), and handheld X-ray fluorescence (XRF) was used to determine the compositional and mineralogical variations of the rocks across and adjacent to the interface. Field and core samples were photographed with a color chart and scale. Representative samples were slabbed and examined to optimize sampling for analysis.

Petrographical and Mineralogical Analyses

A Leica DM2700 microscope with 5x, 10x, 20x, and 63x objectives was used for thin section petrography to evaluate mineralogy, clay and authigenic mineralogy, grain-size, alteration, structural and textural relationships, permeability, and porosity

distribution. Twenty-five representative samples from New Mexico and 12 samples from the Michigan core were selected for thin section analyses. The samples encompassed a wide range of weathering, alteration, and deformation features that were observed in the field. Thin sections billets were prepared at USU and sent to Wagner Petrographics for thin section preparation. Poorly indurated and fractured samples were impregnated with epoxy.

Full thin section scans in plane polarized light (PPL) and crossed polarized light (XPL) were generated using a Canon 9000f Mark II scanner utilizing Canon's My Image Garden software. Scan methods, adapted from Mazdab (2017), were taken in the advanced mode using the 35 mm color positive film input. A 3300 x 2100 pixels tiff file was generated with a resolution of 2400 dpi (1 Pixel ≈ 10.5833 μm). A strip of 2.4 x 15.25 cm was cut out at a distance of 2.2 cm from the short edge, and 7.3 cm from and parallel to the long edge of an 8.5 x 11-inch piece of photo paper. A width of 2.4 cm was chosen to mimic the height of 35 mm film and was a good representation of the sample height in the thin sections. The strip was lined with two 6 inch Westcott protractor rulers with approximately 1 mm of overlap. The rulers provided scale and elevated the thin sections above the flatbed, which produced clearer images. The paper was loaded ruler side up into the flatbed of the scanner and taped in place with the long edge directly adjacent to the long edge of the flatbed and the short edge parallel to the Ltr marking. To produce PPL a linear polarization sheet was placed atop and parallel to the ruler's edge. The thin section was placed sample side down straddling the rulers on the polarized light sheet, and the PPL scan was captured. Then another linear polarization sheet was placed on the backside of the thin section perpendicular to the original linear polarization sheet,

to obtain the XPL scan.

Image acquisition with 5x, 10x, 20x, and 63x objectives of key structural and mineralogical features was acquired using an Apple iPhone 6 with a cellphone telescope adapter mount that attaches to the ocular piece of the DM2700 microscope. The iPhone 6's automatic focus allowed for optimum clarity and sharpness. Clarity on the screen with the 20x and 63x objectives was typically superior to that as viewed through the oculars and allowed for further characterization of fine-grained mineralogy and microstructures. The Canon 9000f Mark II scanner can scan thin sections at a maximum resolution of 4,800 x 4,800 dpi, and image sizes can be adjusted based on individual needs.

X-ray Diffraction and X-ray Fluorescence Spectrometry

X-ray diffraction and X-ray fluorescence analyses were performed at Utah State University's X-ray Analysis Laboratory. XRD analyses were executed using a Panalytical X'Pert Pro X-ray Diffraction Spectrometer (40 mA and 45 kV) with monochromatic CuKα radiation utilizing X'Pert Highscore software (see Degen et al., 2014) for phase analysis. XRF analyses were performed using a portable Bruker Energy Dispersive X-ray Fluorescence Spectrometer utilizing S1PXRF, Microsoft Excel, and ARTAX software packages for elemental analysis. XRD samples were powdered using a Rocklabs Standard Ring Mill in a Zirconia 40 mill head. Powdered samples were loaded into aluminum XRD sample stages using glass slides to pack the powdered sample and produce a flat upper surface of powder.

The randomly oriented powder sample mounts were analyzed by counting for 1 s at steps of 0.0200°2θ from 2.0100 to 74.9900°2θ. Phase identification in X'Pert

HighScore was made using the 2016 PDF4 minerals database. Data noise reduction was performed, and peaks and background model were identified using the Search Peaks function using the minimum 2nd derivative method with a minimum significance of 0.5 to 2.0, 0.01 minimum tip width, 1 maximum tip width, and 2 peak base width. Phase analysis was performed using the Search & Match function to identify pattern matches from the PDF4 minerals database. The XRF elemental data, when available and/or needed, was used as an elemental restriction. Customized PDF4 mineral subsets including clays, Fe oxides/hydroxides, micas, hematite, feldspars, and carbonates were created and used in the restrictions dialogue window to help reduce the number of patterns retrieved. Mineral phases were picked from the candidate list, and PDF cards with Star (S,+) and Indexed (I) quality marks were given preference over Blank (B) and Low Precision (O,?) quality cards. Minerals present in thin section 5% or higher were given preference. X'Pert Highscore and Microsoft Excel was used to compare multiple sample datasets from the same transect, locality, or drillcore. Adobe Illustrator and Microsoft Excel were used to create figures. A customized HTML report for each sample was created to include dataset name, phase analysis, pattern list and table, raw data graphic, phase analysis and peak result graphic, mineral phases pattern graphic, anchor scan parameters, peak list, anchor scan data, and document history. XRD was completed for every hand sample with a corresponding thin section, and other alteration and deformation features.

XRF spectra were taken at 40 kV and 30 uA with a count time of 30 seconds to give a general overview of the elemental composition of samples from the Michigan drillcores. Spectra and peak matches were determined using the Bayesian deconvolution

method utilizing the ARTAX software package. A general Bayesian deconvolution was used on all samples from each locality and then separate Bayesian deconvolutions were done from sample subsets of samples with suspected of high concentrations of graphite, quartz, calcite, clays, or Fe oxides. Elemental peaks for samples were chosen for best match on the Bayesian model. This iterative process was repeated until the Bayesian model best fit the sample spectra. XRF spectra were taken at 45 kV and 25 uA with a count time of 60 seconds using the green filter (Al-Ti-Cu) to analyze the high energy elemental spectra of 5 New Mexico samples. These spectra were used to rule out odd mineralogical matches determined from XRD, including Mo and U bearing minerals.

Structural and Permeability Analyses

The FracPaQ toolbox (Healy et al., 2017) written in MATLAB code, was used to determine fracture length, geometry, and connectivity and estimate fracture intensity, density, and permeability. Photographs were opened with Adobe Illustrator and fracture traces mapped manually using the Pen Tool. The fracture traces were then saved as a .svg file. Every fracture trace is comprised of multiple fracture nodes and segments. FracPaQ2D was run in MATLAB. The .svg file was opened in FracPaQ2D using the Node File input file type. FracPaQ2D was run to generate color-coded fracture trace and segment maps and statistics and estimate permeability, connectivity, fracture intensity, and fracture density. The number of scan circles used for estimating and generating fracture intensity and density maps was changed iteratively until the scan circle radius was closest to 10 cm for consistency and to allow for outcrop comparisons.

We then used our data and observations to subdivide the interface into discrete mechanical and stratigraphic units based on hydrologic and geomechanical properties and developed conceptual geological and permeability models. Understanding the heterogeneities of the interface and collection of data are imperative to providing constraints and inputs for hydro-geomechanical and numerical flow models, which have a multitude of important applications. Our geologic data and conceptual models were integrated into hydromechanical models to help better understand pressure migration proximal to basal nonconformities and possible mechanisms of induced seismicity.

NEW MEXICO AND COLORADO RESULTS

Geologic Background of the Rocky Mountain and Four Corner Region

The geologic history of the southern Rocky Mountain region, including northern New Mexico and southern Colorado, extends to nearly 2 Ga with the crystalline rocks of the Yavapai province and the overlying Proterozoic Uncompahgre Formation and Uinta Mountain Group. During early and middle Paleozoic time, Cambrian to Mississippian, the majority of what is now New Mexico, Colorado, Utah, and Arizona was part of a broad positive area inundated by the ocean (Sloss, 1963; Armstrong et al., 1992; Baltz & Myers, 1999). A primarily transgressive sequence of limestone and sandstone units were deposited in primarily shallow marine environments, including the Ignacio Formation, Elbert Formation, Ouray Limestone, Leadville Limestone, and Tererro and Espiritu Santo Formations (Baltz & Myers, 1999; Gonzales et al., 2003).

During Late Mississippian to early Permian time, Laurentia and Gondwana collided and far-field stresses uplifted the Ancestral Rocky Mountains, which included the Uncompahgre uplift and Front Range uplift (Eardley, 1951; Baars, 1966; Graham et al., 1976; Kluth & Coney, 1981; Baars & Ellingson, 1984; Kluth, 1986; Eaton, 1987; McBride & Nelson, 1999; Dickinson & Lawton, 2003; Chapin et al., 2014). Sea level dropped, and sediments eroded from the Ancestral Rockies were deposited into adjacent synorogenic basins and passive margins.

During the Triassic, Pangea began rifting apart (Dickinson, 1978). The last of the Ancestral Rocky Mountains were eroded by Jurassic time, a period of dry and arid climate when several large eolian dune formations were deposited including the Navajo

and Entrada Formations (Kocurek & Dott, 1983). During the Cretaceous, the subduction of the Farallon Plate beneath North America resulted in the subsidence of the Cretaceous Western Interior Basin, which hosted the Western Interior Seaway (Pang & Nummedal, 1995; Liu et al., 2014), where marine carbonate, shale, and sandstone units were deposited. Uplift and deformation occurred during the Laramide Orogeny, during Late Cretaceous to middle Tertiary, which developed from the shallow subduction of the Farallon plate beneath the North America plate (Dickinson & Snyder, 1978; Liu & Gurnis, 2010). The rocks were overprinted by Eocene to Oligocene volcanic rocks, including the San Juan volcanics, during the Mid-Tertiary Ignimbrite Flare-up (Coney & Reynolds, 1977; Davis & Coney, 1979). The current landscape of the Rocky Mountains is a result of Neogene uplift and subsequent erosion by glaciers, rivers, and streams (Eaton, 2008; Cather et al., 2012).

Gallinas Canyon, New Mexico

The Sangre de Cristo Mountains are a north-trending structural block bounded by northeast-trending thrust faults that were uplifted in the Laramide Orogeny (Lessard & Bejnar, 1976; Baltz & O'Neil, 1986; Baltz & Myers, 1999; Lindline et al., 2015). During the Mississippian, this area was likely a shallow-marine shelf, where a series of sandstone and carbonate units were deposited (Baltz & Myers, 1999). Compression during the Laramide Orogeny resulted in the uplift of a north-trending structural block and the concurrent formation of the Raton Basin (Lessard & Bejnar, 1976; Baltz & Myers 1999).

The nonconformity in the Gallinas Canyon consists of Proterozoic metamorphic and igneous rocks overlain with sedimentary rocks of the Pennsylvanian Sandia

Formation, and the Mississippian Espiritu Santo Formation and Tererro Formation of the Arroyo Penasco Group (Fig. 1) (Baltz, 1972; Baltz & O'Neil, 1986; Baltz & Myers 1999; Lindline et al., 2015). The Arroyo Penasco Group underwent dolomitization, dedolomitization, silicification, calcitization of evaporites, and brecciation prior to deposition of the Sandia Formation (Ulmer & Laury, 1984). The crystalline basement consists of highly deformed compositionally layered quartzofeldspathic gneiss, amphibolitic gneiss, felsite, biotite schist, and granitic pegmatite (Baltz & O'Neil, 1986; Baltz & Myers, 1999; Lemen et al., 2015; Lindline et al., 2015). The Espiritu Santo Formation consists of primarily limestone and dolomitic limestone, with a basal conglomeratic sandstone known as the Del Padre Member (Baltz, 1972; Baltz & Myers, 1999). Previous detailed work in the Gallinas Canyon has primarily focused on the sedimentary units (Baltz & Myers, 1999), while few published works exist on the underlying crystalline basement. The Precambrian crystalline rocks are cut by large thrust faults and smaller scale normal faults (Baltz, 1972; Lessard & Bejnar, 1976; Baltz & Myers, 1999) with some juxtaposing sedimentary and crystalline rock.

In the Gallinas Canyon, the crystalline rock is overlain by the 0.5 to 1.5 m thick marine Del Padre Sandstone, silica and calcite-cemented, grayish-olive and tan, jointed, fine to very coarse-grained sandstone (Baltz & Myers, 1999). The Del Padre Member, in New Mexico, can be up 15 m thick and fills depressions in underlying crystalline rock (Armstrong & Mamet, 1974). In some areas, the Del Padre Sandstone member rests atop deeply weathered regolith (Baltz & Myers, 1999). In the Pecos River valley, the weathered horizon or regolith is over 10 m thick and contains large boulders and corestones (Baltz & Read, 1960). The Del Padre Sandstone is overlain by 3.5 to 4.0 m of

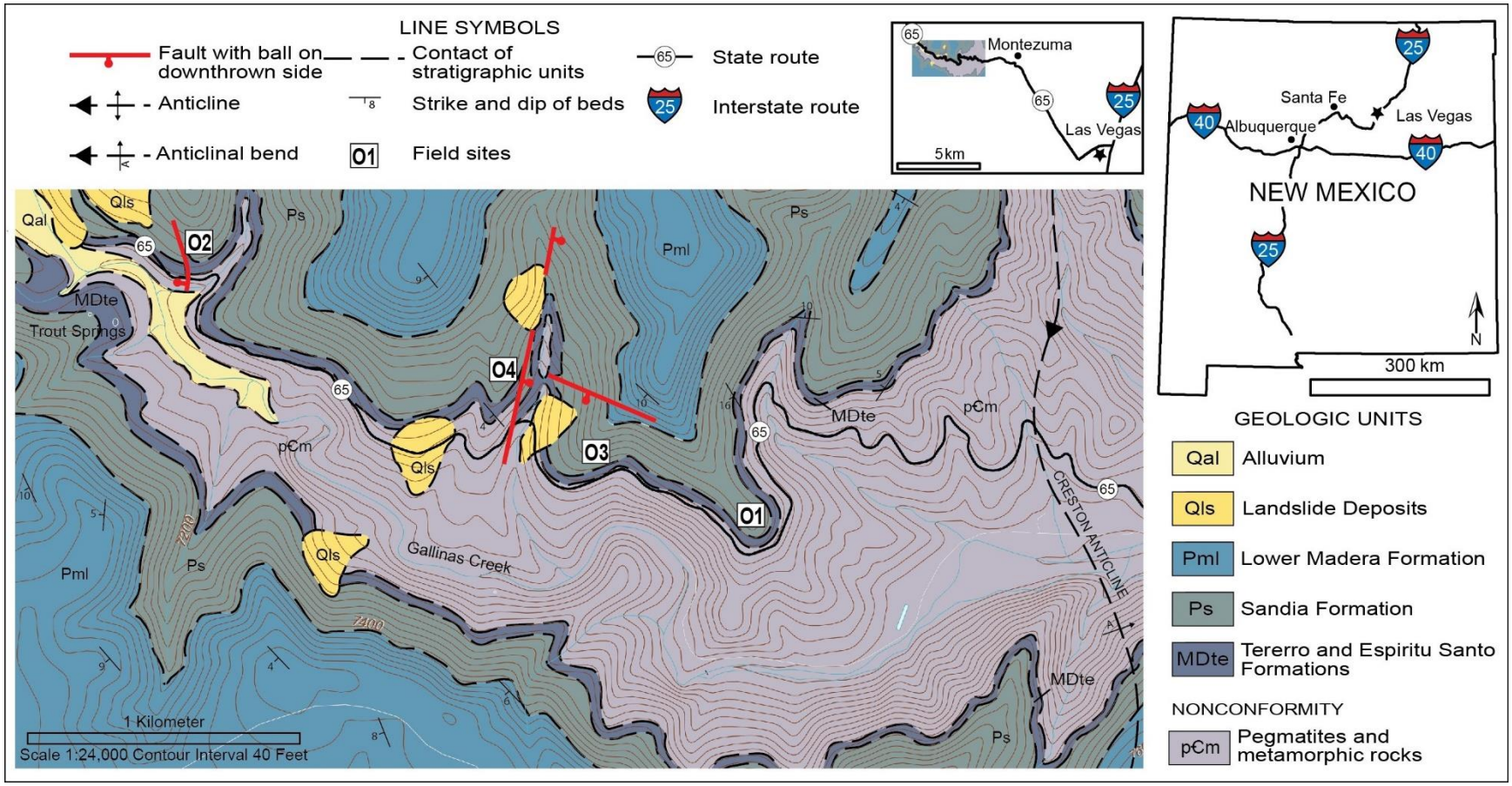

Figure 1. Geologic map of New Mexico field sites. Field sites O1, O2, O3, and O4 are located along NM State Route 65. Note the nonconformity is relatively planar, and generally parallels contour lines. The nonconformity is offset by several map-scale normal faults. The geologic map was digitized from (Baltz, 1972) onto a USGS topo map (U.S. Geological Survey, 2010).

carbonate rocks of the Espiritu Santo Formation (Baltz & Myers, 1999; Kerner, 2015). The exposures in Gallinas Canyon are analogous to the rocks in the adjacent Las Vegas Basin, a sub-basin of the Raton Basin, which is east of our field site. The nonconformity represents a period of non-deposition and erosion and a time gap of over 1 billion years.

Baker's Bridge, Colorado

The Baker's Bridge field site was chosen because of the relatively unweathered and undeformed contact. The Baker's Bridge field site is located approximately 15 miles north of Durango, off of Highway 550, on County Road 250 on the curve west of the historical landmark Baker's Bridge. The 1.7 Ga Precambrian Baker's Bridge Granite (Gonzales, 1997) is overlain by 23 m of the Late Devonian Tamarron Member of the Ignacio Formation and 4 m of the McCracken Member of the Elbert Formation (McBride, 2016). The Baker's Bridge granite is described as relatively homogenous, coarse-grained biotite-magnetite-hornblende granite primarily composed of microcline, perthite, quartz, plagioclase, and hornblende with accessory zircon, apatite, magnetite, calcite, and epidote (Gonzales et al., 2003). Feldspars and mafic minerals are commonly altered to clays, sericite, and iron oxide (Gonzales et al., 2003).

The Precambrian basement surface has 65 m of relief (McBride, 2016), and locally Precambrian conglomerates, up to 43 m thick, rest unconformably on top (Baars, 1965; McBride, 2016). The Tamarron Member at Baker's Bridge is brown, purple, red, and white sandstone with quartz cement, planar laminations, and cross-beds, with thin interbeds of shale, and the McCracken Member is sandy dolomite (McBride, 2016). Bleached zones and beds, locally 20 to 80%, occur in coarse layers (McBride, 2016).

New Mexico Field Sites

I examined four sites along the nonconformity at the New Mexico site. Outcrop sites O1, O2, O3, and O4 (Fig. 1) consist of variably weathered igneous and metamorphic crystalline basement rocks overlain by the Espiritu Santo Formation (Table 2). A weathered zone with variable thickness, 0 to >5 m, lies atop the crystalline basement rock and is truncated by the Del Padre Sandstone. Locally the basal sandstone is laterally discontinuous and pinches and swells, and in areas carbonate units of the Espiritu Santo Formation lie directly atop the crystalline basement.

Locally, the mineralogy of the Del Padre Sandstone is dominated by quartz with lesser feldspar and lithic fragments and in sections overprinted by deep red hematite mineralization and/or cement (Table 2). The sandstone appears less jointed than the crystalline basement and locally forms overhanging ledges, primarily where it rests atop highly weathered crystalline basement. Locally a diffuse contact exists between the basal sandstone and an unconsolidated 'wash' that is situated atop the weathered crystalline rocks. At the map-scale, the nonconformity is relatively planar with little to no undulation (Fig. 1). At the outcrop scale, the contact is slightly wavy and undulatory. Map-scale faults with vertical offset up to 36.5 m (Fig. 1) and small-scale shear fractures with offsets of less than 1 cm cut the nonconformity.

Site O1

The crystalline basement at site O1 consists of deformed granitic gneiss interlayered with amphibolite gneiss, pegmatite, and miscellaneous metaigneous and metasedimentary units (Fig. 2-5). The crystalline basement is moderately to highly

Table 2 Weathering and rock strength classification of New Mexico samples, and summary of mineralogical analyses. Bei: beidellite; Bt: biotite; Cal: calcite; Chl: chlorite; Fe: iron; Ill: illite; Jrs: jarosite; Kfs: K-feldspar; Ms: muscovite; Pg: palygorskite; Phl: phlogopite; Pl: plagioclase; Qtz: quartz; Rt: rutile; S: Sulphur.

Sample	Weathering Classification	Rock Strength	Mineralogy XRD	Description	Grain Size / Textures	Figures
O3P1#7	I	R5-R6	Pl, Qtz, Kfs, Bt, ± Gr	fresh gneiss 25 m E of Fig. 20a	gneissic, anhedral grains, inequigranular, granoblastic interlobate	Fig. 11 - (A)-(H)
O3P1#1	II	R5	Qtz, Pl, Kfs, Bt, ± Gr, Chl, Ill	gneiss core stone (See Fig. 20a)	gneissic, anhedral grains, inequigranular, interlobate	Fig. 12 - (A)-(C)
O3P1#2	II-III	R4	Qtz, Kfs, Pl	gneiss weathering rind (See Fig. 20a)	gneissic, exfoliation, anhedral grains, inequigranular, interlobate	Fig. 12 - (D)-(H)
O3P1#3	III	R3	Qtz, Pl, Kfs, Bt, ± Gr, Ill, Chl	gneiss clay infilled fracture (See Fig. 20a)	gneissic, anhedral grains, inequigranular	Fig. 13 - (A)-(F)
O3P1#4	III-IV	R3-R2	Qtz, Kfs, ± Ill	gneiss directly below interface (See Fig. 20a)	gneissic, anhedral grains, inequigranular	Fig. 13 - (G), (H)
O3P1#5A	IV	R2	Qtz, Kfs, Fe, ± Ms, Ill	weathered and slickenslided 6 m W of Fig. 20a	gneissic?, coarse, disturbed, inequigranular	
O3P1#5b	IV	R2	Qtz, Cal, Kfs, Fe, ± Ms, Ill	weathered and slickenslided 6 m W of Fig. 20a	gneissic?, coarse, disturbed, inequigranular	Fig. 14 - (A), (B)
O3P1#6	V	R1	Qtz, Kfs, Fe, ± Bt, Ill	directly below interface 6 m W of Fig. 20a	coarse, disturbed, inequigranular	Fig. 14 - (C)-(F)
O1P11	III	R3-R4	Qtz, Pl, Kfs, Ill	gneiss pink layer (Fig. 19a)	gneissic, anhedral grains, inequigranular	
O1P12	III-IV	R3	Qtz, Bt, Ms, Kfs, ± Chl	gneiss black to gray layer (Fig. 19b)	gneissic,	
O241 A, B	IV	R1-R2	Qtz, Cal, Kfs, ± Pg	wall rock of white feature 1 m from fault (Fig. 6a-c)		Fig. 9 - (C)-(H)
O241 A, B	-		Cal, Fe, Qtz, Kfs ± Gr, Pg, Ill	infill of white structural feature 1 m from fault (Fig. 6a-c)		
O242			Qtz, Cal, Kfs, ± Gr, Ill			
O243 A, B	IV	R1-R2	Qtz, Cal, Kfs, ± Pg			Fig. 9 -(A), (B)
O246	III-IV	R1	Qtz, Kfs, ± Ms, Ill	fault gouge, below dolomite block (Fig. 20a,d)	foliated cataclasite	Fig. 8 (A), (B), (C), (D)
O247	IV	R1	Qtz, Kfs, Ms, ± Cal, Pg	fault gouge above dolomite block (Fig. 20a)	cataclasite	
O1P71	III	R3-R4	Qtz, Kfs, Pl, Bei	pegmatite (Fig. 20b)	Very coarse, subhedral grains perthitic,	Fig. 5 - (H), (I)
O1P72	IV-V	R2	-	pegmatite wash 12 in below interface (Fig.20c)	Coarse grains, sub-angular, clay matrix	Fig. 5 - (F), (G)
O1P73	III	R3-R4	Kfs, Pl, ± Phl, Bei	pegmatite (Fig. 20b)	Very coarse, subhedral grains, perthitic,	Fig. 5 - (J), (K)
O1P74	V	R1	-	pegmatite wash 6 in below interface (Fig. 20c)	Coarse grains, sub-angular, clay matrix	Fig. 5 - (E), (D)
O1P51	III-IV	R3	-	serpentinite?		
O1P33B	III-IV	R3	Qtz, KFs, Fe, ± Ill, Cal, Ms, Chl	amphibolite gniess		
O1P42A	VI-V	R1-R2	Qtz, Fe, ± Jrs, Ill	metabasite / amphibolite 1 ft below interface		
O1P42B	VI-V	R1-R2	Qtz, Jrs, S	metabasite / amphibolite 1 ft below interface (See Fig. 2a,b)		Fig. 14 - (G), (H)
BS2	-	R3-R4	Qtz, Fe, Kfs	basal sandstone brown	medium to coarse, sub-angular, moderately-sorted	Fig. 15 - (C), (D)
BS3	-	R3-R4	Qtz, Fe, Kfs	basal sandstone green	medium to coarse, sub-angular, moderately-sorted	Fig. 15 - (A), (B), (E), (F)
BS6	-	R2-R3	Qtz, Fe, Rt, ± Ill, FeMg Oxide, Ms	rust to red altered basal sandstone	medium to coarse, sub-angular, moderately-sorted	

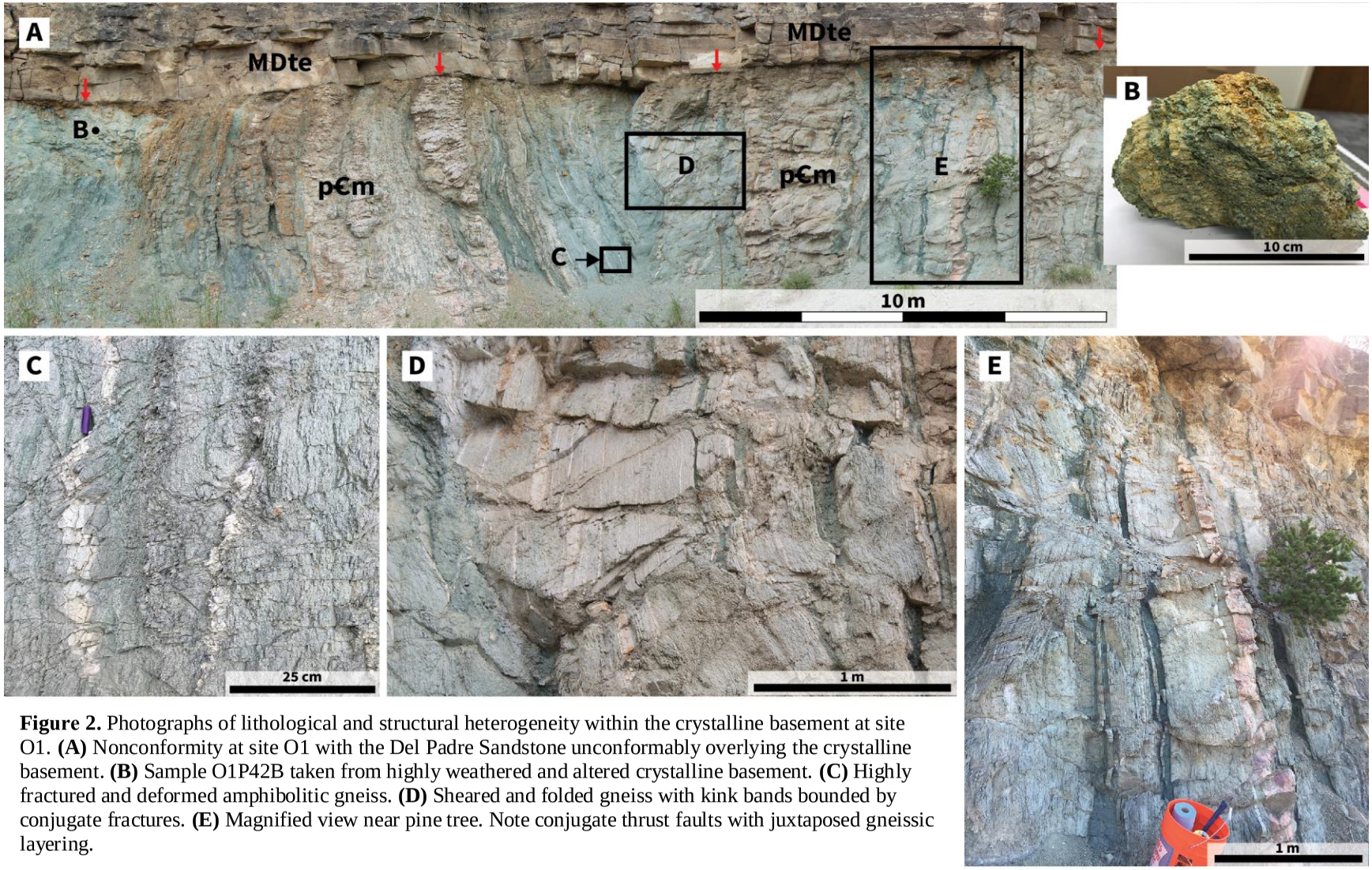

Figure 2. Photographs of lithological and structural heterogeneity within the crystalline basement at site O1. **(A)** Nonconformity at site O1 with the Del Padre Sandstone unconformably overlying the crystalline basement. **(B)** Sample O1P42B taken from highly weathered and altered crystalline basement. **(C)** Highly fractured and deformed amphibolitic gneiss. **(D)** Sheared and folded gneiss with kink bands bounded by conjugate fractures. **(E)** Magnified view near pine tree. Note conjugate thrust faults with juxtaposed gneissic layering.

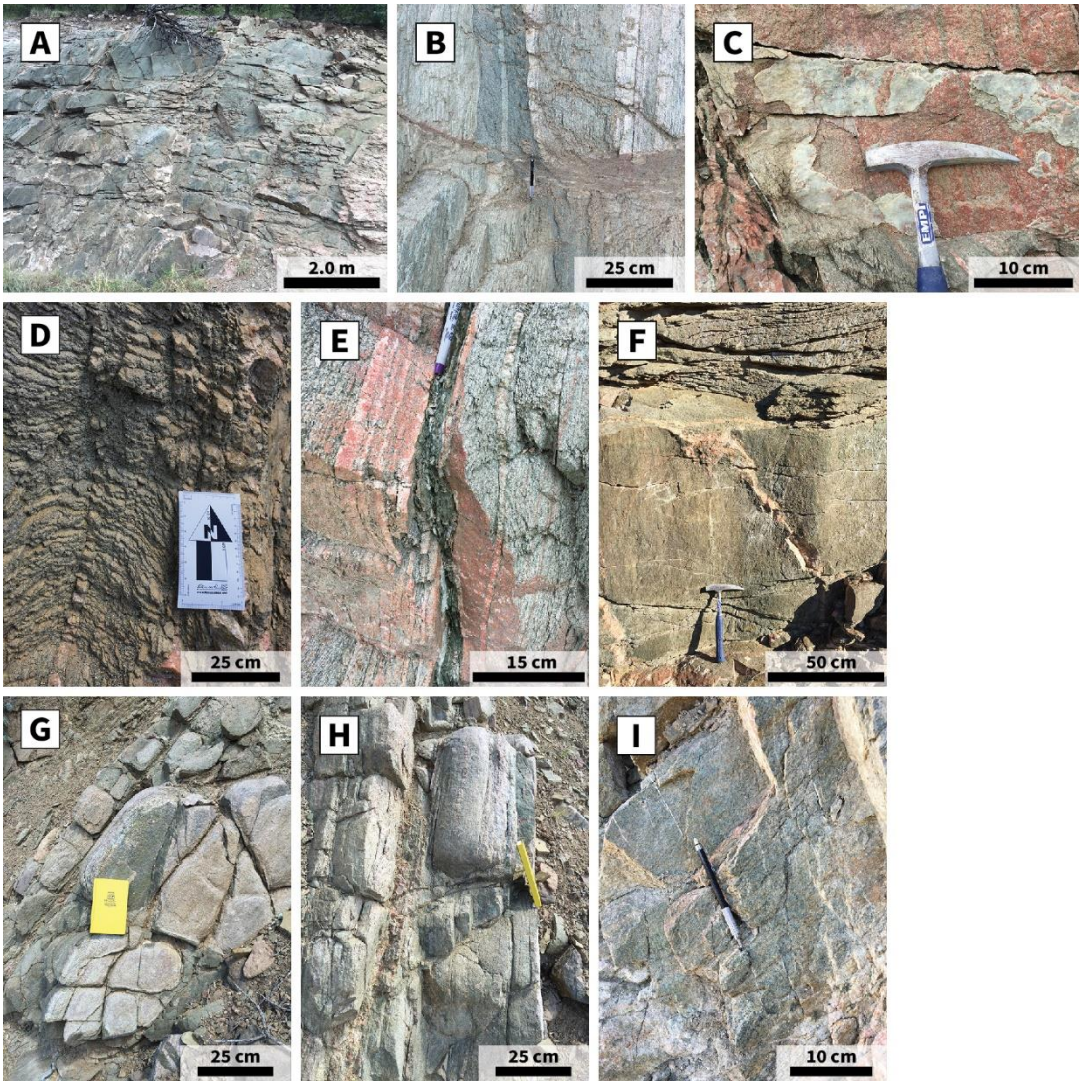

Figure 3. Photographs of structural and lithological features at site O1. **(A)** Gneiss with conjugate joints. **(B)** Small-scale fault offsetting compositional layering. **(C)** Intersecting joint and foliation parallel fractures (left) with white calcite infill. **(D)** Exfoliation weathering pattern in gneiss. **(E)** Layer and foliation parallel calcite vein in phyllosilicate-rich compositional layer. **(F)** Fractures in gneiss along foliation surface. **(G)** Perpendicular to gneissic foliation view of spheroidal weathering, corestones, and joint/fracture patterns within the crystalline basement. Note white calcium carbonate coating and alteration along foliation plane. **(H)** Parallel to gneissic foliation of (G). The field notebook remains stationary. **(I)** Fracture splays within the crystalline basement infilled with calcium carbonate.

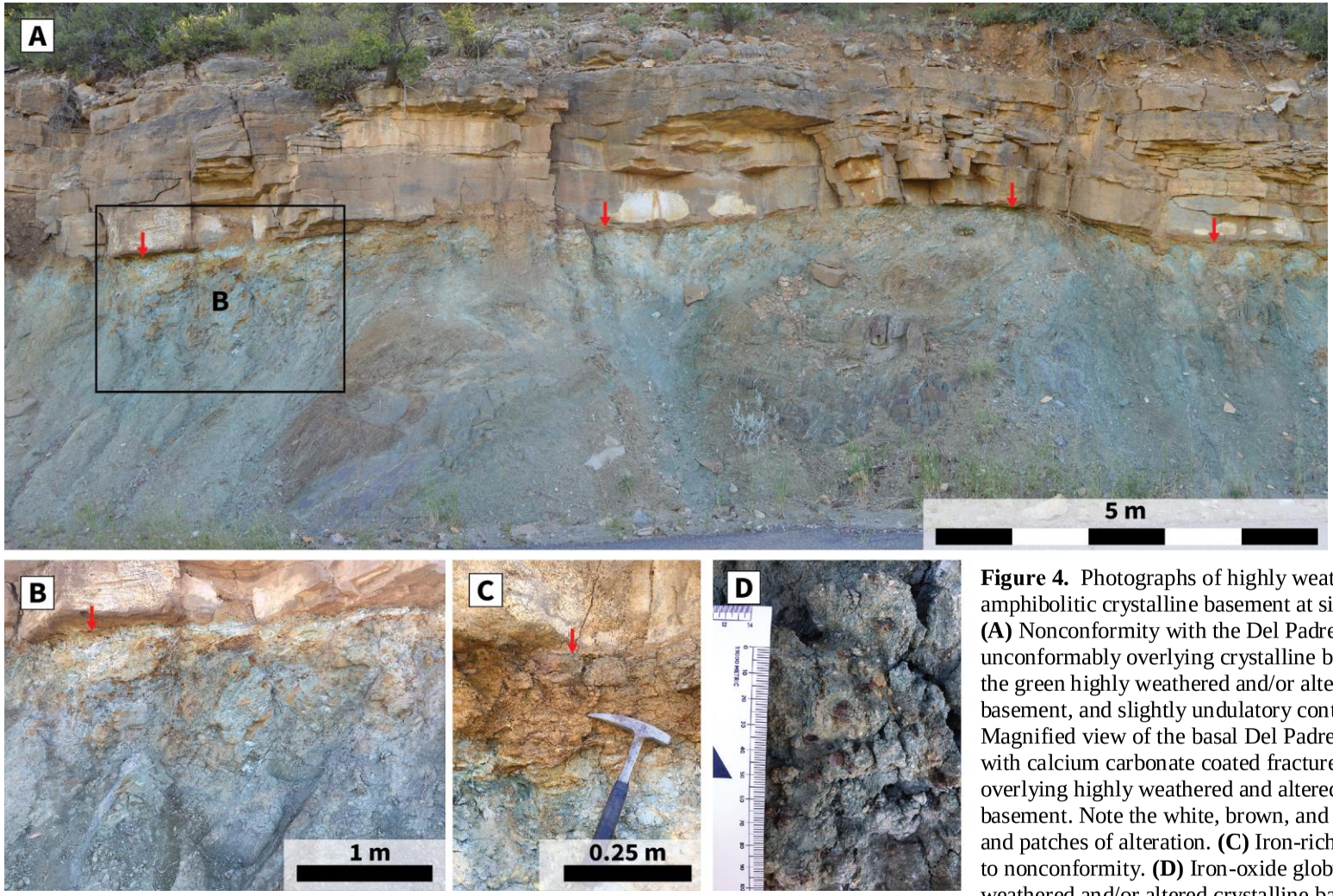

Figure 4. Photographs of highly weathered amphibolitic crystalline basement at site O1. **(A)** Nonconformity with the Del Padre Sandstone unconformably overlying crystalline basement. Note the green highly weathered and/or altered crystalline basement, and slightly undulatory contact. **(B)** Magnified view of the basal Del Padre Sandstone, with calcium carbonate coated fracture surfaces, overlying highly weathered and altered crystalline basement. Note the white, brown, and green colors and patches of alteration. **(C)** Iron-rich crust adjacent to nonconformity. **(D)** Iron-oxide globules within weathered and/or altered crystalline basement.

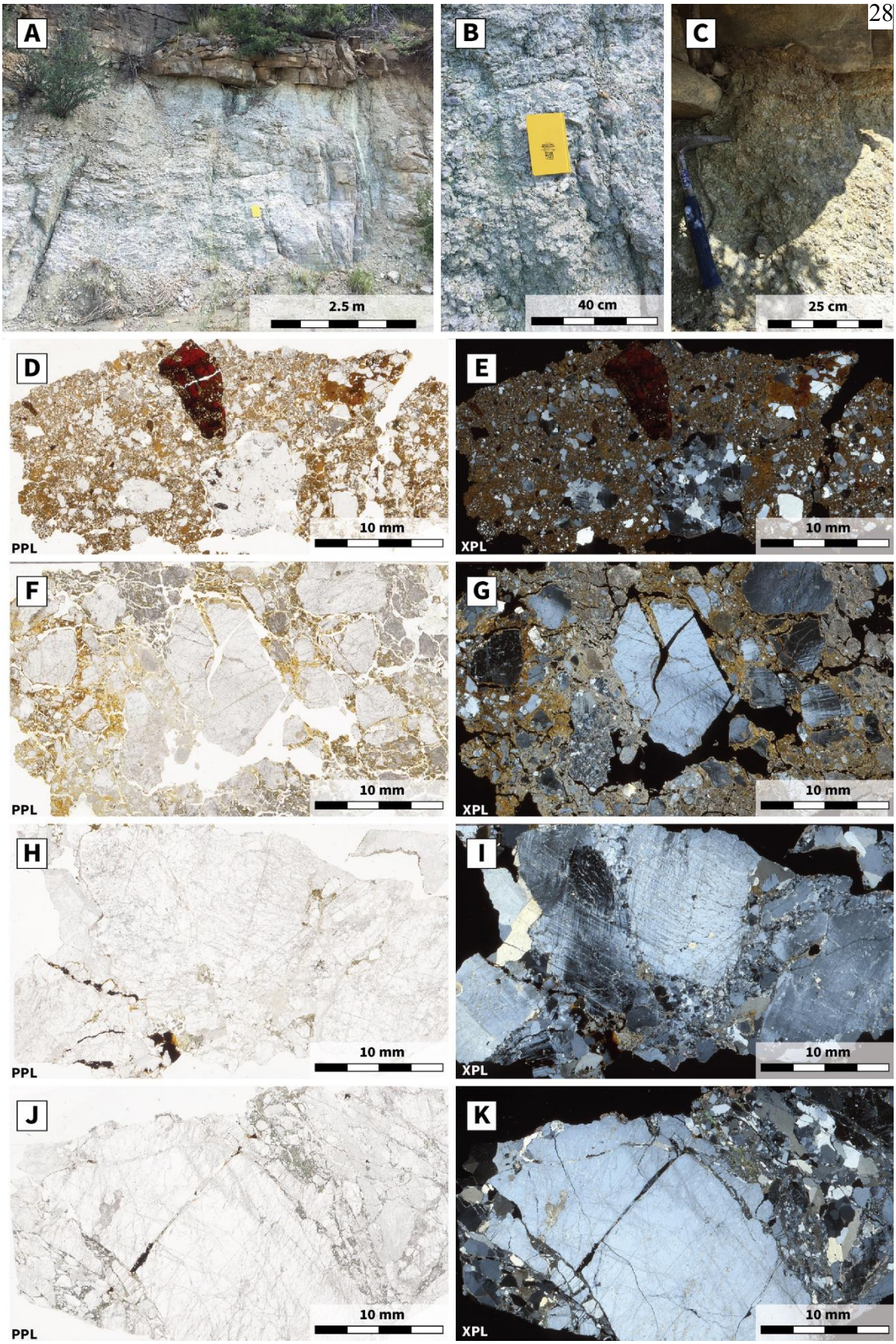
A
2.5 m
B
40 cm
C
25 cm
D
10 mm
PPL
E
10 mm
XPL
F
10 mm
PPL
G
10 mm
XPL
H
10 mm
PPL
I
10 mm
XPL
J
10 mm
PPL
K
10 mm
XPL

Figure 5. Photographs and thin section scans of alkali granitic pegmatite, and associated microstructures. Samples are progressively more weathered from bottom to top. **(A)** Outcrop view of the pegmatite. Degree of weathering increases towards the nonconformity. **(B)** Magnified view of the highly fractured pegmatite. Notebook for scale. **(C)** Pegmatite wash adjacent to the nonconformity. **(D)** Coarse-grained regolith and/or 'wash'. Mineral clasts include quartz, feldspar, and lithic fragments. Large alterorelic completely replaced by bright red to orange iddingsite and iron oxides. (PPL). **(E)** Same area as (D). Granitic lithorelic (center bottom) and abundant detrital quartz in an iron rich clayey soil material. (XPL). **(F)** Aggregates of quartz and lithic fragments in a clayey matrix. Highly disturbed pegmatite. (PPL). **(G)** Same area as (F). (XPL). **(H)** Large highly fractured perthitic feldspar grains. Fractures infilled with phyllosilicates, iron oxides, and quartz. Towards the upper left, plagioclase grains display remnant oscillatory zoning. (PPL). **(I)** Same area as (H). Feldspar grains display uneven extinction and deformation twining. Reduction of grain size and brecciation along fracture planes. Evidence of grain rotation, and recrystallization. (XPL). **(J)** Large highly fractured perthitic feldspar grain (center). Grain is broken up into smaller fragments along its margins, evidence of shearing and/or grain sliding. Fractures are infilled with fine-grained phyllosilicates, quartz, and iron oxides. Patchy alteration to sericite, specifically along fracture traces, gives the feldspars a dusty appearance. (PPL). **(K)** Same view as (J). (XPL).

weathered (Table 2), and contains abundant structural and physical weathering features (Fig. 3a-i). Gneissic foliation is nearly vertical (Lindline et al., 2015) or dips steeply to the southeast, and cm- to m-scale parasitic gneissic folds are common. The crystalline basement is cut by joints, conjugate shear fractures, and small-scale faults that offset compositional layering and foliation (Fig. 2c-e, 3b-i). The small-scale faults and shear fractures are infilled with fine-grained phyllosilicates, debris, and/or calcium carbonate and typically display slickensided surfaces. Intersecting fractures, joints, and foliation planes are locally infilled with calcite and/or weathered clayey material, and discolored and altered along their margins (Fig. 3b-i). The gneissic layers and joint have undergone weathering, chloritization, epidotization, and sericitization (Fig. 2a-b, 3a-d) (Lindline et al., 2015). Joints appeared progressively less altered with increasing depth below the nonconformity. Anastomosing calcite veins 0.3 to 3.0 cm thick are intermittently distributed in the gray to green to black phyllosilicate-rich compositional layers (Fig. 3e). Small-scale conjugate thrust faults and fractures are abundant (Fig. 2c-e). Locally, conjugate thrust faults intersect at approximately 60° forming triangular shaped wedges with juxtaposed gneissic layering on either side (Fig. 2e). Fracture planes are infilled with calcite, clayey material, and/or iron oxides. The thrust faults dominantly truncate at the nonconformity. Locally, shear fractures, joints, and exfoliation fractures are infilled with a white clayey material forming root-shape structures emanating from the nonconformity and extending and tapering into the crystalline basement. Locally, these white structures occur in highly chaotic and branching vein networks.

The crystalline basement beneath the nonconformity is dominated by moderately to highly weathered gneiss (Fig. 2a). The thickness of the weathered horizon is variable.

In areas fresh to slightly weathered granitic gneiss lies directly beneath the nonconformity (Fig. 3a). In contrast, a weathered horizon of amphibolite, up to 5 m thick, also lies directly beneath the interface (Fig. 4a). Locally the sandstone forms ledges that overhang the crystalline basement. The metamorphic rocks and layers have receded to different extents beneath the basal sandstone member making the outcrop face irregular and uneven. The phyllosilicate content gradually decreases with depth as the rock grades to fresh crystalline basement. Alluvium truncates the crystalline basement and/or sedimentary rocks.

The gneiss is cut by abundant cm- to m-thick granitic pegmatite sills that intruded parallel to subparallel to foliation and compositional layering. Near the western portion of site O1, a 4.5 m to 5 m thick alkali granitic pegmatite (Fig. 5a-k) is white to pale pink-purple-green and highly fractured at the micro- to outcrop scales (Fig. 5b). In thin section, large euhedral perthitic feldspar grains, with widespread dusty gray alteration to fine-grained clays and relict igneous textures (Fig. 5h-k), characterize the pegmatite. Alteration is concentrated and/or localized to fracture and cleavage planes and grain-to-grain contacts. The feldspar grains are cut by several small-scale shear fractures infilled and/or bounded by brecciated wall rock material, quartz, iron oxides, and fine-grained phyllosilicates (Fig. 5h, 3j). Quartz and feldspar grains display undulatory extinction and sutured grain boundaries (Fig. 5j, 3k). Towards the interface, the pegmatite is progressively more weathered (Fig. 5d-g). The large feldspar grains become enclosed by a fine-grained phyllosilicate-rich groundmass (Fig. 5d-g). The weathered pegmatite grades into a “granitic wash” made up quartz, feldspar, and lithic clasts in a clayey matrix (Fig. 5d, 3e). The fine-grained phyllosilicate abundance increases from approximately

10-15% in slightly weathered pegmatite to >65% in the granitic wash (Fig. 5d-k).

The mafic rocks, amphibolite gneiss, biotite gneiss, serpentinite, and metabasites are medium to dark gray to green and appear to have a more developed and thicker weathered horizon (Fig. 4a) than the felsic basement. The weathered horizon is iron-rich and typically has yellow to orange to brown coloration (Fig. 4a, 4b), and locally contains sporadic iron oxide alteration patches and/or globules up to 2 cm^2 (Fig. 4c, 4d). Primary pyroxene and amphibole grains are moderately to completely altered to and/or replaced by secondary chlorite, quartz, epidote, jarosite, and iron oxides (Table 2). Locally an indurated iron crust, 0.25 to 1 m thick, makes up the uppermost section of the iron-rich weathered crystalline basement (Fig. 4c). Shear fractures coated with slickensided and/or iridescent iron oxide are present 1 to 2 m below the nonconformity in a 5 m^2 block of a weathered metabasite and/or amphibolite, and in the overlying sandstone and limestone units. The basal sandstone forms sharp and gradational contacts with the weathered horizon. Locally the basal strata of sandstone, adjacent to the nonconformity, is altered and contains abundant iron oxide mineralization and/or iron-rich cement and matrix. The basal sandstone displays a general coarsening downwards, and near the nonconformity tends to be conglomeratic or coarse to very coarse-grained.

Site O2

The nonconformity at site O2, also studied by Kerner (2015), consists of moderately to highly weathered granite and granitic gneiss truncated by the Del Padre Sandstone (Fig. 6a-g, 7). The nonconformity is offset by a west-side down normal dip-slip fault (Lindline et al., 2015; Kerner, 2015), with an apparent offset of approximately

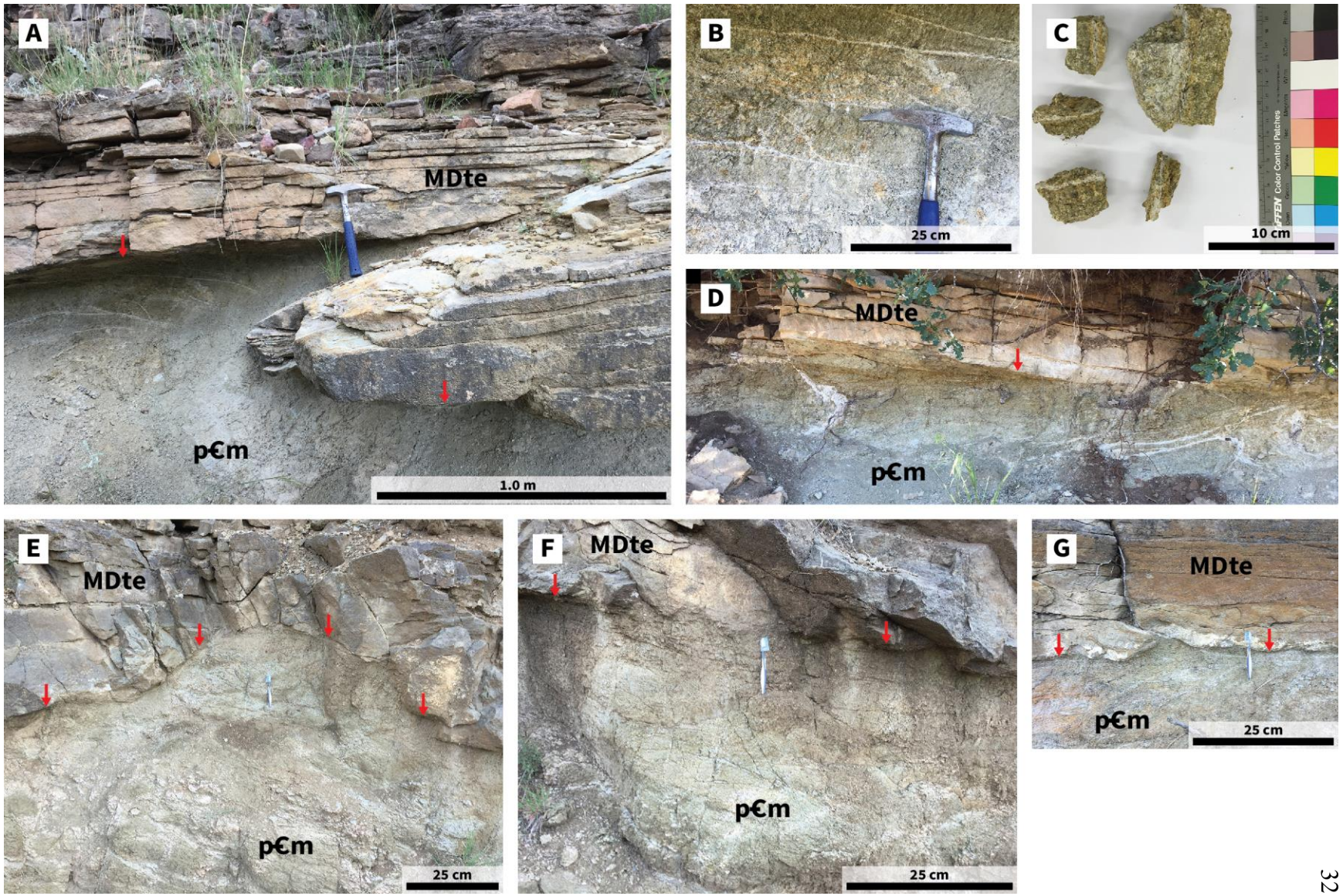
A
MDte
p€m
1.0 m
B
25 cm
C
10 cm
D
MDte
p€m
E
MDte
p€m
25 cm
F
MDte
p€m
25 cm
G
MDte
p€m
25 cm

Figure 6. Photographs of structural features at site O2. (A), (B) Rock hammer for scale = 0.33 m. (E), (F), (G) Toothbrush for scale ≈ 8.5 cm. **(A)** Reverse fault with slickensided fault surfaces with white clayey features emanating from the fault surface into the crystalline basement. **(B)** Magnified view of white features in (A). **(C)** Sample O241 A,B photograph. **(D)** Roots and associated mineralization and alteration. **(E), (F)** Abundant fractures cutting crystalline basement and overlying sedimentary rocks. Note the undulating and steeped nonconformity contact. **(G)** Weathered basement infilled fracture adjacent to nonconformity in the sedimentary units.

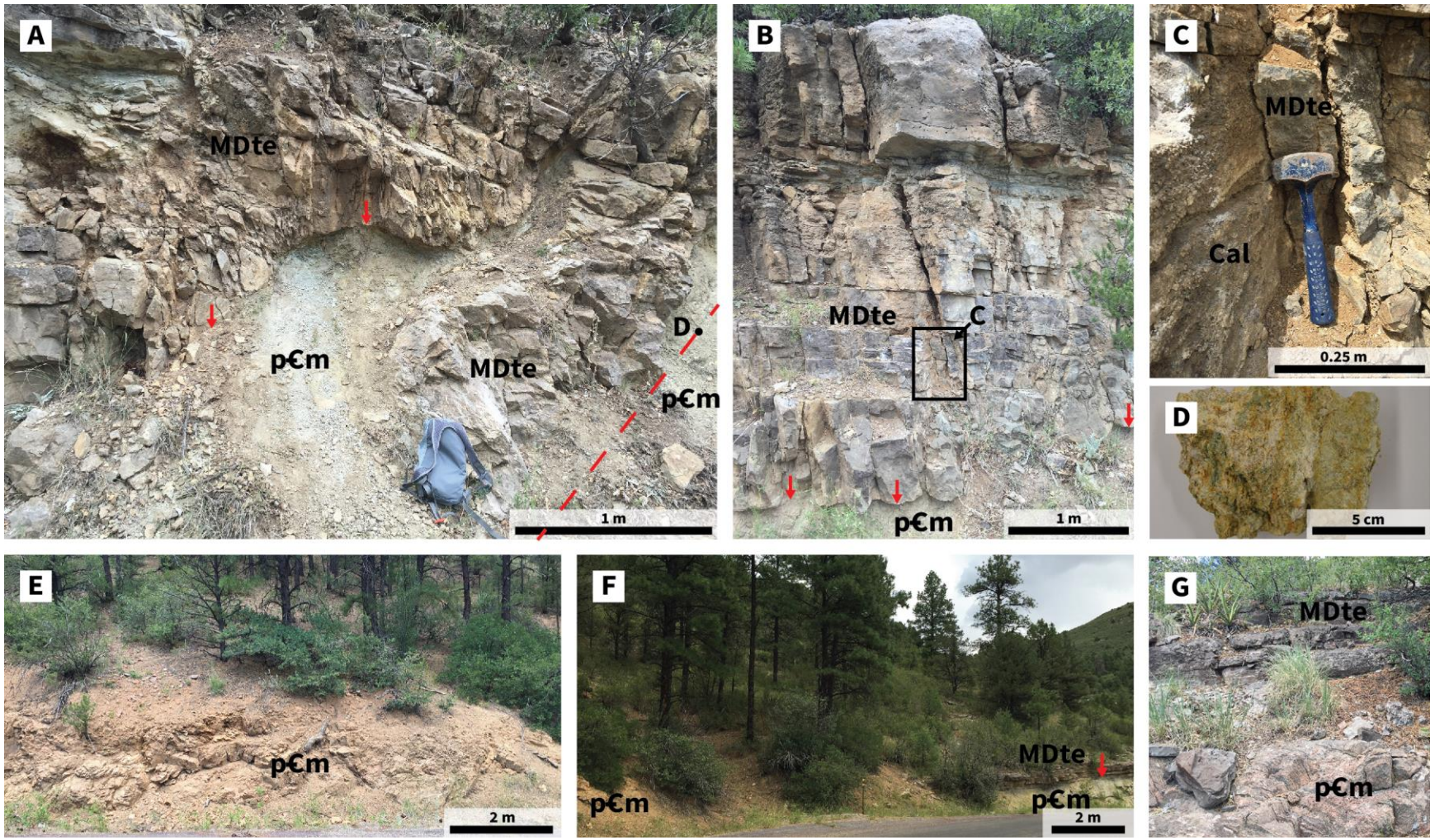
A
MDte
p€m
MDte
D
p€m
1 m
B
MDte
C
p€m
1 m
C
MDte
Cal
0.25 m
D
5 cm
E
p€m
2 m
F
p€m
MDte
p€m
2 m
G
MDte
p€m

Figure 7. Photographs of map-scale normal faults and associated structures at site O2 (A-D), and site O4 (E-G). (See Fig. 1.) (A) Fault with phyllosilicate rich core with interface offset between granitic basement and sedimentary rocks. A large block of dolomite (above backpack) has broken off and been incorporated into fault core. Sample O246 taken below dolomite block within crystalline basement fault core. **(B)** Sedimentary damage zone with large mineralized and unmineralized subvertical fractures. **(C)** Magnified view of subvertical coarse crystalline calcite veins. Veins are on either side of the head of the hammer. **(D)** Sample O246 from crystalline basement fault core. Sample location marked in (A). See (Fig. 8) for thin section photomicrographs. **(E)** Fault damage zone in footwall gneiss of a high angle normal fault (West). Note the crystalline basement is highly fractured. **(F)** Fault core and nonconformity in the hanging wall the high angle normal fault (East). The fault core is largely concealed by alluvium and vegetation. Note the highly weathered crystalline basement and overhanging sandstone ledges (lower right corner). **(G)** Nonconformity in the footwall of the map-scale normal fault, with fresh gneiss at the interface.

4.5 m to 5 m (Fig. 7a). The weathered crystalline basement is offset and vertically juxtaposed against the Espiritu Santo Formation (see Kerner, 2015). The fault has a several meters thick damage zone and well-developed fault core consisting of altered and deformed sedimentary and crystalline rock (Kerner, 2015) (Fig. 7a, 7b).

The fault core is fine-grained, phyllosilicate-rich, and dominated by cataclasite and fault gouge (Fig. 8a-d). The fault core is highly fractured at the micro- to macro scales. Abundant intragranular fractures, pressure solution seams, and microfaults cut quartz and feldspar grains that display undulatory extinction and sutured and bulging grain-to-grain contacts (Fig. 8a-d). Plastic deformational structures are regularly cut by brittle structures. At the micro-scale, grains adjacent to slip surfaces are intensely fractured and pulverized (Fig. 8a, 8b). Fractures have a preferred orientation (Fig. 8c, 8d) and are infilled with fine-grained phyllosilicates, iron oxides, and/or brecciated grain fragments. Multiple slip surfaces and microfaults anastomose through the highly fractured and deformed quartz and feldspar grains and recrystallized grains (Fig. 8a-d). Locally, a shear fracture is bounded by a microfracture damage zone and highly deformed grains and slickensided surfaces (Fig. 8a, 8b).

A several meter thick damage zone in the sedimentary and metamorphic rocks is characterized by large roughly vertical mineralized and unmineralized fractures (Fig. 7a-c) (Kerner, 2015). Several 0.5 to 1.0 cm thick fractures with coarse crystalline calcite infill and cataclasite margins cut the entire Espiritu Santo Formation (Fig. 7b, 7c) (Kerner, 2015). Fractures here terminate at the interface and cut into the crystalline basement. Structures in the sedimentary section appear spatially dependent on crystalline basement structures (e.g., Fig. 6e, 6f, 7a, 7e). Locally small-scale fractures and faults cut

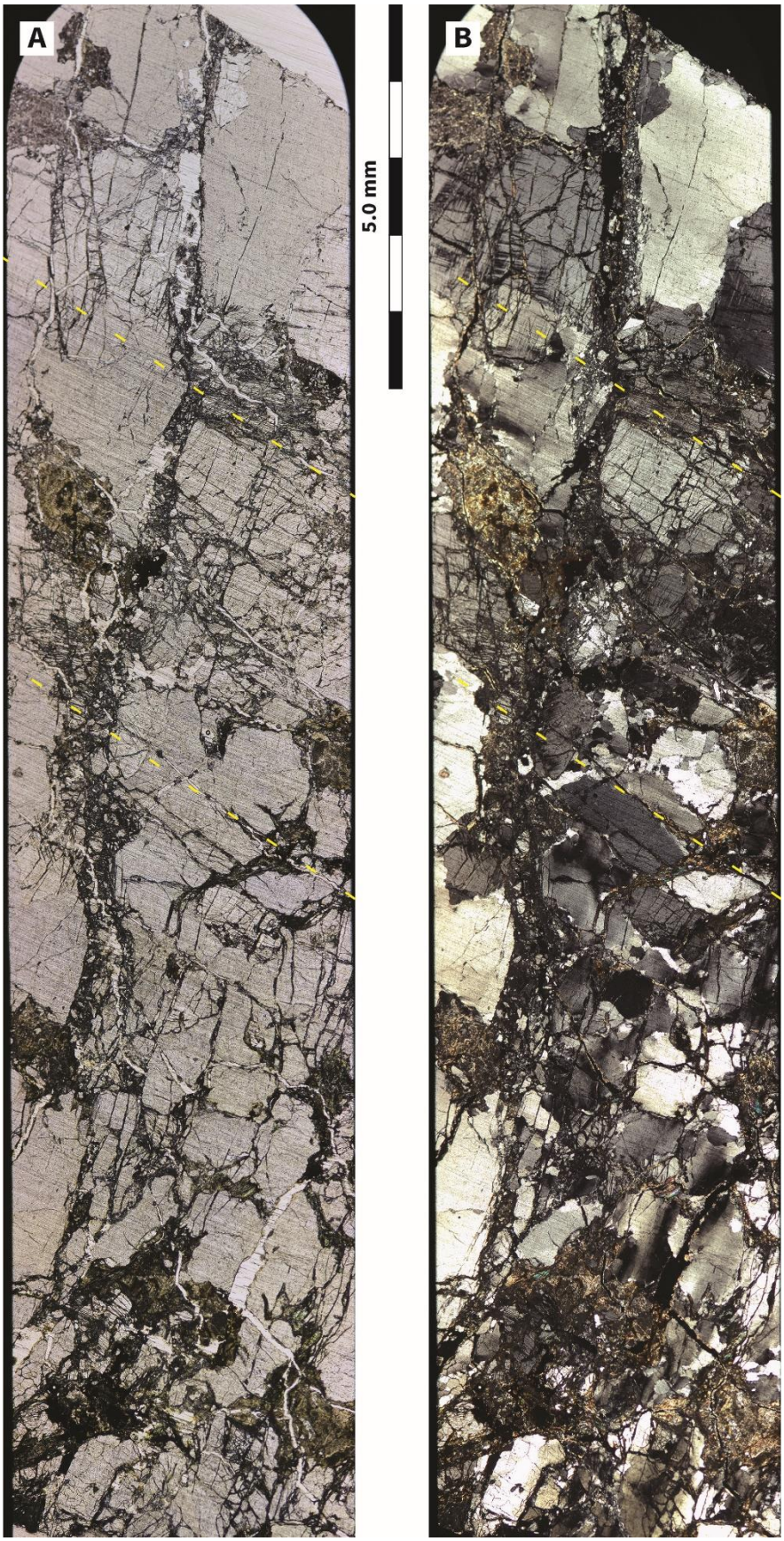

Figure 8. (A) and (B) continued next page.

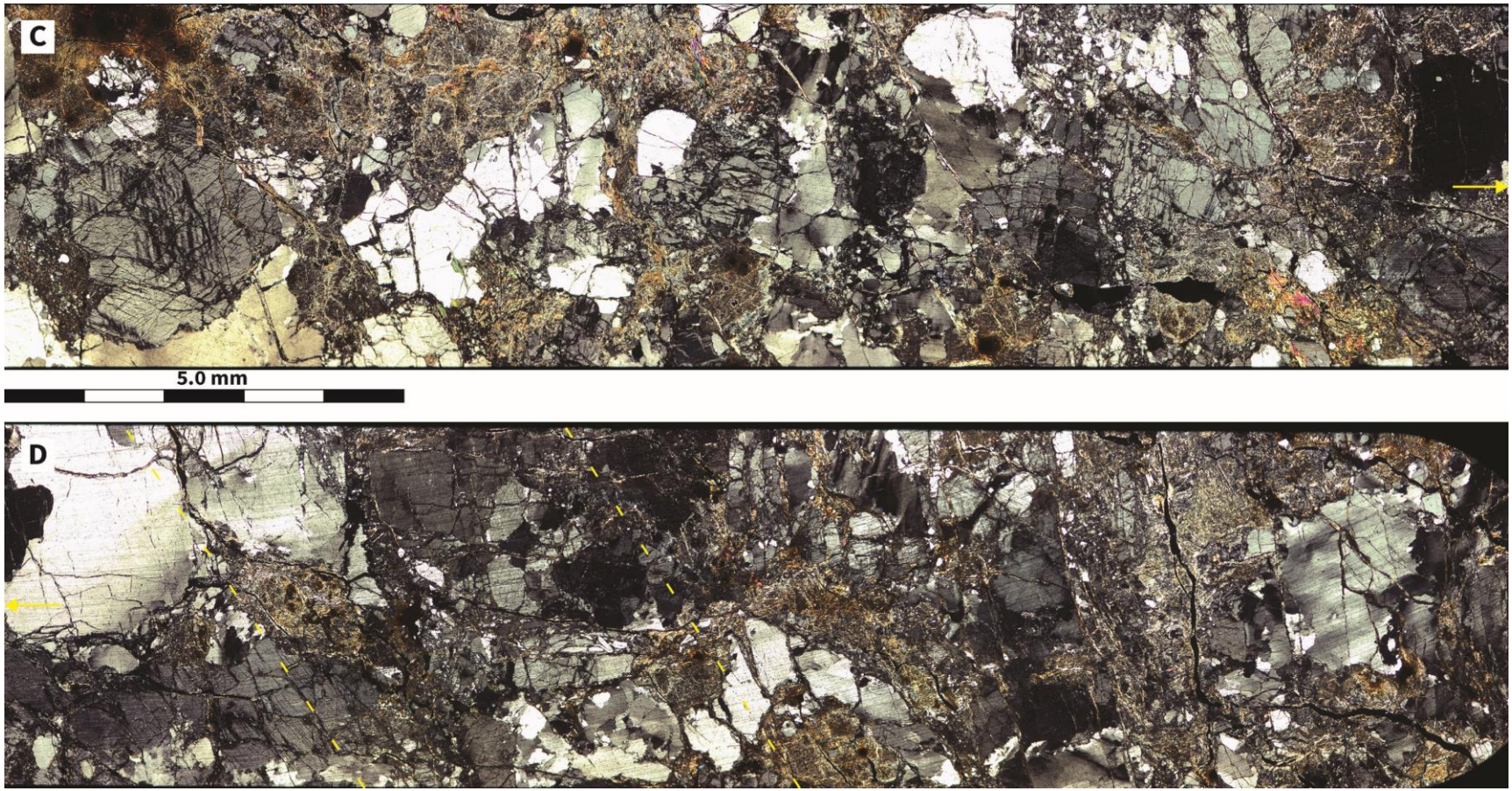

Figure 8 cont. Photomicrographs of foliated fault gouge and cataclasite from gneissic fault core of map scale fault (site O2). Sample O246 and associated microstructures. Scale bars are 5 mm. **(A)** Vertical sector subparallel to microfault trace. Angular fragments of quartz and feldspar grains. Sample is pervasively fractured and deformed. Note cataclasite and grain size reduction along slip surface. Fracture infill consists of fine-grained phyllosilicates, iron oxides, and brecciated wall rock material. Yellow dashed lines represent intersection with (D). (PPL). **(B)** Same area as (A). (XPL). **(C)** Horizontal sector subperpendicular to microfault trace. Pervasively fractured and deformed. Quartz grains display undulatory extinction and sutured grain contacts. Abundant intragranular fractures with grain scale displacement, deformation twins, and fined-grained phyllosilicates. Note network of microfractures trending NNW-SSE, parallel to subparallel to the fault trace in (A) and (B). (XPL). **(D)** Continuation of micrograph in (C) (yellow arrows). Yellow dashed lines represent intersection with (A) and (C). (XPL).

and offset the interface. An antithetic reverse fault with less than 1 m of offset (Fig. 6a) is located approximately 15 m NE of the map-scale normal fault. Where the basal sandstone is cut by the thrust fault, there are multiple carbonate slickensided fault surfaces.

The weathered horizon is calcite-rich, effervesces with hydrochloric acid, and cut by abundant white clayey structures which are present throughout the New Mexico field sites. The white features are laterally continuous, planar, locally slickensided, 0.3 mm to several cm thick, infilled with organic debris and inclusions of wall rock material, and are concentrated in the moderately to highly weathered crystalline basement rock (Fig. 6a-d). Several white clay infilled fractures, locally slickensided, emanate in a splaying and/or branching pattern from the fault surface of the small-scale thrust fault at site O2 (Fig. 6a, 6b). The majority of the features appear directly beneath the interface and form root-shape structures with preferred orientations that extend into the crystalline basement (Fig. 6d). Several recent modest rock falls and slope failures appear to have initiated, and root growth preferentially penetrates the crystalline basement, along these structures (Fig. 6d). Locally roots penetrate approximately 4 m of sedimentary rock and extrude out of crystalline basement structures. Modern root growth and water infiltration have enhanced the chemical and physical weathering of the surrounding rock mass, and roots are typically surrounded by white mineralization and alteration (Fig. 6d).

At site O2, the clayey features are composed of fine-grained phyllosilicates and calcite and have diffuse to sharp boundaries with highly weathered granoblastic gneiss (Fig. 9a). The weathered gneiss consists of quartz and feldspar aggregates in a clay- and calcite-rich groundmass (Fig. 9b). Feldspar grains have wedge-shaped deformation twins and are typically split along cleavage planes. The yellow to brown clays appear cut by

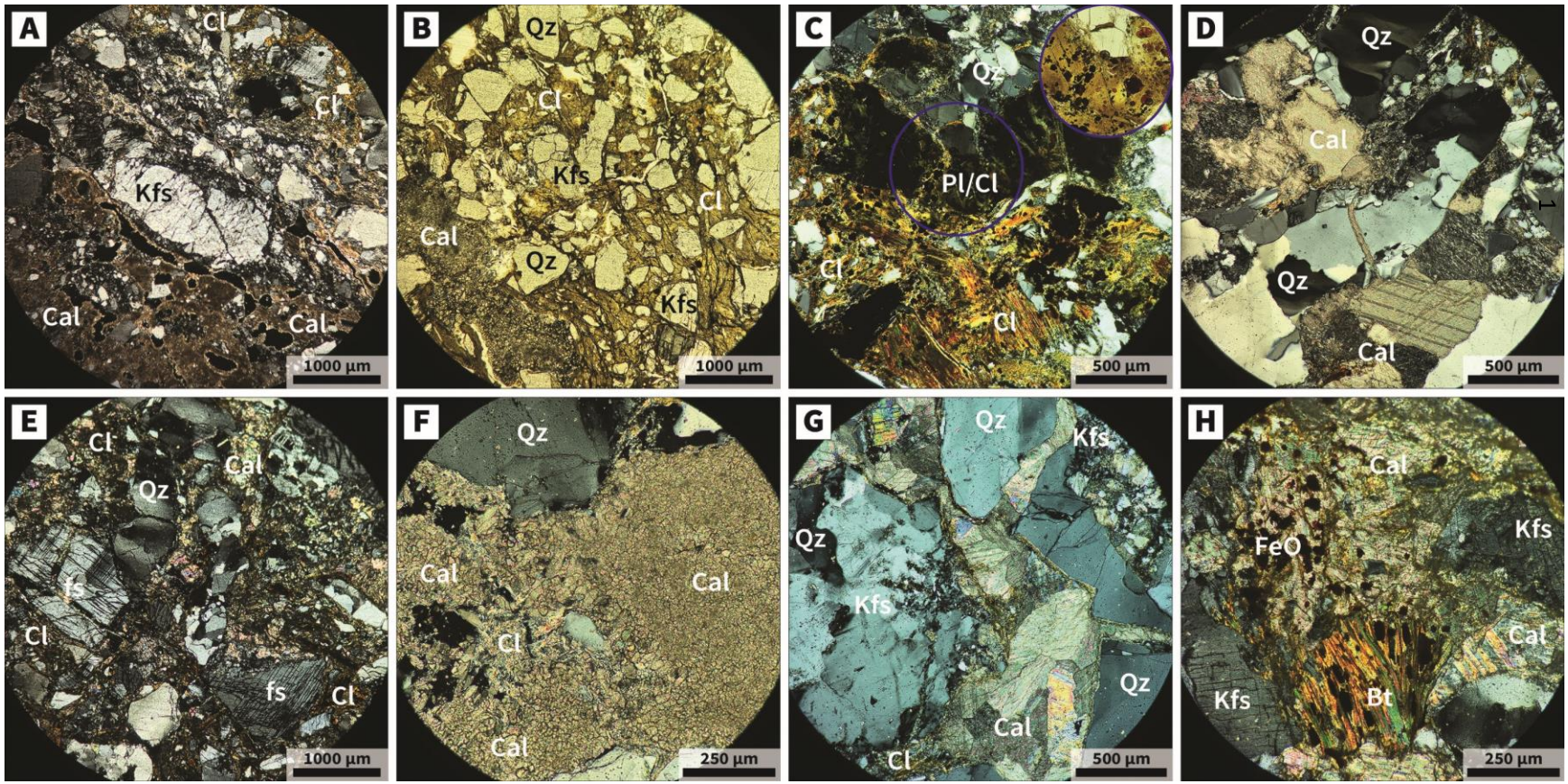

Figure 9. Photomicrographs of deformed and highly weathered gneiss cut by a fracture infilled with clayey material. Samples O241A,B, and O243A,B. **(A)** Highly fractured and deformed K-feldspar grain, and cataclasite on outcrop scale fracture margin. Fracture runs NW-SE, roughly parallel to long axis of K-feldspar grain. Note fracture infill contains abundant fine-grained micritic calcite. Wall rock consists of quartz and K-feldspar aggregates in a phyllosilicate-rich groundmass. (XPL). **(B)** Quartz and K-feldspar aggregates within a fine-grained calcite- and phyllosilicate-rich groundmass. Phyllosilicates are yellow to brown. (PPL). **(C)** Large grain replaced by nearly isotropic fine-grained clays, and iron oxides and/or hydroxides. Blue circle is PPL view. (XPL). **(D)** Undulatory quartz enclosed coarse-crystalline calcite cement and microfracture infill. Calcite displays tabular shaped deformation twins. (XPL). **(E)** Highly fractured aggregates in a fine-grained groundmass. (XPL). **(F)** Fine-grained micritic calcite. (XPL). **(G)** Recrystallized and deformed grains coated with fine-grained phyllosilicates. Sparry calcite fracture infill and cement. (XPL). **(H)** Biotite grain altered to secondary chlorite, smectite, and iron oxides. Quartz and feldspar grains surrounded by calcite cement. (XPL). Bt: biotite; Cal: calcite; Cl: phyllosilicates; FeO: iron oxide; Kfs: K-feldspar; Pl: plagioclase; Qz: quartz.

secondary fine-grained, polygonal, and micritic calcite (Fig. 9d-h). Calcium carbonate is also present as grain coating, and as coarse-grained sparry cement and fracture infill (Fig. 9g). Coarse calcite grains have tabular shaped deformation twins (Fig. 9g). Calcite dissolution is locally associated with an increase in void space and porosity. The fracture infill contains less K-feldspar and a higher percentage of fine-grained calcite and phyllosilicates than the parent rock (Fig. 9c). Locally, phyllosilicates, oxides and/or hydroxides are overprinted by calcite (Fig. 9h). Some of the white clayey structures are entirely contained within the weathered rock zone and coalesce with depth into unaltered and or slightly weathered joints and fractures within the unweathered to slightly weathered crystalline basement.

Site O3

The degree of weathering of the crystalline basement adjacent to the interface at site O3 ranges from fresh (Fig. 10a) to completely weathered (Fig. 10b). Locally a gneissic ellipsoidal corestone or block with exfoliation weathering features is topped by highly weathered gneiss (see Structural and Permeability Analysis). The ellipsoidal corestone marks a gradual horizontal transition from highly to completely weathered gneiss to the west, and fresh, unweathered gneiss to the east. Spheroidal and ellipsoidal corestones are abundant at all sites and displayed a range of shapes and sizes. Variable joint and fracture networks cut the crystalline basement. Joints and fractures in the weathered horizon are altered along their margins, and/or are infilled with secondary fine-grained phyllosilicates and calcite, and blend in with the surrounding rock mass. The joints are progressively less altered with increasing depth below the nonconformity. The

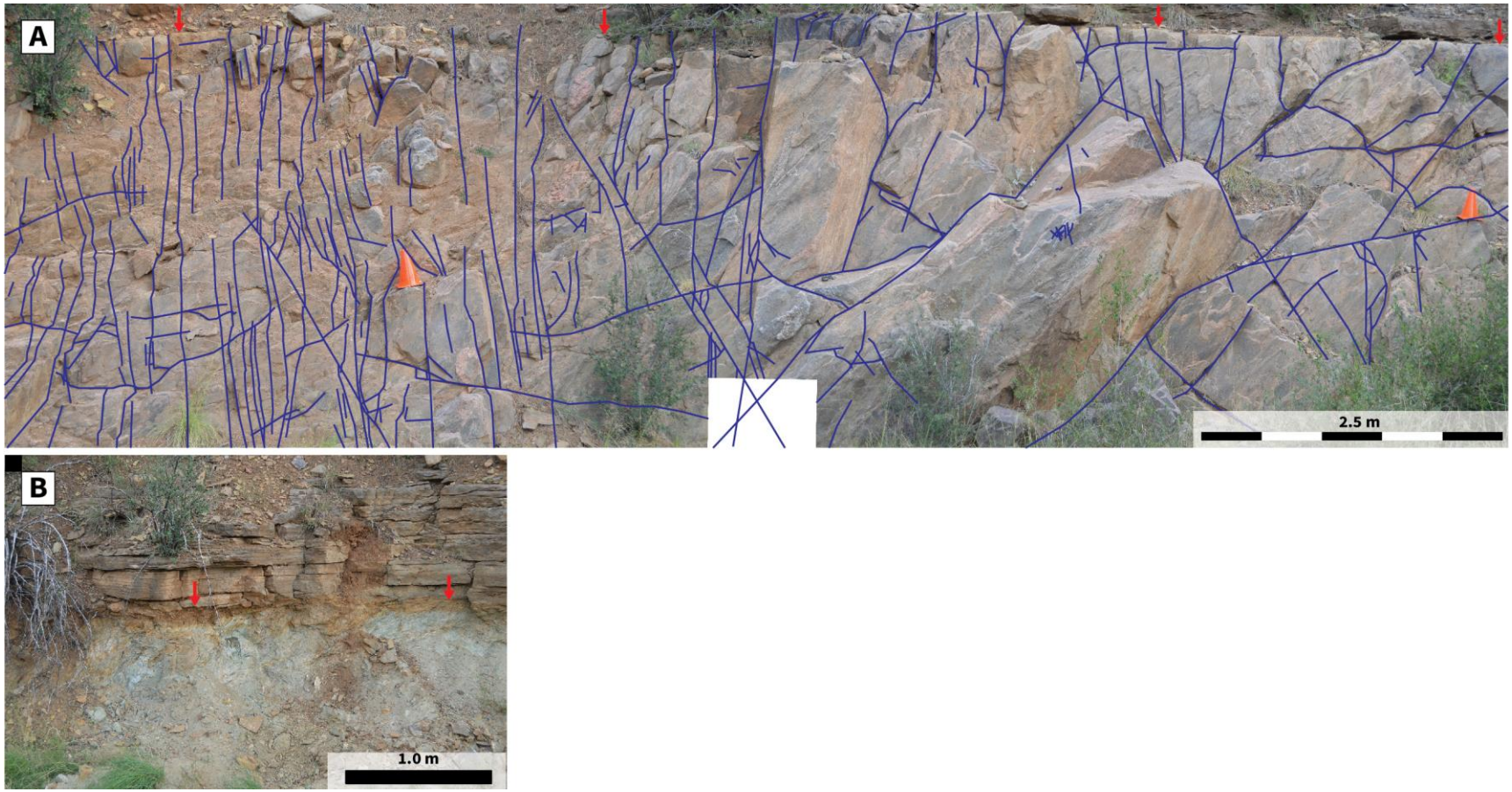

Figure 10. Photographs of lithological and structural features at site O3. **(A)** Fresh and unweathered gneiss to the east of Fig. 17a. Note a general increase in joint density towards the left side of photo. **(B)** Highly to completely weathered crystalline basement west of Fig. 17a. Blue: Fractures and Joints; Red Arrow: Nonconformity.

weathered rock extends to greater depths along joints, faults, and phyllosilicate- and mafic layers.

Site O4

A map-scale normal fault with a vertical offset of approximately 36.5 m cuts the nonconformity at site O4 (Fig. 1, 7e, 7f). The damage zone consists of a highly fractured crystalline basement and sedimentary rocks. The fault core and damage zone is more extensive, and fracture density higher (Fig. 7a) at site O4 than the fault core and damage zone and fracture density observed at site O2. The phyllosilicate-rich fault core is mostly covered by alluvium and overgrown with vegetation (Fig. 7f). The fracture network in the damage zone is highly chaotic (Fig. 7e). A thin discontinuous layer of the Del Padre Sandstone or medium to dark grey limestone tops the footwall gneiss (Fig. 7g). The footwall gneiss (Fig. 7f) and hanging wall gneiss (Fig. 7g) are variably weathered.

Petrography

Fresh to Slightly Weathered Rocks

The granitic gneiss, at sites O1 to O4, displays anhedral, granoblastic amoeboid, and inequigranular textures (Table 2). The fresh gneiss is competent and takes several blows with a hammer to induce breakage. A fresh gneiss sample from site O3 contains approximately 39.5% plagioclase, 34.5% quartz, 20.0% K-feldspar, 4.5% biotite, and 1.5% magnetite and opaque minerals, with minor muscovite, garnet, zircon, and sphene (Fig. 11a-h). The gneiss displays myrmekite, perthite, antiperthite, graphic, exsolution,

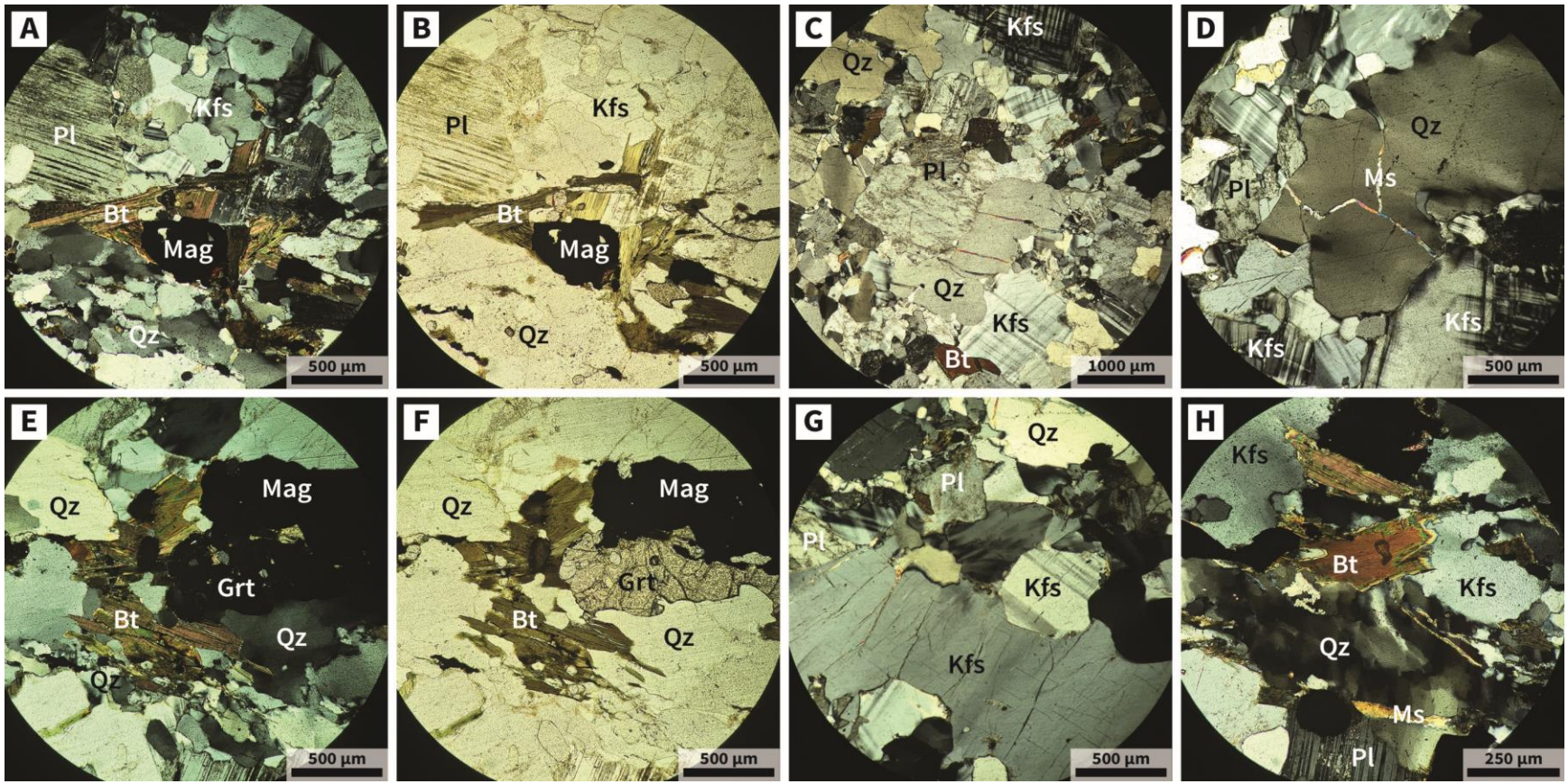

Figure 11. Photomicrographs of fresh granoblastic gneiss (O3P1#7), and associated microstructures. **(A)** Common mineral assemblage of quartz, plagioclase, K-feldspar, biotite, magnetite, and garnet. Incipient alteration of plagioclase to sericite. Plagioclase grains with polysynthetic twining displays differential sericitization of twin lamellae. (XPL). **(B)** Same area as (A). (PPL). **(C)** Incipient alteration of plagioclase to sericite gives grains a dusty appearance. Quartz and K-feldspar with irregular and bulging grain boundaries. (XPL). **(D)** Microcline porphyroblasts with tartan twinning. Undulatory quartz grain cut by intragranular fractures with muscovite infill. Interpenetrating grains, sutured grain boundaries, and abundant grain boundary triple junctions. (XPL). **(E)** Isotropic garnet and opaque magnetite grains surrounded by biotite laths. Incipient alteration of biotite to chlorite, which displays anomalous blue interference colors. Recrystallized quartz stringer below biotite grains. (XPL). **(F)** Same area as (E). Slight yellow staining along grain boundaries and intergranular fractures. (PPL). **(G)** K-feldspar grain with cleavage parallel intragranular fractures infilled with fine-grained phyllosilicates. K-feldspar grain displays signs of incipient dissolution, recrystallization, and grain boundary migration. (XPL) **(H)** Fresh biotite laths with birds-eye extinction. Subgrains in quartz with muscovite infilled microfractures. (XPL). Bt: biotite; Grt: garnet; Kfs: K-feldspar; Mag: magnetite; Ms: muscovite; Pl: plagioclase; Qz: quartz

and granophyric intergrowth textures. Plagioclase is dominated by albite and commonly displays characteristic polysynthetic twinning (Fig. 11a, 11b). Calcic and sodic plagioclase grains are variably altered and weathered to fine-grained phyllosilicates. Secondary alteration to fine-grained phyllosilicates is concentrated in sodic plagioclase grains and along fracture, cleavage, and twin planes (Fig. 11a-c). Quartz and K-feldspar are fine- to coarse-grained, appear transparent, and exhibit little or no alteration (Fig. 11a-h). Microcline grains display well-developed to patchy tartan twinning and contain spherical inclusions of quartz and plagioclase. Quartz grains are typically composed of subgrains, and display undulose extinction and sutured and bulging grain contacts (Fig. 11d-h). Undulatory extinction and sutured grain boundaries in quartz, and kinked deformation twins in plagioclase are evidence of incipient recrystallization and/or solid-state plastic deformation.

Deformation appears more prevalent in the dark bands composed of stringers of biotite, magnetite, garnet, and deformed and recrystallized quartz. Biotite laths are brown to dark brown and have undergone minor to moderate alteration to secondary chlorite and/or iron oxide and hydroxide (Fig. 11a, 11e, 11h). Magnetite grains have light brown to red replacement rims of hematite and/or iron oxide, and garnet grains are partially altered to biotite and chlorite (Fig. 11f). Intergranular and intragranular fractures are infilled with fine-grained phyllosilicates and/or iron oxides (Fig. 12a, 12b). Intragranular fractures isolated in individual grains occur preferentially along cleavage and twin planes (Fig. 12a, 12b). Staining, discoloration, and alteration is concentrated along joint, foliation, and fracture planes. As the fresh rock transitions to slightly weathered rock, there is an increase in dissolution and alteration of plagioclase and biotite grains to

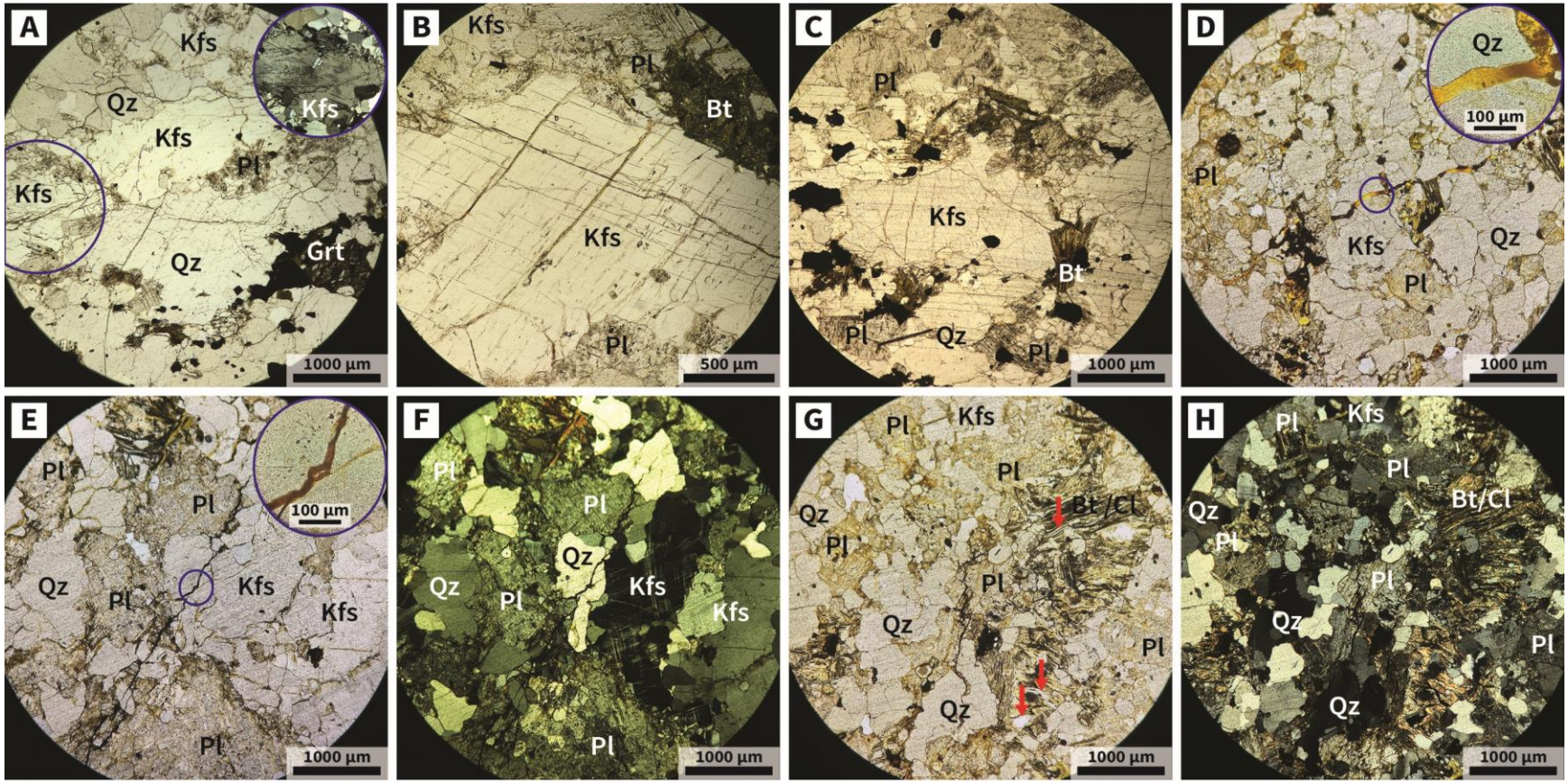

Figure 12. Photomicrographs of slightly to moderately weathered gneiss and associated microstructures. Similar composition to fresh gneiss in Fig.11. **(A)** Abundant intragranular and intergranular microfractures infilled with fine-grained phyllosilicates and iron oxides and/or hydroxides. Exsolution lamellae in K-feldspar grain cut by sericite veins (blue circle). Garnet altered to fine-grained phyllosilicates and iron oxides. Alteration of plagioclase to sericite gives grains a cloudy appearance. (PPL). **(B)** Cleavage parallel microfractures infilled with fine-grained phyllosilicates. Fractures display strong preferred orientation. Biotite laths altered to secondary chlorite and iron oxides. (PPL). **(C)** Intragranular fractures emanating from biotite lath into surrounding rock mass. (PPL). **(D)** Intergranular and intergranular fractures with illuvial clay (yellow) and iron oxide (black) infill. Magnified view (blue circle). Abundant grain boundary triple junctions. (PPL). **(E)** Plagioclase grains altered so secondary fine-grained phyllosilicates. Microfracture infilled (SW-NE) infilled with iron oxide. Magnified view (blue circle). (PPL). **(F)** Same area as (E). (XPL). **(G)** Biotite grains altered to secondary phyllosilicates and iron oxides which gives grains gray coloration parallel to cleavage. Increased porosity from biotite grains splitting along cleavage, and dissolution voids (red arrows). (PPL).**(H)** Same area as (G). (XPL). Bt: biotite; Cl: phyllosilicates; Grt: garnet; FeO: iron oxide; Kfs: K-feldspar; Mag: magnetite; Ms: muscovite; Pl: plagioclase; Qz: quartz.

secondary minerals (Fig. 12).

Moderately Weathered Rocks

In the moderately weathered gneiss (Fig. 12c-h), the plagioclase grains are cloudy and highly to completely altered to secondary fine-grained phyllosilicates. Minor dissolution and etching of K-feldspar grains give them a slightly dusty appearance (Fig. 12c). Locally dissolution voids in plagioclase grains adjacent to phyllosilicate-rich layers are infilled with secondary calcite. Biotite grains are altered to secondary smectite, vermiculite, chlorite, and/or iron oxide (Fig. 12c-h). Biotite grains are cut by numerous intragranular fractures and split along cleavage planes (Fig. 12g). Intragranular and intergranular fractures form an anastomosing network subparallel to foliation linking biotite, iron oxide, and miscellaneous secondary minerals (Fig. 12c, 12e). Grain size reduction is accommodated by grain scale fracturing and splitting along cleavage planes (Fig. 12b). An increase of iron oxide and hydroxide minerals gives the rocks a pale yellow-orange-brown coloration in thin section and hand sample (Fig. 12g). Moderately weathered rock adjacent to and cut by a fracture with phyllosilicate infill displays enhanced alteration, and a distinct mineralogical composition (Fig. 13a-h).

Highly to Completely Weathered Rocks

Highly to completely weathered rock (Fig. 14a-h) contains abundant intragranular and intergranular fractures that are regularly infilled with orange to brown to yellow clayey material. Fracture infill includes phyllosilicate, iron oxide, and calcite (Fig. 14b). Intragranular fractures at the grain scale are preferentially located along cleavage and

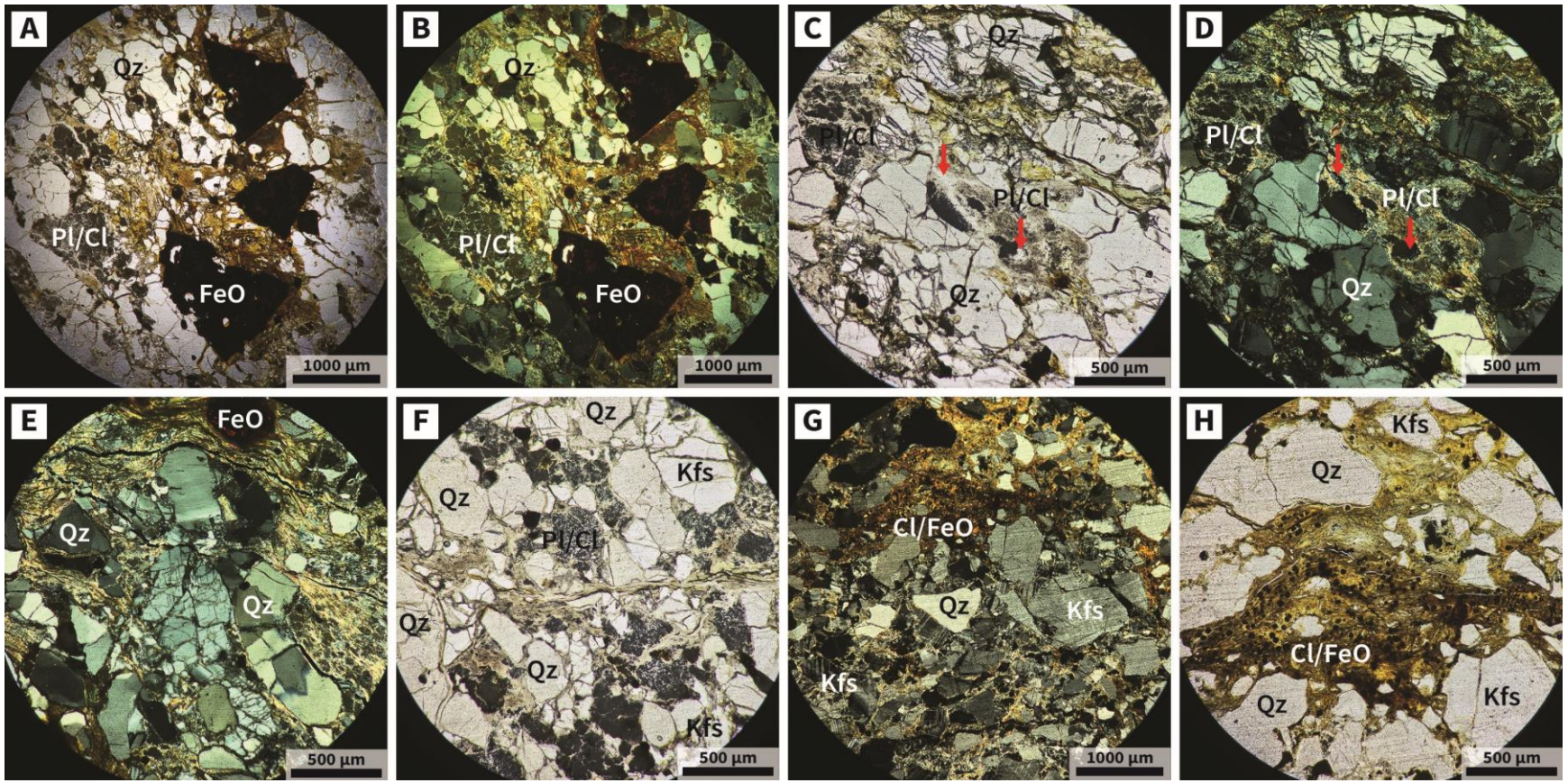

Figure 13. Photomicrographs of moderately weathered gneiss and associated microstructures. (A) - (F) from altered wall rock of outcrop scale fracture with phyllosilicate infill. **(A)** Large red to brown hematite and/or goethite grains. (PPL). **(B)** Same area as (A). (XPL). **(C)** Plagioclase grains completely replaced by secondary fine-grained phyllosilicates and amorphous silica?. Dissolution voids and clay infill with abundant porosity (red arrows). Abundant intragranular fractures. (PPL). **(D)** Same area as (C). (XPL). **(E)** Highly fractured grain in the center, surrounded by less fractured quartz grains and fine-grained phyllosilicates. (XPL). **(F)** Cloudy plagioclase grains completely altered to secondary phyllosilicates. Intragranular fracture network. (PPL). **(G)** Angular K-feldspar grains and lesser quartz in a network of fine-grained clays. (XPL). **(H)** Magnified view. Same area as (G). Biotite and plagioclase grains completely altered and replaced by fine-grained phyllosilicates and iron oxides. Iron oxides occur as small blebs. Cl: phyllosilicates; FeO: iron oxide; Kfs: K-feldspar; Pl: plagioclase; Qz: quartz.

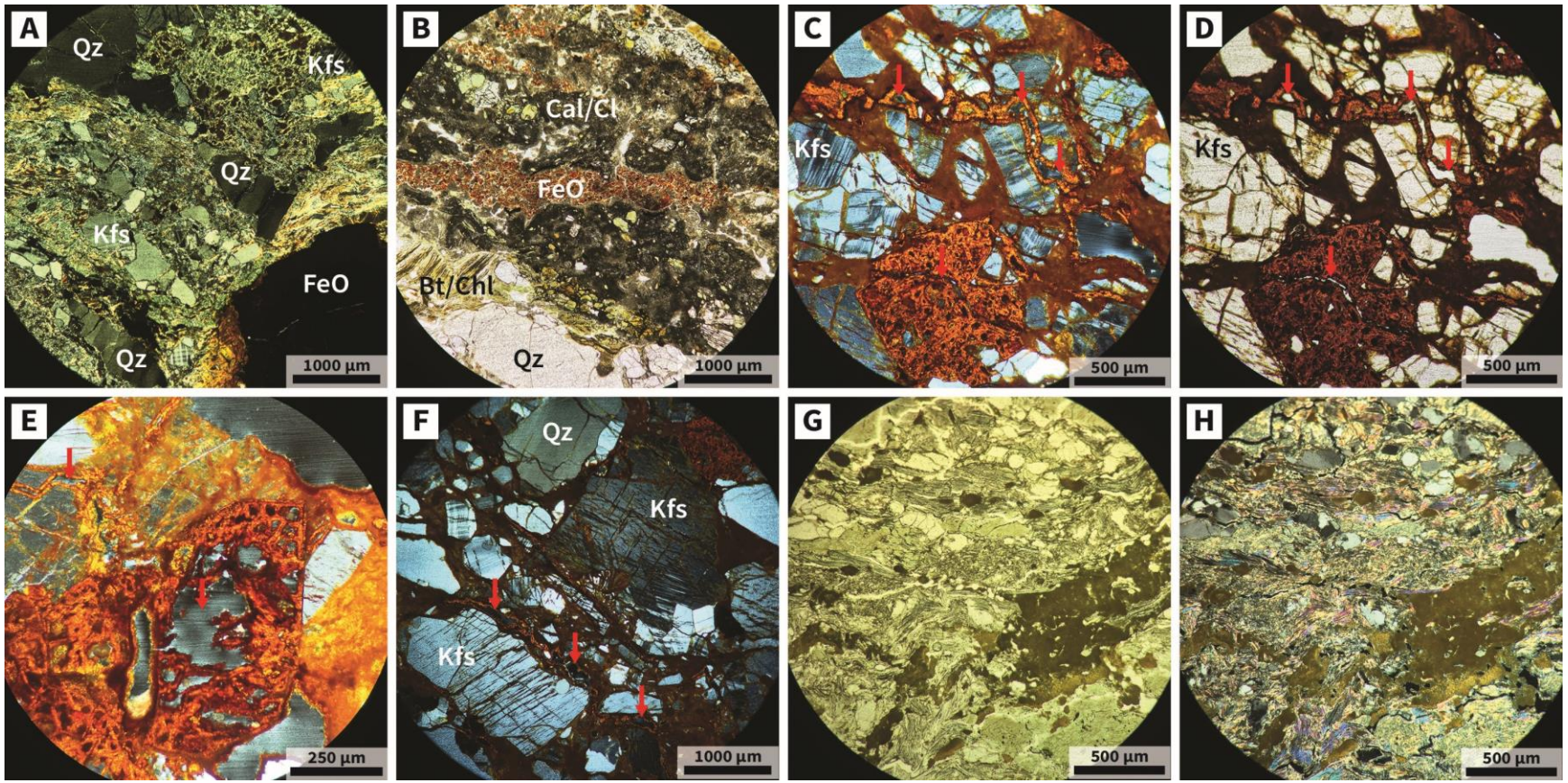

Figure 14. Photomicrographs of highly to completely weathered crystalline basement rocks, and associated microstructures. **(A)** Aggregates of quartz, and K-feldspar in a clayey groundmass. Note greater percentage of fine-grained material. (XPL). **(B)** Fine-grained phyllosilicate and calcite infilled microfracture, cut by hematite mineralization. Grains adjacent to and in fracture are highly fractured. (PPL). **(C)** Original rock fabric highly disturbed and decomposed. Grains appear suspended in an iron rich clayey groundmass, composed of orange-red-brown ferruginous minerals and eluviated clays. Intragranular fractures with void space along medians (red arrows). (XPL). **(D)** Same area as (C). (PPL). **(E)** Lithorelict clast with abundant void space. Note void space likely a combination of true void space and clasts removed during thin section preparation. (XPL). **(F)** Highly fractured feldspar grains. Anastomosing network of microfractures infilled with fine-grained material. (XPL). **(G)** Weathered amphibolite?. Original amphibole minerals are largely replaced by microcrystalline pale green to blue epidote, chlorite, and/or illite?. Elongate quartz grains. Fine-grained phyllosilicates constitute over 70% of sample. Mass of smetitic? clays. (PPL). **(H)** Same area as (G). (XPL). Cal: calite; Cl: phyllosilicates; Chl: chlorite; FeO: iron oxide; Kfs: K-feldspar; Pl: plagioclase; Qz: quartz.

twin planes. Fracture density and fine-grained phyllosilicate mineral abundance increase with increases in the degree of weathering (Fig. 14a). The remaining grains are broken up and appear suspended in the iron-rich groundmass (Fig. 14c-f). Dissolution and etching give the K-feldspar grains a dusty gray appearance. Plagioclase and biotite grains are pervasively altered to secondary phyllosilicates (Fig. 14c). The rocks are friable, and fine-grained phyllosilicates make up 40% and higher of the rock mass. Locally, abundant pore space is present in the clayey material along fracture medians and cleavage planes (Fig. 14c-f). However, the fine-grained mineralogy appears to bisect and/or separate the void space. Where present, iron and magnesium-rich mafic minerals are primarily transformed into secondary fine-grained material (Fig. 14g-h). The basal sandstone is composed of medium- to coarse-grained, poorly sorted, subangular grains with a brown to red-brown matrix (Fig. 15a-f). The mineralogy is dominated by quartz, with lesser feldspar and lithic fragments cemented by fine-grained-phyllosilicates, iron oxides, and lesser calcite.

X-ray Diffraction Results

We characterize the mineralogy of the rocks in the contact zone with XRD of the different altered and/or weathered zones identified by petrography (Table 2) (Fig. 16-18). The XRD spectra of the unaltered crystalline basement sample has a sharp narrow reflection at 10.00 Å (8.85 2θ), generated by fresh biotite and micas (Fig. 18). The plagioclase in the unweathered crystalline basement produces a strong reflection at approximately 3.18 Å (28.02 2θ), and 6.36 Å (13.92 2θ) and the plagioclase to K-feldspar ratio is approximately a 2:1. The relative intensities of the peaks attributed to plagioclase

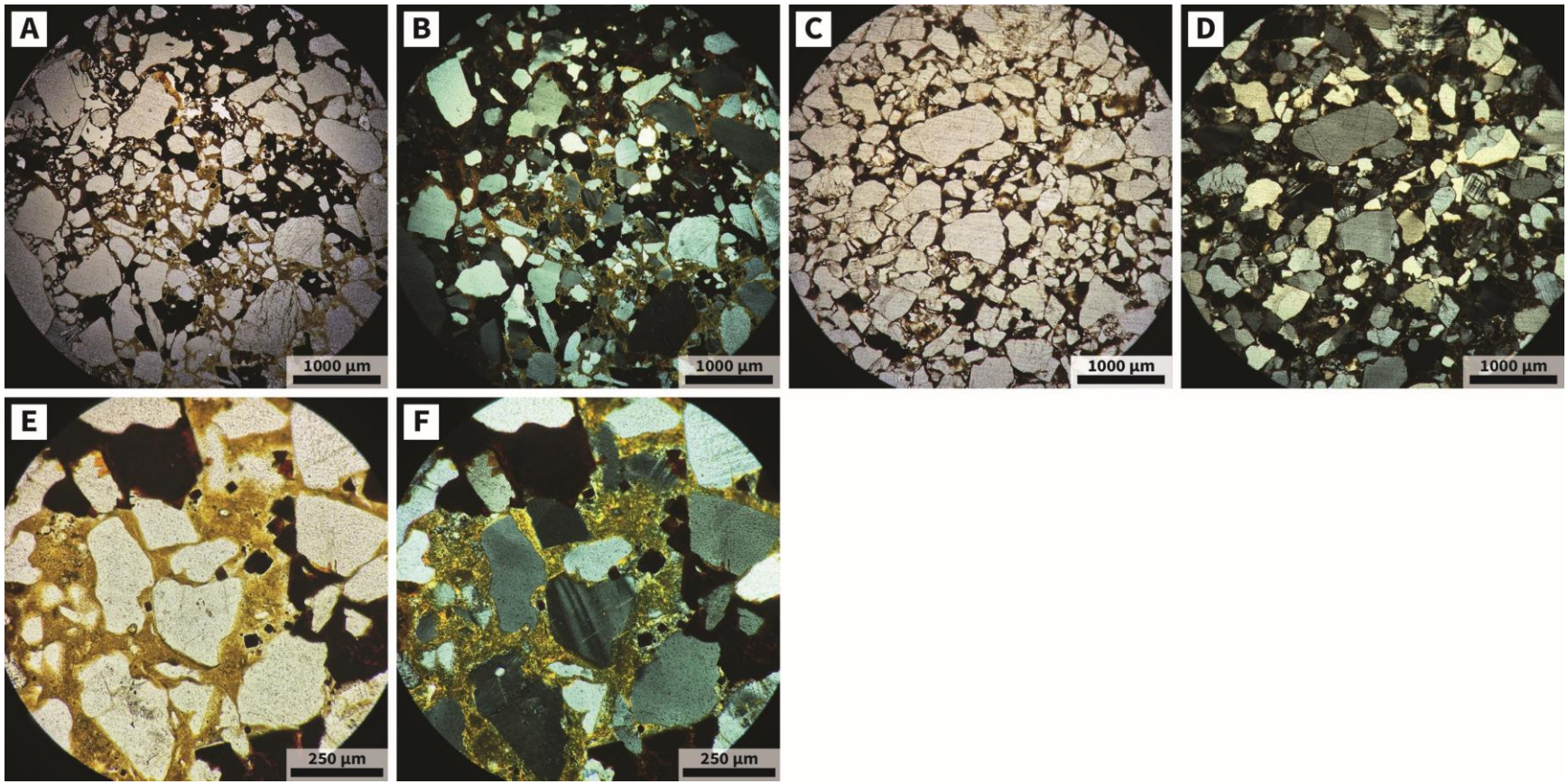

Figure 15. Photomicrographs of the basal Del Padre Sandstone, and associated microstructures. **(A)** Coarse-grained, poorly-sorted, and subangular grains. Pale brown to red-brown phyllosilicate, calcite, and iron oxide matrix. (PPL). **(B)** Same areas as (A). (XPL). **(C)** Matrix and cement dominated by dark brown iron oxide. (PPL). **(D)** Same view as (C).
(XPL). **(E)** Magnified view. Same area as (A) and (B). Note red euhedral iron oxide grains, and pale brown fine-grained phyllosilicates. (PPL). **(F)** Same area as (E). (XPL).

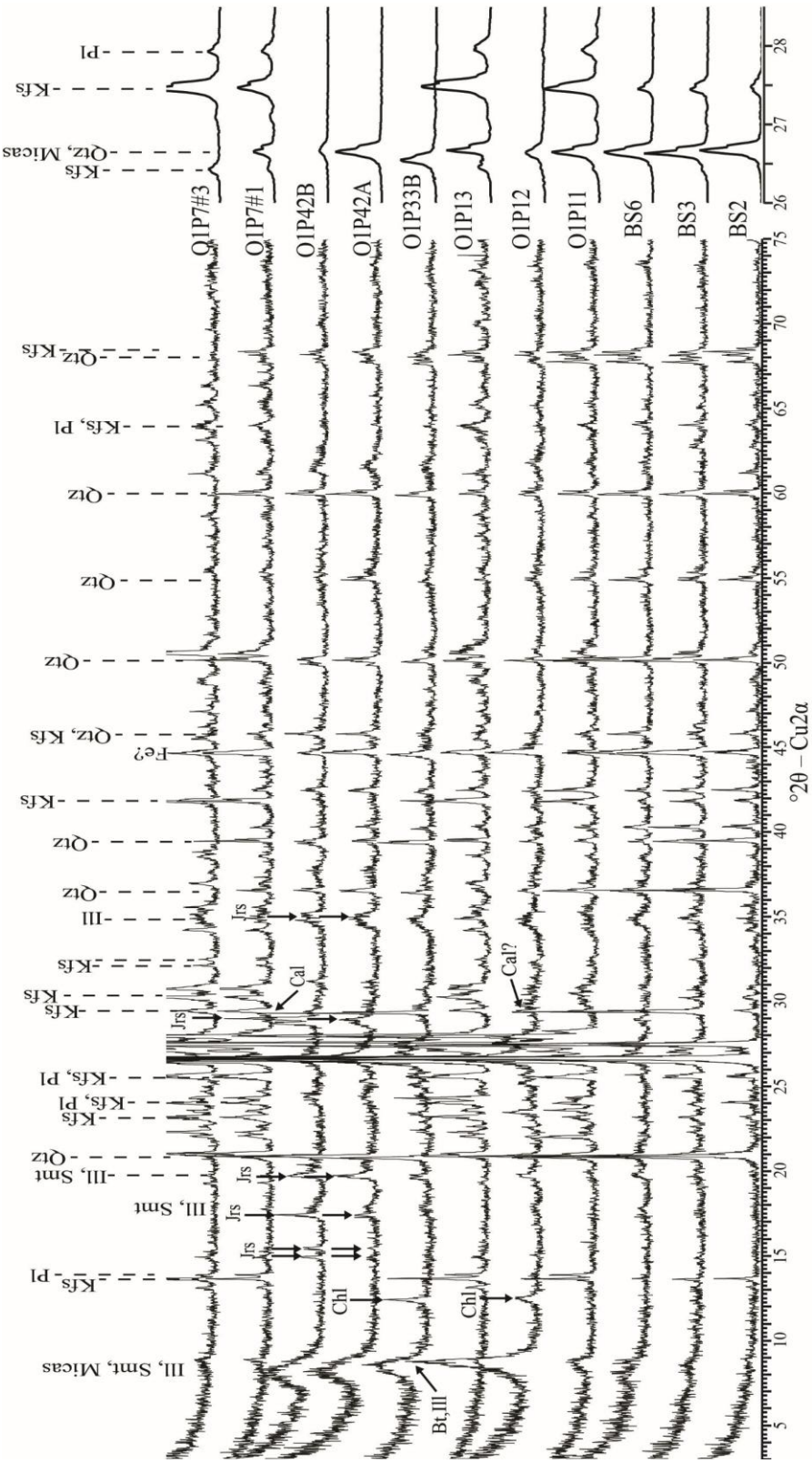

Figure 16. XRD patterns of bulk powder samples from site O1, with mineral peak positions labeled. Intensity versus °2θ – Cu2α. Right portion is a compressed view from 26.0 to 28.5 °2θ – Cu2α (Vertical scale = 0.066). Bio: biotite; Cal: calcite; Fe: iron; Ill: illite; Jrs: jarosite; Kfs: K-feldspar; Micas: mica group; Pl: plagioclase; Qtz: quartz Smt: smectite; ?: unknown. See Table 2.

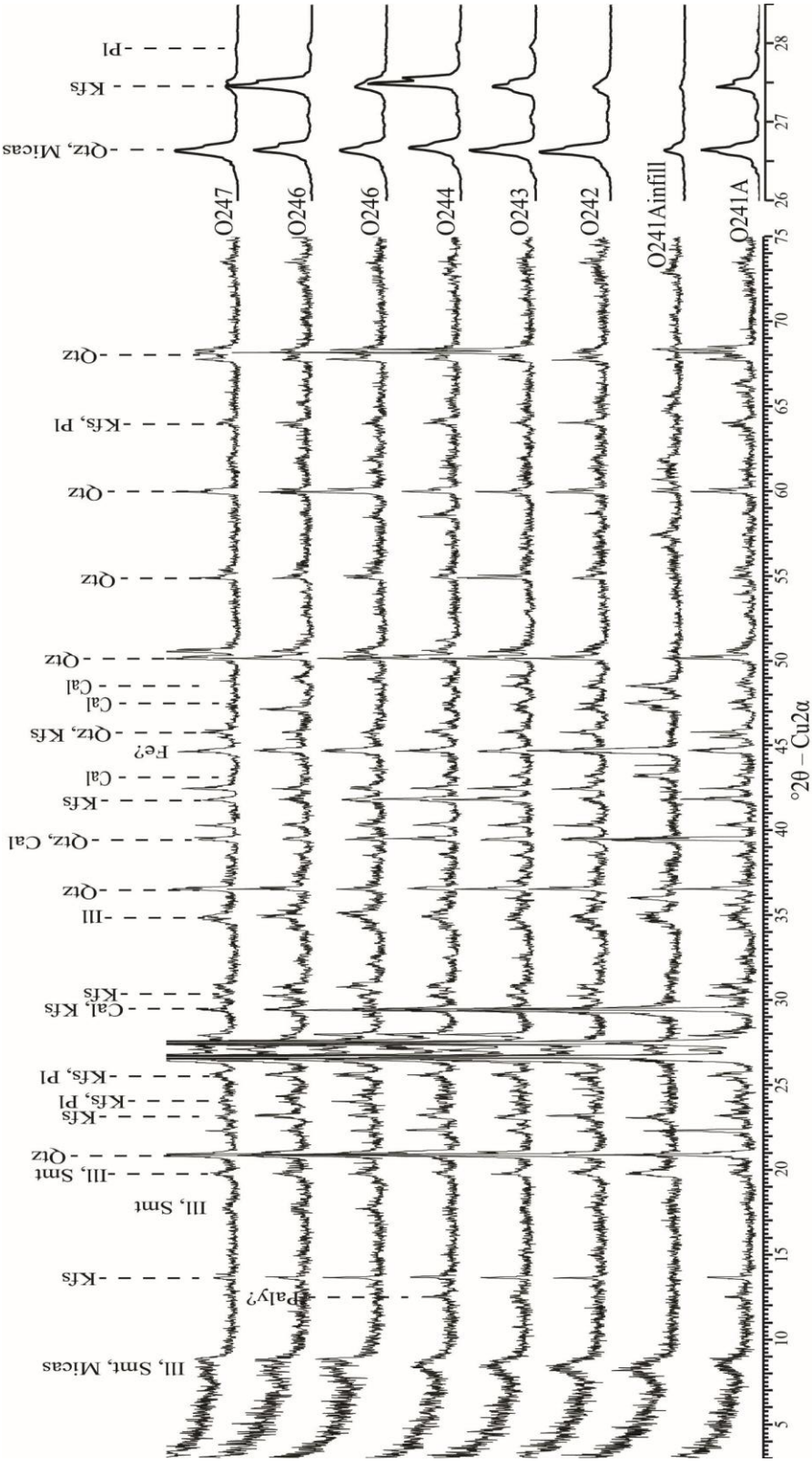

Figure 17. XRD patterns of bulk powder samples from site O2, with mineral peak positions labeled. Intensity versus °2θ – Cu2α. Right portion is a compressed view from 26 to 28.5 °2θ – Cu2α (Vertical scale = 0.066). Bio: biotite; Cal: calcite; Ill: illite; Kfs: K-feldspar; Micas: mica group; Paly: palygorskite; Pl: plagioclase; Qtz: quartz Smt: smectite; ?: unknown. See Table 2.

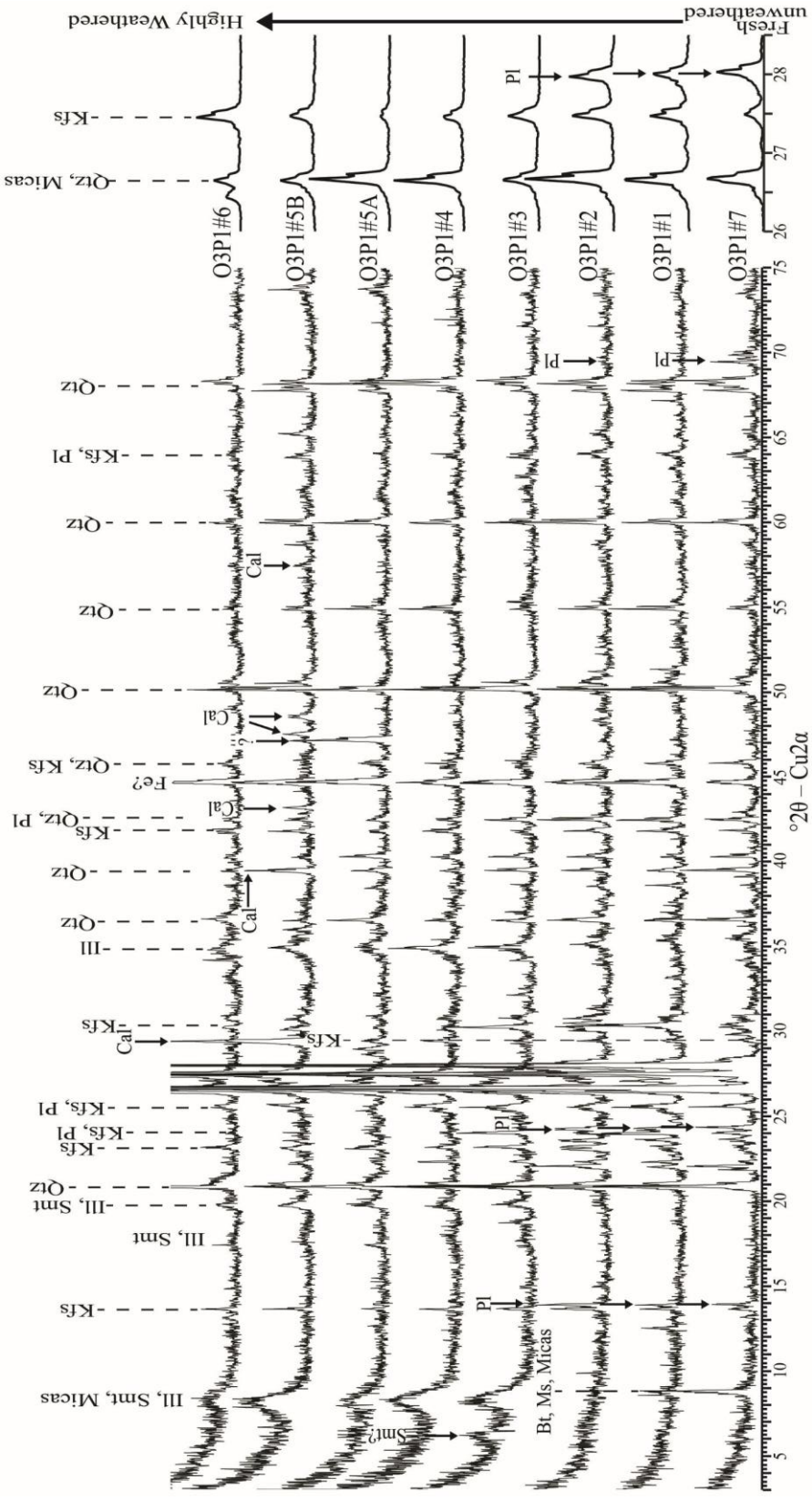

Figure 18. XRD patterns of bulk powder samples from site O3, with mineral peak positions labeled. Intensity versus °2θ – Cu2α. Samples are progressively more weathered from top to bottom. Right portion is a compressed view from 26 to 28.5 °2θ Cu2α (Vertical scale = 0.066). Bio: biotite; Cal: calcite; Fe: iron; Ill: illite; Kfs: K-feldspar; Micas: mica group; Pl: plagioclase; Qtz: quartz Smt: smectite; ?: unknown. See Table 2.

and biotite diminish in the slightly weathered samples and disappear entirely in the moderately to completely weathered samples. The relative intensities of the peaks attributed to K-feldspar at 3.24 Å (27.50 2θ) and 6.50 Å (13.63 2θ) increase and/or remain relatively consistent in fresh to slightly weathered samples. Fracture infill is typically associated with a decrease in peak intensity associated with K-feldspar. The relative intensities of the peaks attributed to quartz remain relatively consistent from fresh to completely weathered samples. The XRD peaks attributed to phyllosilicates within in the fault-related rocks and fracture infill are broader than the adjacent weathered rock (Fig. 17). The fracture infill contains less K-feldspar and a higher percentage of fine-grained calcite and phyllosilicates than the parent rock.

The moderately to completely weathered samples have broad peaks at approximately 10.70 Å (8.25 2θ), and 2.56 Å (35.00 2θ). An increase in phyllosilicate content with an increase in weathering grade is noted by the higher intensity and broader clay peaks and in the gradual diminishing of the quartz and K-feldspar peaks (Fig. 18). Locally the weathered horizon contains pedogenic calcite. Calcite is distinguished by its strong reflections at approximately 3.05 Å (29.40 2θ), 2.9 Å (39.50 2θ), and 2.10 Å (43.18 2θ). Plagioclase peaks are not present in moderate to completely weathered samples as plagioclase grains have undergone complete alteration to fine-grained phyllosilicates (Table 2). The broad peaks in the XRD spectra may indicate the weathered horizon is composed of a mixture of phyllosilicates including illite, smectite, and/or micas or variable degrees in sample crystallinity. Biotite altered to chlorite and vermiculite, and feldspars and mafic minerals have altered to illite and smectite. The joints and fractures in the moderately to highly weathered rocks are coated and infilled

with fine-grained illite and smectite clays. Green coloration and hues in the weathered rocks are attributed to the presence of smectite and/or illite. The broad asymmetrical peaks may be attributed to the presence of mixed-layer illite-smectite, resulting from the transformation of primary clays to mixed-layer illite-smectite (e.g., Lanson and Champion, 1991), or a result of using a fixed width slit window during the analyses.

Structural and Permeability Analyses

I characterize the megascopic fractures in the granitic gneiss at outcrops sites O1 (Fig. 19a-h) and O3 (Fig. 20a-i) with FracPaQ2D to understand the structural and permeability heterogeneity and anisotropy. Fracture traces are less apparent in the weathered rock, and it is likely some fractures traces were not mapped (Fig. 19b, 20b). These fractures typically had small apertures or were infilled with clay-sized material. FracPaQ uses a constant aperture approach to estimate permeability. Thus, their exclusion may provide a more accurate estimate. Trace length is visible trace length, and traces were typically censored by ground cover. The fractured rock mass permeability estimate does not take into account all exfoliation fractures or fractures that occur along foliation planes. Fractures that parallel foliation were difficult to distinguish in photographs, however, they were observed in outcrop.

The interconnectivities of the fracture networks in the crystalline basement plot near the base of the interconnectivity ternary diagram (Fig. 19g, 20g) indicating that they are cross joint and/or fracture networks, which typically contribute to enhanced permeability. Fracture trace lengths, at site O3, have a log-normal distribution (Fig. 20i). The crystalline basement contains more fractures than the overlying sedimentary units

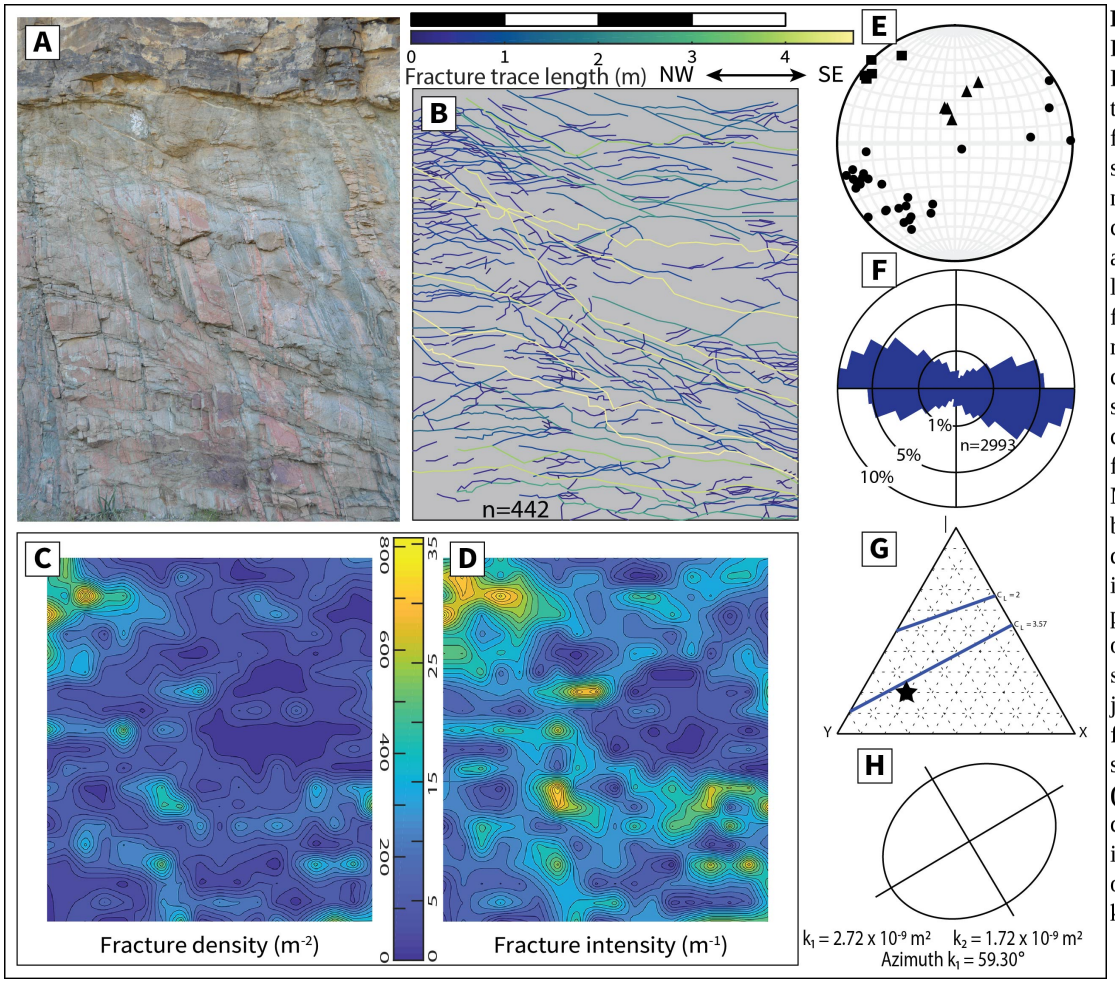

Figure 19. Fracture characterization and FracPaQ results from site O1. Outcrop of Del Padre Sandstone overlying weathered gneiss with typical compositional layering and joint and fracture patterns. Figures (A-D) are the same scale (Scale bar = 4 m). **(A)** Photograph of the nonconformity. Numerous faults and joints cut compositional layers in gneiss. A thrust fault with an apparent offset of 0.6 m juxtaposes gneissic layering. Slip was accommodated by multiple fault and slip surfaces. Surficial weathering along rock and fracture faces gives them a strong pink coloration. Joint planes in sandstone that subparallel outcrop face coated with white calcium carbonate. Red: unconformity; Blue: fractures; White: sample locations (O1P1). **(B)** Map of fracture trace length in the crystalline basement. **(C)** Map of estimated fracture trace density. **(D)** Map of estimated fracture trace intensity. **(E)** Equal area lower hemisphere projection of fracture, joint, and foliation plane orientation. Three dimensional orientations of structural features collected at site O1. Circles: joint/fracture; Square: foliation. Triangles: thrust faults **(F)** Equal area rose diagram of fracture segment orientation (2D) from (B). North is up. **(G)** Ternary plot of fracture segment connectivity. X: intersection; Y: abutment; I: isolated. **(H)** Permeability ellipse in the direction of flow of the fracture network.
$k_1 = 2.75 \times 10^6$ mD $k_2 = 1.74 \times 10^6$ mD

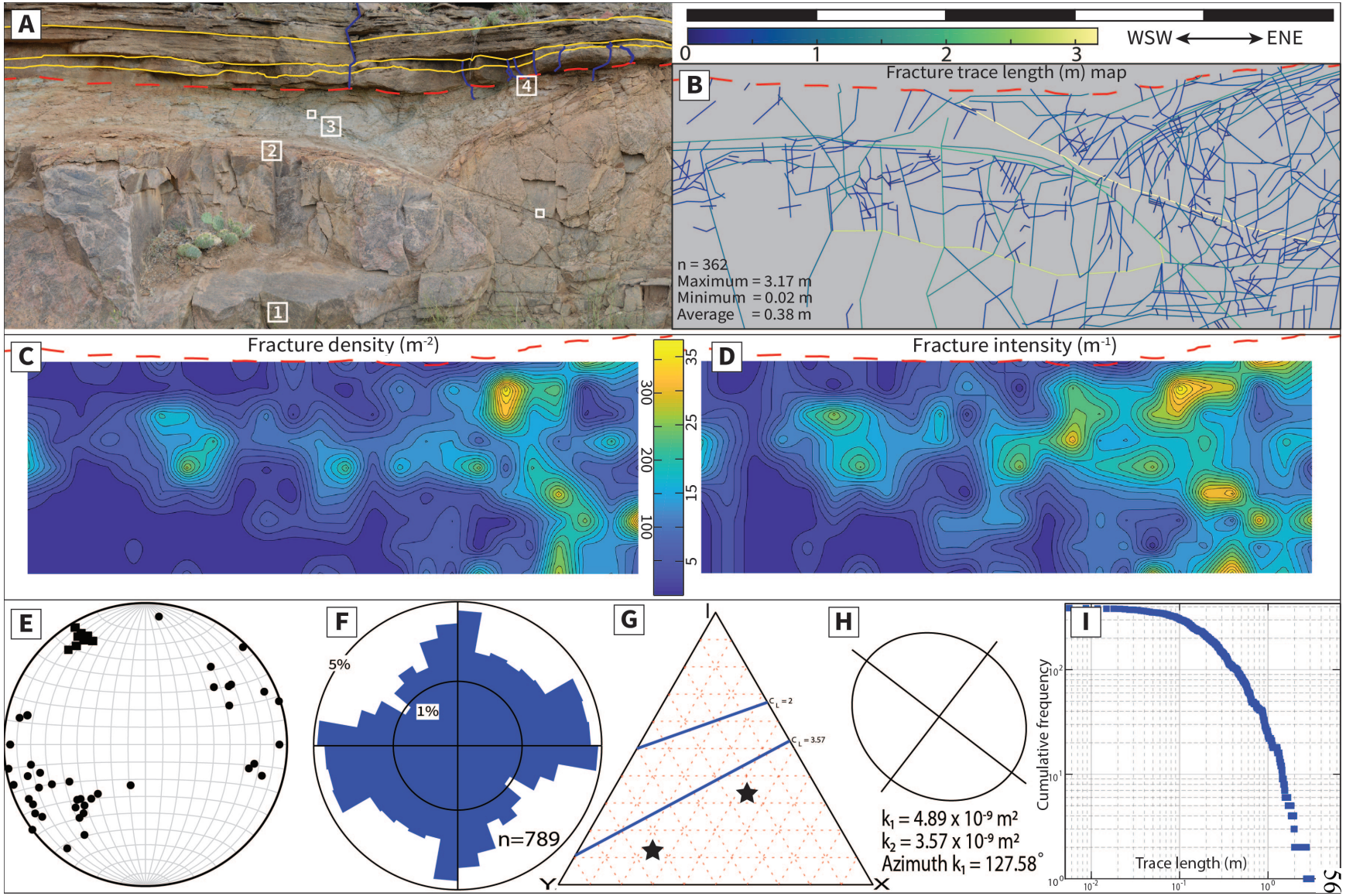
A
1
2
3
4
WSW
ENE
0
1
2
3
Fracture trace length (m) map
B
n = 362
Maximum = 3.17 m
Minimum = 0.02 m
Average = 0.38 m
C
Fracture density (m-2)
D
Fracture intensity (m-1)
35
25
15
5
300
200
100
E
F
5%
1%
n=789
G
I
X
Y
CL = 2
CL = 3.57
H
k1 = 4.89 x 10-9 m2
k2 = 3.57 x 10-9 m2
Azimuth k1 = 127.58°
I
Cumulative frequency
Trace length (m)

Figure 20. Fracture characterization and FracPaQ results from site O3. Outcrop of variably weathered gneiss truncated by the Del Padre Sandstone. Figures (A-D) are the same scale (Scale bar = 5 m). **(A)** Photograph of nonconformity, ellipsoidal corestone, and fracture network. The basal sandstone is crosscut by several fractures, with some traversing the interface. A joint plane in the sandstone (center top) is oriented subparallel to outcrop face. Red: unconformity; Yellow: bedding; Blue: fractures; White Squares: sample locations with number (O3P1). **(B)** Map of fracture trace length in the crystalline basement. **(C)** Map of estimated fracture trace density. **(D)** Map of estimated fracture trace intensity. **(E)** Equal area lower hemisphere projection of fracture, joint, and foliation plane orientation. Three dimensional orientations of structural features collected at site O3.Circles: joint/fracture; Square: foliation. **(F)** Equal area rose diagram of fracture segment orientation (2D) from (B). North is up. **(G)** Ternary plot of fracture segment connectivity. X: intersection; Y: abutment; I: isolated. **(H)** Permeability ellipse in the direction of flow of the fracture network. $k_1 = 4.95 \times 10^6$ mD $k_2 = 3.61 \times 10^6$ mD (I) Log-log plot of cumulative frequency versus trace lengths. Note log normal distribution.

(Fig. 20a). The fractures within the crystalline basement are dominantly truncated by the basal sandstone with lesser fractures cutting the interface (Fig. 19a, 20a). Locally an increase in fractures that cut the interface into the sedimentary units is observed proximal to outcrop scale to map-scale faults (Fig. 7), crystalline basement highs, and areas of high joint density in the crystalline basement (Fig. 6e, 6f). The highest apparent density of fractures is observed adjacent to map-scale faults that offset the nonconformity (Fig. 7).

Fracture and joint densities fluctuate spatially within the crystalline basement within the outcrops analyzed (Fig. 19c, 19d, 20c, 20d). This appears consistent throughout the field sites based on qualitative observations. The crystalline basement has abundant longitudinal fractures that cut and offset metamorphic layering (Fig. 19a). These fractures rarely extend into the sedimentary units, which also contain isolated and/or localized fracture networks. The basal sandstone displays minor jointing, with joint surfaces typically altered along their margins and/or infilled with calcium carbonate (Fig. 19a). The sandstone is sheeting off along these planes. The orientation of fracture segments at site O3 are relatively evenly distributed (Fig. 20f), whereas site O1 had a bimodal distribution (Fig. 19f). A higher percentage of fractures at site O3 appear to be the result of exfoliation weathering. The fracture networks in the crystalline rock results in inclined fracture and permeability anisotropy (Fig. 19h, 20h). At site O1 and site O3, the fracture network contributes to permeability anisotropy, with a maximum permeability approximately 1.56 and 1.37 times greater than minimum permeability. The permeability of sites O1 and O3 was calculated in FracPaQ using a fixed aperture width of 1 mm. Aperture width at depth can be significantly lower than 1 mm, and as aperture width decreases permeability decreases. The permeability calculated in FracPaQ varies

directly as the cube of aperture width.

Baker's Bridge Structure and Permeability

I examined one site along the nonconformity at the Durango site. Only one field day was spent at the Baker's Bridge field site. Therefore, the Baker's Bridge site was not analyzed to the same degree as the New Mexico sites. The Tamarron and McCracken Members have distinct cm to m scale beds with variable mineralogy, grain sorting, and angularity. The sandstone and crystalline basement rocks are jointed (Fig. 21a). Locally fractures cut the entire exposed sedimentary section. There is several meters of relief of the nonconformity surface (Fig. 21a). Joints and fractures cut the crystalline basement and are altered to and/or infilled with clayey material (Fig. 18b, 18c). The crystalline basement adjacent to the nonconformity is relatively fresh and unweathered (Fig. 18d).

TinyPerm values were collected at six locations within the basal beds of the Tamarron Member (Fig. 18a) (Table 3). Calculated permeability ranged from 1.19 mD to 2.78 mD. The permeability values are below the TinyPerm II's recommended threshold of 10 mD for accurate results. Twenty-three samples from the sedimentary units, analyzed in McBride, 2016, had an average porosity of approximately 1.12% and a median porosity of 0% (McBride, 2016). The low calculated permeabilities coupled with the low porosities (from McBride, 2016), likely indicates low matrix permeability within the Tamarron Member. The permeability of the sedimentary and crystalline rocks is likely structurally controlled.

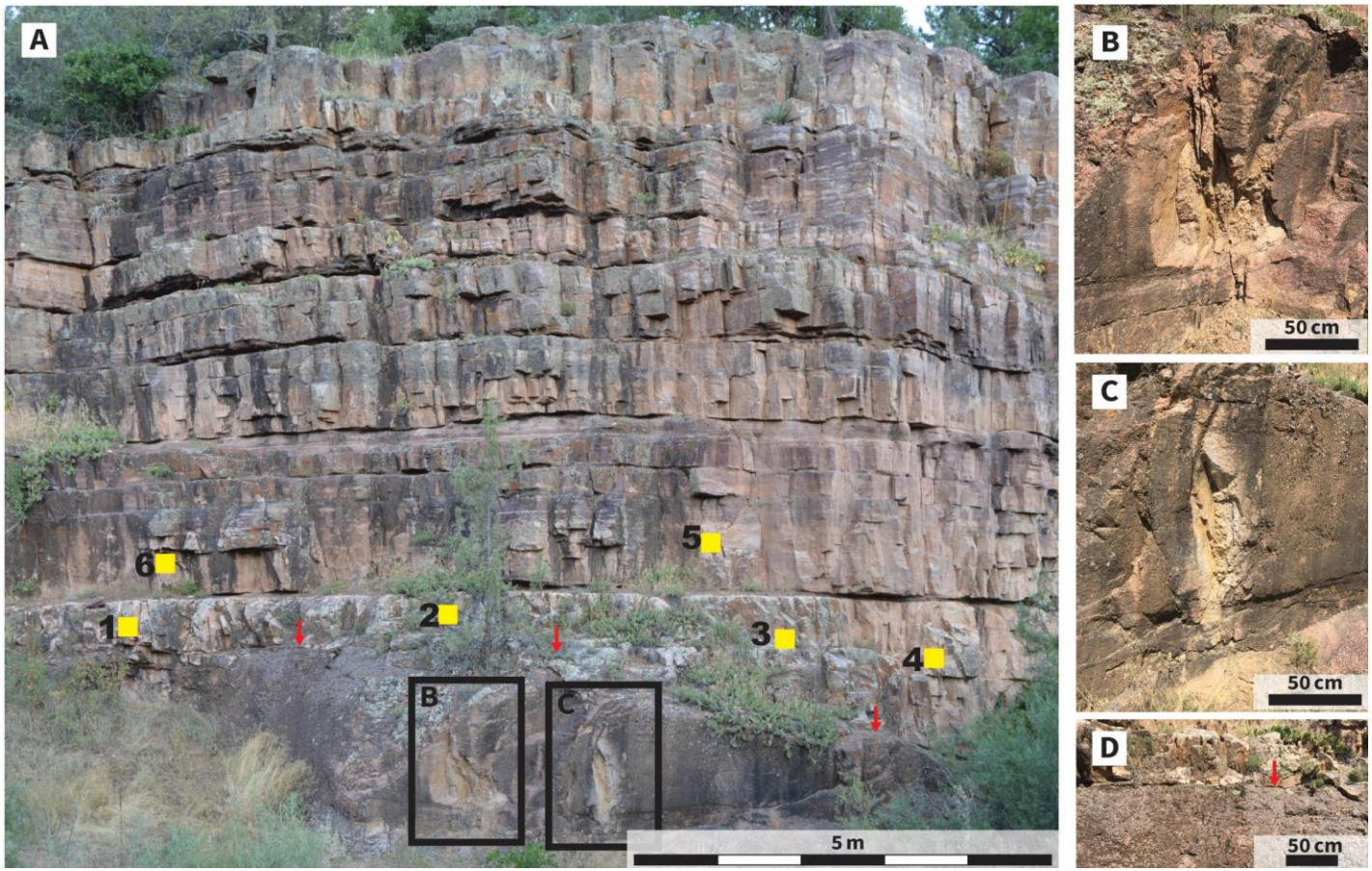

Figure 21. Photographs of the Baker's Bridge field site. **(A)** Tamarron Sandstone Member atop the Baker's Bridge Granite. Note the relief of the nonconformity. Overlying sandstone units are jointed. Yellow Squares: Location of TinyPerm II Measurement; Red Arrow: Nonconformity. **(B),(C)** Magnified view of fractures that cut the Baker's Bridge Granite, with signs of secondary alteration. (D) Magnified view of the nonconformity. The Precambrian basement is fresh and unweathered.

Table 3 Summary of TinyPerm II Portable Air Permeameter results at Baker's Bridge. T: TinyPerm II Value; K: Permeability (mD).

Location	T1	T2	T3	T4	T5	High T	High K	Average T	Average K
1	11.71	11.96	12.39	12.26	11.82	12.39	1.796	12.028	2.784
2	11.89	12.06	11.81	12.15	12.22	12.22	2.206	12.026	2.791
3	12.16	12.3	12.22	12.36	11.87	12.36	1.862	12.182	2.310
4	12.68	12.72	12.41	12.38	12.2	12.72	1.205	12.478	1.615
5	12.74	12.51	12.66	12.95	12.78	12.78	1.120	12.728	1.193
6	12	11.91	12.37	12.67	11.97	12.67	1.280	12.184	2.305

Interpretation and Discussion of Field Analog Sites

The evidence presented here, and of Kerner (2015) indicates that the crystalline basement adjacent to the nonconformity in the Gallinas Canyon exhibits thin zones of saprolith on the top of the Precambrian crystalline basement. Saprolith is generally divided into saprock, where the original texture is still mostly intact, and saprolite, where the rock texture is destroyed (Taylor & Eggleton, 2001). The saprolith developed atop a complex network of jointed, folded, and layered igneous and metamorphic rocks during subaerial exposure and weathering before deposition of the Mississippian sedimentary units. Lateral variation in the thickness of the saprolith and degree of weathering and/or alteration suggests that the crystalline basement likely underwent and/or were exposed to variable levels of exfoliation, weathering, erosion, hydration, leaching, and oxidation during subaerial exposure, before sedimentary rock deposition, pre-Mississippian. Weathering in the saprock was concentrated along joint, fracture, and foliation planes. Differential weathering and variable thickness of the saprolith was possibly controlled by crystalline basement structure and composition. The thickness of the weathered zone and fracture-rich zone, in a weathering profile, is controlled by topography and the base typically mirrors the topographic surface (Taylor & Eggleton, 2001; Clair et al., 2015). Therefore, our observations may be more representative of smaller-scale scale heterogeneities within the weathered crystalline basement.

The saprolite contains abundant corestones, secondary phyllosilicate, iron oxide, and carbonate minerals. The Del Padre Sandstone rests atop fresh crystalline basement, saprock, and saprolite. The degree of alteration and weathering of the crystalline

basement is most intense adjacent to the interface and dissipates with depth as rock grades to fresh crystalline basement. The thickness of the saprolite ranges from 0 to >5 m. The weathered crystalline basement adjacent to the nonconformity at site O2 is calcite-rich saprolith, which formed atop granitic crystalline basement. The phyllosilicate mineralogy of the saprolite is dominated by illite, smectite, and lesser vermiculite and chlorite. Kaolinite is a common weathering product of granitic rocks (Taylor & Eggleton, 2001); however, no kaolinite signature is present in the XRD analysis. It is possible kaolinite recrystallized to illite during burial diagenesis. A more detailed clay analysis would be needed to confirm this. In the saprolith, plagioclase and biotite grains have undergone moderate to complete dissolution and alteration to fine-grained phyllosilicates, and K-feldspars have undergone partial dissolution. Altered and etched feldspars can have elevated microporosity and permeability (e.g., Worden et al., 1990; Walker, 1990; Walker et al., 1995; Lee et al., 1995), and in the New Mexico rocks, microporosity is concentrated in the secondary phyllosilicates (Kerner, 2015). Generally, there is a positive correlation between weathering grade and porosity (Lumb, 1975; Taylor & Eggleton, 2001). Biotite grains in thin section were typically split along cleavage and linked together by an anastomosing fracture network. As biotite alters to vermiculite and/or chlorite an increase in volume occurs, which exerts pressure perpendicular to mineral cleavage (Delvigne, 1998). The fractures are infilled with clayey material and/or iron oxides likely sourced from the oxidation and weathering of primary minerals. The clayey material contains abundant voids and pore space.

At site O1 a well-developed ferruginous saprolite with an ‘iron crust' is present at the interface. The iron-rich saprolite contains iron oxide including goethite, limonite, and

lesser hematite. Goethite is a typical product from the weathering mafic rocks and may indicate precipitation of iron under humid oxidizing conditions (Taylor & Eggleton, 2001). Iron released and mobilized from the weathering of iron-rich minerals was precipitated as iron oxides and hydroxides. Oxidation of the iron-rich rock gives them a distinctive yellow to orange to brown color. Hydration, oxidization, and weathering of pyrite commonly result in the formation of jarosite that commonly occurs with iron oxide and hydroxide, calcite, and quartz (Taylor & Eggleton, 2001).

Locally, root-shape structures form branching and splaying patterns, extending into the crystalline basement, that emanate from the nonconformity and/or fault surfaces that cut sedimentary rocks and crystalline basement (Fig. 6). The white clay-rich structures are typically infilled with fine-grained phyllosilicates and carbonate and coalesce into joint, shear fracture, exfoliation fracture, and foliation planes within the crystalline basement (Fig. 6). The structures are dominantly located in moderately to highly weathered rock and dissipate with depth. Locally, the white infill clogs and/or cuts into the basal sandstone member (Fig 6g). The fault core and fracture infill produced distinctive XRD spectra compared to the surrounding weathered and unweathered crystalline basement (Fig. 17). This includes smaller and less defined peaks associated with K-feldspar, and broader peaks attributed to phyllosilicates (Fig. 17). This may be related to the dissolution of K-feldspar and reprecipitation, and neocrystallization to fine-grained phyllosilicates, and/or fault-related clay mineralization. High phyllosilicate content and a decreased plagioclase content within the uppermost samples collected from the crystalline basement supports formation as a result of weathering. Locally, the fine-grained phyllosilicates and primary carbonates were possibly replaced, to varying

degrees, by secondary carbonate while immobile iron oxides and/or hydroxides stayed in place. Calcite grain growth may have been retarded and/or influenced by the fine-grained phyllosilicates (e.g., Wieder & Yaalon, 1974), resulting in the micritic textures. In some areas, coarse carbonate cement and infill cuts fine-grained calcite which suggests multiple phases of carbonate. It is possible sections of crystalline basement may have experienced alteration coeval with the dolomitization, dedolomitization, silicification, calcification of evaporites, and brecciation of the Arroyo Penasco group (See Ulmer & Laury, 1984).

Calcite- and hematite-rich slip surfaces and carbonate infilled fractures that cut the sedimentary and crystalline rocks indicate hydrological communication between the units. The carbonate infilled fractures, which occur at every field site, suggest the hydrological communication may have been widespread. The presence of jarosite and serpentine clay minerals, branching fracture patterns, calcite, clay, hematite veins, recrystallization textures, and lateral alteration in the Del Padre Sandstone may provide evidence of hydrothermal alteration proximal to the interface. However, more detailed geochemical analyses on the gneissic and mafic rocks and sampling of the rocks at greater depths is needed to substantiate. Variable grain sorting in the basal sandstone may have facilitated fluid flow localization and enhanced fluid-rock interaction and alteration of the basal strata of the Del Padre Member. Our FracPaQ results show that fracture network heterogeneity within the crystalline basement likely contributed to permeability anisotropy. The matrix permeability of the sedimentary rocks at Baker's Bridge (Table 3) are several orders of magnitude lower than the permeability of the fractured crystalline basement at the Gallinas Canyon (Fig. 19, 20). The permeability of the fracture network

would be dependent on aperture width.

Based on the data presented above, I hypothesize that alteration and fluid migration, associated with weathering and secondary fluid-rock interactions, preferentially occurred along fractures, faults, and joints within the crystalline basement. I interpret the white clay-rich structures infilled with secondary fine-grained phyllosilicates and carbonate as joint, shear fracture, exfoliation fracture, and foliation planes that have undergone secondary deformation, dissolution, and alteration which is supported by macro- to microscopic evidence including the presence of secondary clays, sparry and micritic calcite, dissolution textures in feldspars, fractured and faulted grains, and slickensided surfaces. The white infilled fractures are generally limited to moderately to highly weathered rock, which may indicate enhanced permeability and/or porosity in fractures within the saprolite zone, that may have facilitated fluid migration between the basal sedimentary rocks and crystalline basement resulting in hydrothermal and/or fluid related overprinting of the saprolith.

Macroscopic evidence including foliation and fault core parallel calcite veins, shows phyllosilicate mineral alignment in foliation and/or fault gouge may have contributed to enhanced cleavage parallel fluid flow. Micro- and macroscopic evidence in the fault core at site O2, including multiple slip surfaces, shear fractures, overprinting of plastic and brittle deformational structures, highly deformed and fractured and recrystallized quartz and feldspar grains, all indicates multiple episodes of slip, slip localization and possibly repeated healing, recrystallization, and reactivation. Mineralized and unmineralized fractures cut the nonconformity adjacent to map-scale faults that offset the interface which is evidence of fault enhanced hydrogeologic communication between

the sedimentary rocks and crystalline basement.

Alteration, reduced grain size, and foliation, fracture, and joint planes can contribute to a weaker rock mass (Goodman, 1989). Feldspars altering to fine-grained phyllosilicates is a reaction weakening process (e.g., Evans, 1988). Fractures, joints, bedding, and foliation planes with smoothed surfaces, and/or phyllosilicate infill can have low to no cohesion and a reduced shear strength compared to the surrounding rock. An increase in fine-grained phyllosilicates in the saprolite zone likely coincides with a less competent rock mass. Faults have been observed to be weak (e.g., Zoback et al., 1987; Holdsworth, 2004), and can further weaken with the addition of fluids (Byerlee, 1978; Rice, 1992; Wintsch et al., 1995). The map-scale faults in New Mexico display signs of repeated deformation and have cataclasite and fine-grained phyllosilicate-rich cores. A low percentage of weak minerals can weaken a fault zone (e.g., Wintsch et al., 1995; Moore & Rymer, 2007; Niemeijer et al., 2010). The white structures are planes of weakness in the rock mass as shown by the presence of several modern rock falls and slope failures.

The saprolite and more competent fresh crystalline basement would likely behave differently under stress changes. The high porosity, calcium carbonate and fine-grained phyllosilicate-rich, and weak saprolite would likely undergo primarily ductile deformation (e.g., Kerner, 2015), while the quartz- and feldspar-rich competent fresh crystalline basement would likely undergo brittle deformation. The saprolite and/or phyllosilicate-rich rocks would likely have a decreased tensile strength. A strength contrast may explain why extensional calcite veins occurred parallel to preexisting fracture and phyllosilicate-rich foliation planes in New Mexico rocks. Competent and

fresh crystalline basement would be able to accommodate higher differential stress. However, based on the Mohr-fracture criteria this competent rock may require less pore fluid pressure to induce failure. The strength of the preexisting planes of weakness is dependent on their orientation and the orientation of the stress field. If the planes of weakness are 'optimally oriented', shear failure can occur under lower differential stress. Elevated fluid pressures can reduce shear strength and induce shear failure spurring fracture growth and linkage (e.g., Byerlee 1978; Cox et al., 1991; Sibson, 1994). Strength contrast within the crystalline basement may explain the uneven outcrop face observed in the field. The sandstone ledges are more pronounced where the crystalline basement is highly weathered, possibly because the mechanically weaker rock has eroded more readily.

The fine-grained phyllosilicate-rich weathered horizon and fault cores have elevated porosity. However, they likely represent low permeability barriers or exhibit anisotropic permeability. Crystalline basement permeability is dominated by interconnected joint and fracture networks. These fracture networks contribute to permeability anisotropy and may provide fluid pathways and/or increase the hydraulic communication between the basal reservoir and crystalline basement. The permeability of the fracture network is dependent on the fracture aperture, and it is possible the fracture and/or joint apertures could be closed at depth. However, they could still be planes of weakness.

MICHIGAN RESULTS

Geologic Background of the Upper Peninsula, Michigan

The geologic history recorded in the Precambrian rocks of the western Upper Peninsula of Michigan dates to the Archean, through the development of the Neoarchean Great Lakes tectonic zone, the Paleoproterozoic Penokean Orogeny, and the Late Mesoproterozoic Mid-Continental Rift (MCR). The Great Lakes tectonic zone formed during a continental collision at approximately 2.7 Ga (Sims et al., 1980). The 2.7 Ga Canadian Shield is located to the north, and the 3.5 Ga Superior Province located to the south (Sims et al., 1980). The 1.8 Penokean Orogeny resulted from the collision of an oceanic-arc terrane with the cratonic Archean Superior terrane (Schulz and Cannon, 2007). Shallow seas that filled extensional basins during the orogeny resulted in the deposition of banded iron formations (Schulz & Cannon, 2007). The MCR is a failed rift that developed in the late Mesoproterozoic (1120-1097 Ma; Malone et al., 2016) on the Laurentian supercontinent and overlaps the Greenville Orogeny (Cannon, 1994; Ojakangas & Dickas, 2002). The MCR extends from the Upper Peninsula, Michigan through Wisconsin, Iowa, and Kansas. The MCR is synonymous with the formation of the Lake Superior basin, the eruption of flood basalts including the Portage Lake Volcanics (Cannon, 1994), and several economic mineral deposits in the Upper Peninsula (Bornhorst & Barron, 2011). The mineral deposits driven by the Greenville orogeny, 40-50 Ma post rifting, are primarily strata-hosted (Bornhorst & Barron, 2011). The Keweenaw native copper deposits formed from circulating hydrothermal fluids derived from the Portage Lake Volcanic rocks (Bornhorst & Barron, 2011). Sedimentary rocks,

including the Bessemer Sandstone and Jacobsville Sandstone represent a transition from flood basalts, erupted during the Greenville Orogeny, to post rift sediments deposited in a subsiding basin during the Late Proterozoic (Stein et al., 2014, 2015; Malone et al., 2016). In the Pleistocene, glaciers eroded Michigan's landscape and carved out the great lakes, exposed bedrock, and deposited glacial till.

Gogebic Drillcore

We examined and sampled four drillcores, D9-08-20, D9-08-22, D9-08-23, and D9-08-24, that intersected the nonconformity from Gogebic County, Michigan (Fig. 22a, 22b) (Table 4, 5). The drill core were part of 20 drill cores acquired during an unconformity-type uranium exploration project in the western Upper Peninsula of Michigan housed by the Michigan DNR in Marquette, Michigan. The Gogebic area was targeted because of the presence of graphitic slate conductors and red bed sequences (Lynott, 2008) similar to what is present in the Athabasca Basin.

The Michigan cores consist of Precambrian Neoproterozoic Jacobsville Sandstone and Bessemer Sandstone atop of the Early Proterozoic Michigamme Slate (Lynott, 2008). The Michigamme Formation is the uppermost formation of the Marquette Range Super Group that consists of sedimentary rocks metamorphosed during the Penokean orogeny (Barovich et al., 1989). The Michigamme Formation consists primarily of alternating greywacke and slate. The Bessemer Formation is the basal unit and Jacobsville the uppermost unit of the Proterozoic Keweenawan Super Group (Morey & Van Schmus, 1988; Cannon & Nicholson, 1992; Zartman et al., 1997). In the drillcores, the Jacobsville Formation rests unconformably atop the Bessemer Formation, where present, or the

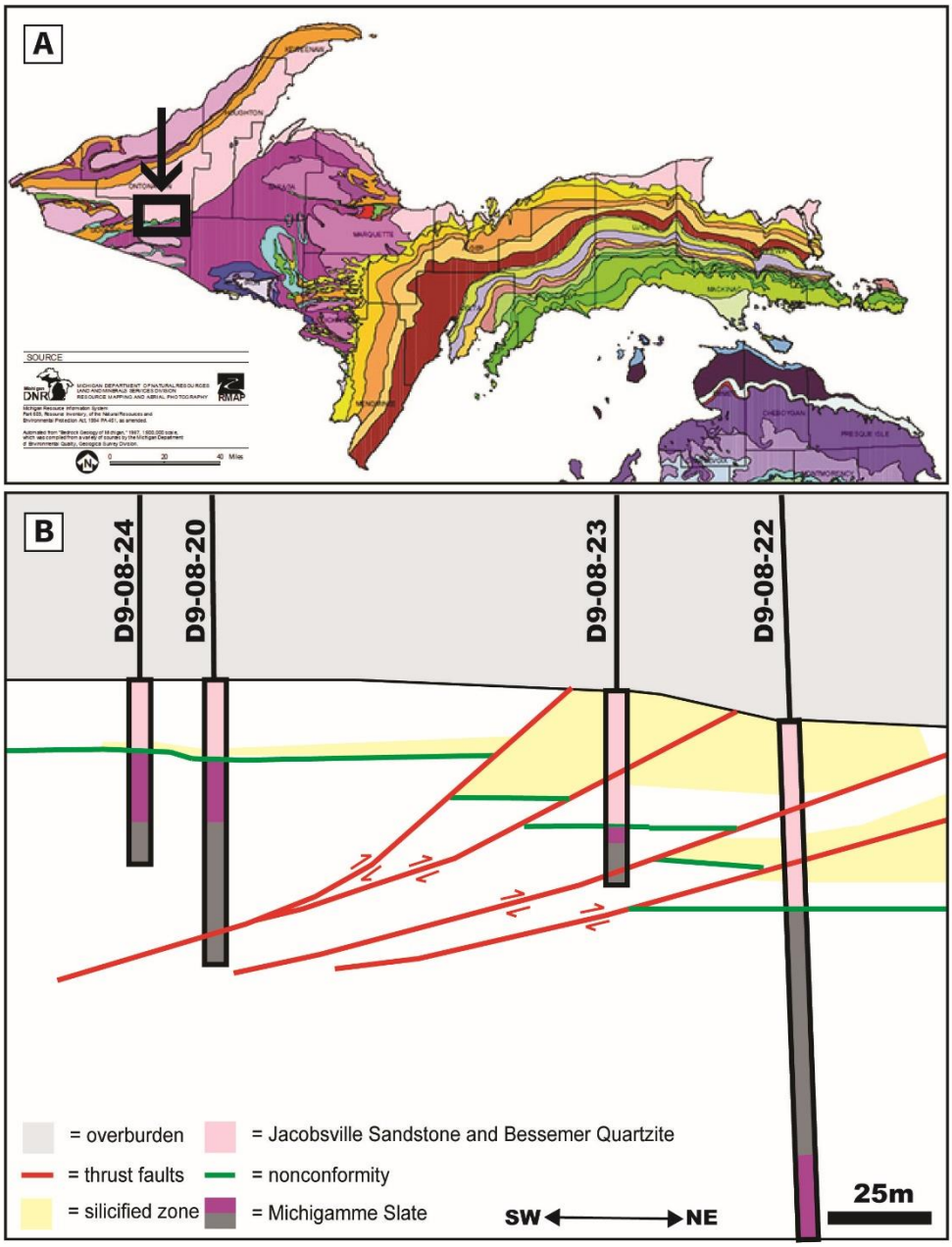

Figure 22. Geologic Map of the Upper Peninsula of Michigan and geologic cross section of Michigan site. **(A)** Locator map for Gogebic County in the Upper Peninsula of Michigan. Scale bar represents 40 miles. **(B)** Geologic cross section of Michigan site (After Lynott, 2008). Note the nonconformity is offset by several small displacement thrust faults. Gray: graphitic slate; Purple: non-graphitic slate.

Table 4 Summary of mineralogical analyses from Michigan core D9-08-20. Depth to nonconformity is 64.54 m. Depth to contact between non- graphitic slate and graphitic slate is 81.5 m. Note XRD minerals are in order from highest to lowest score as determined using the HighScore software. Ank: ankerite; Cal: calcite; Cb: carbonate; Chl: chlorite; Clc: clinochlore; Dol: dolomite; Fe: iron; Gr: graphite; Hem: hematite; Ill: illite; Kao: kaolinite; Micas: mica group; Ms: muscovite; Phl: phlogopite; Qtz: quartz; Srp: serpentine group; Vrm: vermiculite. TS: thin section. XRF - *: peak intensity above average ^: top 15 percentile peak intensity.

Sample	Depth (m)	Description	Subsample Description	XRD	Portable XRF
D9-08-20 A	66.19	Slate and metaphylitte, red-purple to gray, clay-rich, foliation and laycring at approximately 60° to core axis. Core length is 6.5 cm. Cb veins (6), widths ≤ 0.5 mm, parallel to layering and/or cleavage (TS A). Fracture surfaces have pale green hue, and contain very fine-grained metallic minerals (Possibly Py). Fractures planes retain moisture and stay damp longer after core is wetted. Breaks easily during cutting along fracture and compositional layers. Coarser grained than sample D.	A1 - slate / groundmass A2 - white vein / fault surface A3 - red to marron fault surface	Qtz, Ms, Gr, Clc, Ill, ± Phl. Guidottite (Srp)	Si*, K*, Ca, Ti*, Cr*, Mn, Fe, Ni*, Cu*, Zn*^, Rb, Sr*, Y*, Zr* Si, K, Ca*^, Ti, Mn*, Fe, Ni*^, Rb, Sr, Y*, Zr* Si, K, Ca, Ti, Mn, Fe*, Cu, Zn*, Rb*, Sr, Zr
D9-08-20 B	66.65	Slate, red to maroon-purple, wavy layering. Fault surface with clay gouge and Cb mineralization (TS BB). Microcrystalline Qtz-rich zone (cloudy-white) and purple slate bisected by white Cb veins (TS BA). Branching and anastomosing Cb veins (7-10) with widths ≤ 1 mm.	B1 - clay gouge / fault surface (top) B2 - Qtz / silicification zone B3 - dark gouge (bottom) B4 - red fracture surface Cb vein B5 - groundmass red slate B6 - groundmass Qtz-rich zone	Qtz, Clc, Fe, Cb (Ank, Cal), Hem, Ill Qtz, Fe, Clc, Ill, Hem, Ms, Cb (Cal, Ank), Gr Qtz, Gr, Ms, Cb (Ank, Cal), Clc, Ill, Halloysite	Si, K*, Ca, Ti*^, Cr, Mn, Fe*^, Zn*^, Rb*, Sr, Zr Si*^, K, Ca, Ti, Mn, Fe, Ni*^, Cu*^, Zn, Rb, Sr Si, K, Ca, Ti, Cr, Mn, Fe*, Rb*^, Sr Si, K*, Ca, Ti*, Mn, Fe*, Cu*, Zn*, Rb*, Sr, Y*, Zr* Si*, K*, Ti*, Cr, Mn, Fe*, Cu*, Zn*, Rb*, Sr, Y, Zr* Si, K, Ti, Cr, Mn, Fe*^, Zn*, Rb*^, Sr, Zr
D9-08-20 C	66.93	Slate and lesser chert / graywacke, red to black. Qtz- and Hem-rich, hard to cut. Highly indurated shear zone (TS CA1). Black gouge shear zone at top (TS CB2). Abundant coarse-grained red cubic Hem grains. Crosscut by iron oxide and carbonate veins.	C1 - White zone with white vein C2 - gouge near Black and veins C3 - groundmass white and red C4 - groundmass away from Qtz	Qtz, Hem, Fe, Clc, Gr, Ms, Cb (Cal, Dol) Qtz, Clc, Gr, Hem, Ill, Cb (Dol), Phl	Si*^, K, Ca, Ti, Cr, Mn, Fe*, Ni, Cu*, Rb, Sr, Y* Si*^, K, Ca, Ti, Cr*, Mn, Fe*, Ni, Cu*, Zn*, Rb, Sr, Y Si*, K, Ca, Ti, Mn, Fe*, Cu*, Rb*, Sr Si, K, Ti, Mn, Fe*^, Zn*, Rb*^, Sr, Zr
D9-08-20 D	67.48	Slate, Red to purple, wavy layering. Interconnected Cb veins parallel to subparallel to layering (TS D). Approximately 5 Cb veins, width 1 to 2.5 mm and many smaller subsidiary veins branching of vein margins. Multiple slickenslided faults surfaces, with white and green clays. Vein with symmetrical alternating white and pink Cb bands bounded on both sides by smoothed slip surfaces.	D1 - fault surface w/ veins, (white) (purple) D2 - fault surface w/ veins (white) (purple) D3 - slate minor veins D4 - green mineral fault surface and vein	Qtz, Cb (Cal, Dol), Ms, Clc Qtz, Gr, Cb (Cal), Clc, Ill, Ms, + Cronstedtite (Srp) Qtz, Chl-Srp, Hem, Ill	Si, Ca*^, Cr*, Mn*, Fe, Ni*^, Rb, Sr*, Y*, Zr Si, K*, Ca*, Ti, Cr, Mn*, Fe, Ni*, Cu*^, Zn*, Rb, Sr*, Y, Zr* Si, K*, Ti, Cr*, Mn, Fe*, Cu, Zn*, Rb*, Sr, Zr Si, Ca*^, Mn*, Fe, Ni*^, Rb, Sr*, Y*, Zr Si, K, Ca, Ti, Cr, Mn*, Fe*, Zn*, Rb*, Sr*, Y, Zr Si, K*, Ca*, Ti, Cr, Mn*, Fe, Ni*, Cu*, Rb, Sr*, Y*, Zr
D9-08-20 E	74.12	Slate, red to purple, small patches of green to white clays and/or green reduction spots parallel to layering (60°) (TS E). No Cb Veins. Breaks easily along layers and/or cleavage planes. Ms-rich.	E1 - slate with white patches E2 - red fracture surface	Qtz, Ms, Gr, Ill	Si*^, K*, Ca, Ti*^, Cr*, Fe*, Ni, Cu*, Rb, Sr*, Y*, Zr* Si*, K*^, Ti, Cr*^, Fe*, Cu, Zn*, Rb*, Sr*, Y, Zr*
D9-08-20 F	76.58	Slate to schist, Pale purple/red to gray, wavy layering. Broken zone, fault and fracture with clay-rich gouge, fragile, heavily fractured. Pale green to white clays. Ms-rich.	F1 - clay gouge minor slate/schist (purple) (Green clay)	Qtz, Ms, Gr, Ill	Si*, K*^, Ti*^, Cr*^, Fe*, Cu, Rb*, Sr*, Y*^, Zr* Si*, K*^, Ti*^, Cr*^, Mn, Fe, Ni*^, Cu*, Rb, Sr*^, Y*^, Zr*^
D9-08-20 G	78.96	Slate, earthy red to brown, wavy and folded layering (TS G). Leached zone, patchy alteration, and dissolution voids. Rock heavily dissolved and decomposed. Above fault gouge zone at 79.68 m. Coarse grained carbonate.	G1 - dissolution void G2 - clay, black fracture surface minor vein G3 - slate and veins	Qtz, Fe, Cb (Ank, Cal), Ill, Clc, Gr Qtz, Fe, Ill, Ms, Hem, Cb (Cal, Dol), Clc Qtz, Fe, Ill, Hem, Ms	Si, K, Ca*, Ti, Cr, Mn*, Fe*, Rb, Sr, Y, Zr Si*, K*^, Ti*^, Cr*, Fe, Ni, Cu*, Rb, Sr*, Y*^, Zr*^ Si*^, K, Ca, Ti, Cr*, Fe*, Ni, Cu*, Rb, Sr, Y, Zr
D9-08-20 H	81.28	Slate, dark purple/red to brown, wavy layering. Abundant white Cb veins generally parallel to subparallel to layering (TS H1). Clay gouge zones and slip surfaces, same orientation as veins. Pale green to grey clay-rich fault surfaces. Veins also occur sub-perpendicular to core axis.	H1 - green clay fault surface w/ slate H2 - (TS H2) black fracture with green clay minor veins H3 - slate maroon and veins	Qtz, Gr, Ms, Ill, Cb (Ank), Clc Qtz, Gr, Ms, Cb (Dol), Clc, Al? Cr? Qtz, Cb (Ank), Ms, Clc, Clinopyroxene	Si*, K*^, Ca, Ti*^, Cr*^, Mn, Fe, Ni*, Zn*, Rb, Sr*, Y*^, Zr*^ Si, K, Ca, Ti, Cr, Mn, Fe*^, Zn*, Rb*, Sr Si, K, Ca, Ti, Cr, Mn, Fe*^, Cu*, Rb*^, Sr, Zr Si*, K, Ca*, Ti, Cr, Mn*, Fe, Ni*, Cu, Rb, Sr*, Y*, Zr
D9-08-20 I	81.36	Slate, dark maroon, high density of anastomosing Cb veins in a shear fabric (TS I). Highly fractured and deformed clay-rich domain. Dark green to purple clays. Very fragile.	I1 - middle (clay clumped during powdering)	Vrm, Tosudite, Cb (Dol), Hem	
D9-08-20 J	81.4	Transition zone. Contact between non-graphitic and graphitic slate. Abundant highly anastomosing Cb veins (TS J). Vein aperture increases from top to bottom (From 0.5 to 2.5 mm). Green clay at transition zone. Veining dissipates in graphite zone ending at 82 m.	J1 - non-graphitic slate J2 - graphitic slate w/ clay, green tint, minor veins J3 -graphitic slate	Cb (Dol), Gr, Kao, Vrm, Ms Gr, Cb (Ank), Clc, Ill, Mnt-Chl, Nontronite	Si, K, Ca*, Ti, Cr, Mn*, Fe, Ni, Rb, Sr Si, K*, Ca, Ti*^, Cr*^, Mn, Fe, Ni, Cu, Zn*^, Rb*, Sr*^, Y*^, Zr*^ Si, K, Ca, Ti*, Cr, Mn, Fe*, Zn*, Rb*, Sr*, Zr

Table 5 Summary of mineralogical analyses from Michigan core D9-08-24. Depth to nonconformity is 60.17 m. Depth to contact between non- graphitic slate and graphitic slate is 78.66 m. Note XRD minerals are in order from highest to lowest score as determined using the HighScore software. Ank: ankerite; Cal: calcite; Cb: carbonate; Chl: chlorite; Clc: clinochlore; Dck: dickite; Dol: dolomite; Fe: iron; Goe: Goethite; Gr: graphite; Hem: hematite; Ill: illite; Kao: kaolinite; Micas: mica group; Ms: muscovite; Phl: phlogopite; Py: pyrite; Qtz: quartz; Srp: serpentine group; Vrm: vermiculite. *: peak intensity above average; ^: top 15 percentile peak intensity.

Sample	Depth (m)	Description	Subsample Description	XRD	Portable XRF
D9-08-24 A	66.33	Slate, red to grey, wavy layering. Broken zone, fault / fracture zone, clay-rich gouge / fracture surfaces, fragile, heavily fractured. Yellow to brown patchy hydrothermal alteration and green to grey/blue clays.	A1 - gouge /clays	Qtz, Gr, Ill, Ms, FPhl, Clc	Si*, K*^, Ti*^, Cr, Mn, Fe*, Ni, Cu, Rb*, Sr*^, Y, Zr*^
			A2 - yellow alteration	Qtz, Ms, Fe, Ill, Py, Hem	
			A3 - red to brown to yellow	Qtz, Ms, Gr, Ill, Hem	Si, S*, K*^, Ti*^, Cr*^, Fe, Ni*, Cu, Zn*^, Rb*, Sr*^, Y*^, Zr*^
D9-08-24 B	72.28	Slate, red to maroon / purple, wavy layering. Fracture zone, clay rich fracture surfaces. Top half red to maroon with patchy alteration. Lower half pale red, and more altered with abundant dissolution voids, forms sharp contact. Some voids filled with calcite. Leached interval.	B1 - clay fracture surface	Qtz, Ms, Gr, Ill, Ms	Si*, K*^, Ti*^, Cr*^, Fe, Ni*^, Cu*^, As* / Pb*^,Rb, Sr*^, Y*^, Zr*^
			B2 - slate protolith	Qtz, Ms, Gr, Ill, FPhl, Ms	Si*^, K*, Ti*, Cr, Fe*, Ni, Cu*^, Rb, Sr, Y*^, Zr*^
			B3 - altered slate	Qtz, Ms, Gr, Hem, Ill	Si*^, K*, Ti, Cr, Fe, Ni*^, Cu*^, As* / Pb*^,Rb, Sr*^, Y*^, Zr*^
			green fault surface / clays		
D9-08-24 C	74.92	Slate to schist, earthy dark red to brown, wavy layering, altered. Leached interval. Top and bottom fracture with green to blue / yellow clay. Rock heavily dissolved and decomposed, appears to be concentrated along fractures. Abundant dissolution voids some filled with calcite. (above fault gouge at 75.64m)	C1 - red fracture surface	Qtz, Ill, Ms	Si, K*^, Ti*, Cr*^, Fe*, Ni, Cu, Rb*, Sr*, Zr*
			C2 - calcite and clay	Qtz, Ms, Gr, Cb (Cal), Ill, Goe	Si, K*, Ca, Ti*, Cr*, Fe*, Ni, Cu*^, Rb, Sr*, Y*, Zr
			C3 - groundmass		Si*, K*^, Ti*^, Cr*, Fe*, Ni, Cu, Rb*, Sr, Y*, Zr*
D9-08-24 D	77.40	Slate, red to brown, wavy layering. Abundant veins generally parallel to subparallel to layering. Veins chaotic near base, and parallel to subparallel to layering at top.	D1 - slickenfibres fault surface	Qtz, Cb (Cal), Glc, Gr, Ill, Clc	Si, K*, Ca, Ti*, Cr, Mn, Fe*, Ni, Rb, Sr*, Y*, Zr*,
			D2 -white veins w/ minor slate	Cb (Cal), Fe, Gr, Qtz, Ill	Si, K, Ca*^, Ti*, Cr*, Mn, Fe, Ni*^, Rb, Sr*, Y*, Zr*
			D3 - slate w/ veins		Si*, K, Ca*^, Ti, Cr, Mn, Fe, Ni*^, Cu*^, As* / Pb*^,Rb, Sr, Y, Zr
			D4 - slate		Si*, K, Ca, Ti, Cr, Fe*, Ni*, Cu, Rb, Sr*, Y*, Zr*,
D9-08-24 F	78.31	Slate, red to purple, highly altered and deformed . Pervasive calcite mineralization in chaotic and anastomosing white veins. Original rock textures highly folded and contorted. Brecciated texture. Carbonate veins crosscut by vein with black infill, possibly Chl.	F1 - dark slate		Si, K, Ca, Ti, Cr, Mn, Fe*, Ni, Cu, Rb*, Sr, Y, Zr
			F2 - white veins		Si, Ca*, Ti, Cr, Mn, Fe*, Zn*^, Rb*, Sr
			F3 - slate		Si*^, K, Ca*, Ti, Cr*^, Fe, Ni*^, Cu*^, As* / Pb*^,Rb, Sr, Y, Zr
			F4 - veins and slate		Si, Ca*^, Ti, Mn, Fe, Ni*, Rb, Sr, Y, Rh
D9-08-24 G	78.35	Slate, dark red to purple, wavy layering. Continuation of texture observed in sample F. Calcite mineralization in branching chaotic veins. Preferred orientation parallel to compositional layers.	G1 - slate		Si, K, Ca, Ti, Cr*, Mn, Fe*^, Rb*, Sr,
			G2 - white veins		Si, Ca*^, Mn*^, Fe, Ni*, Rb, Sr, Y
D9-08-24 H	78.49	Transition from red non-graphitic to back graphitic slate. Abundant Cb veins with brecciated, anastomosing, and branching textures. Brecciated sections.	H1 - graphitic slate		Si, K, Ca*, Ti, Cr, Mn*, Fe*, Ni, Zn*^, Rb, Sr, Y, Zr
			H2 - transition		Si, K, Ca*, Ti, Mn*, Fe*, Cu, Zn*, Rb, Sr
			H3 - veins and groundmass		Si, K, Ca*, Ti, Mn*^, Fe*, Cu, Rb, Sr
			H4 - green clay		Si, Ca*^, Cr*, Mn*^, Fe, Ni*, Cu, As* / Pb*^, Sr
			H5 - white vein		Si, Ca*^, Mn*, Fe, Ni*, Sr
			H6 - dark groundmass		Si, K, Ca, Ti, Cr, Mn, Fe*^, Rb*, Sr, Zr
D9-08-24 E	78.88	Graphitic slate, black, wavy layering / folding. Dominantly black with minor alteration to green clays. Very small patches of red to brown hematite. Fine grained disseminated pyrite. End of sample with slight white to green tint, with clay alteration.	E1 - graphitic slate	Qtz, Gr, Ms, Vrm, Ill, Clc	Si*^, K, Ca, Ti, Cr*^, Mn, Fe*, Ni, Cu*^, Rb, Sr, Y, Zr
			E2 - white / green tint clay	Qtz, Gr, Dck, Vrm, Ill	Si*, K*, Ca, Ti*, Cr*, Mn, Fe, Ni*, Cu, Rb*, Sr*^, Y*^, Zr*^
D9-08-24 I	82.17	Graphitic slate, black, folded, wavy layering. Blocky and subhedral disseminated pyrite. Highly polished graphitic fault surfaces.	I1 - pyrite zone	Py, Qtz, Gr, Chl-Srp, Ill, Mag, Clc	Si, S*, K, Ca, Ti, Cr*, Fe*^, Cu*^, Zn*^, Rb*^, Sr
			I2 - graphite polished fault surface		Si, K*^, Ca, Ti*^, Cr*, Fe*, Ni, Zn*^, Rb*, Sr*^, Y*^, Zr*^
			I3 - graphitic groundmass		Si, K*^, Ti*^, Cr*^, Mn, Fe*, Ni, Zn*, Rb*, Sr*^, Y*, Zr*^
			I4 - silicification w/ pyrite		Si*^, S*^, K*, Ti, Cr*, Fe, Ni*^, Cu*^, Rb, Sr, Y, Zr

Michigamme Formation. The Jacobsville Formation consists of fluvial quartzose and feldspathic sandstones deposited in rift basins (Bornhorst & Barron, 2011; Mitchell & Sheldon, 2016), and zircon ages show that the Jacobsville Sandstone is Neoproterozoic (Craddock et al., 2013; Malone et al., 2016). Unconsolidated glacial deposits overlay these units. Volcanic and sedimentary rocks of the Powder Mill Group, Bergland Group, and Oronto Group that underlie the Jacobsville Sandstone are missing in the core, however, are present further north.

The cores intersect several small displacement thrust faults in the hanging wall of larger thrust (Fig. 22b), with approximately 40 m of throw of the nonconformity between boreholes D9-08-20 and D9-08-22 (Lynott, 2008). The sedimentary and basement rocks display variable degrees of alteration (Table 4, 5), with preferential alteration possibly occurring along thrust faults and thickened basal sandstone units (Lynott, 2008). The nonconformity zone contains elevated concentrations of pathfinder elements, suggesting mineralizing fluids circulated proximal to the interface (Lynott, 2008). The Jacobsville and Bessemer Sandstones are red, medium- to coarse-grained, and well sorted with lesser interbeds of mudstone and shale (Lynott, 2008). The sandstones are jointed, bleached, and silicified (Table 4, 5). The basal unit is a silicified conglomerate and contains carbonate, sulfide, iron oxide, and minor copper mineralization (Lynott, 2008). The crystalline basement consists of oxidized non-graphitic slate and graphitic slate of the Michigamme Formation. The contact between non-graphitic slate and graphitic slate includes a 1.0 to 2.0 m zone of sub-horizontal carbonate veining and marks the appearance of euhedral to subhedral pyrite grains (Table 4, 5). Locally the graphite-rich slate has fault surfaces with purple smear, which may indicate shear along the contact

(Lynott, 2008). The non-graphitic and graphitic slate contact intersects the nonconformity near drill hole D9-08-22, and the sandstone and slates straddling the nonconformity are mineralized (Lynott, 2008). These core provide examples and insights into a highly altered sequence of rocks at a nonconformity.

Drillcore Descriptions

Michigamme slates are intermittently cut by faults, clay gouges, bleached zones, leeched zones with abundant voids, pressure solution seams, folded and contorted layers, clay-rich shear zones, and broken core intervals (Table 4, 5) (Fig. 23 A-J). Iron oxide, primarily hematite, gives the rocks a characteristic deep red color. Leached zones occur adjacent to faults and consist of a siliceous boxwork of dissolution voids and vugs with patchy quartz, carbonate, and chlorite mineralization (Fig. 23 G1). The slates are prone to fracture along fractures, cleavage planes, and compositional layers. Clay-rich shear fractures and carbonate veins are abundant within the basement slates. Veins occur both as singular veins that are parallel or subparallel to cleavage and/or compositional layering (Fig. 23 A1), and as densely clustered intervals of branching and/or highly anastomosing vein networks (Fig. 23 BB1, BA1, CA1, D, H11, H21, I1, J1). Singular veins are typically fibrous and are locally bound by shear fractures with stepped and slickensided surfaces. Additionally, veins display anastomosing, brecciated, and mesh textures that are primarily composed of blocky carbonate grains (Table 4, 5). Brecciated intervals consist of angular fragments of phyllosilicate-rich graphitic and non-graphitic slate suspended in a network of white, chaotic, and branching carbonate veins (Table 4, 5).

The non-graphitic slate transitions to a dark gray to black graphitic slate (Fig. 23


A1

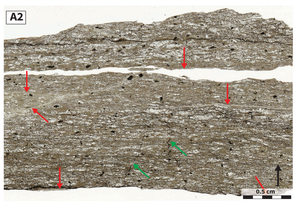
A2
0.5 cm

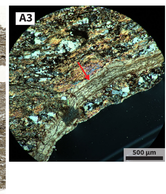
A3
500 µm

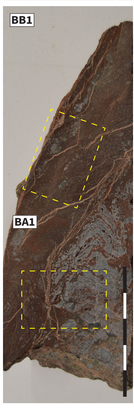
BB1
BA1

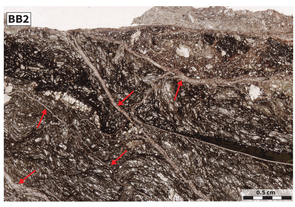
BB2
0.5 cm

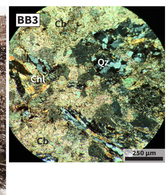
BB3
Chl
Qz
Chl
Cb
250 µm

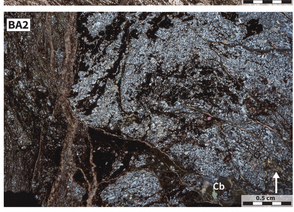
BA2
Cb
0.5 cm

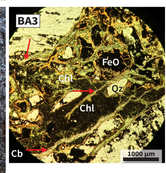
BA3
FeO
Chl
Qz
Chl
Cb
1000 µm


CA1
CB1

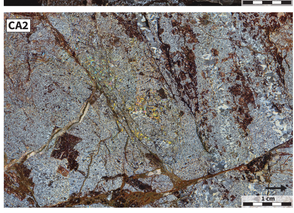
CA2
0.5 cm

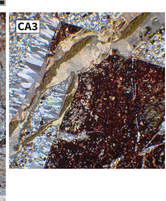
CA3

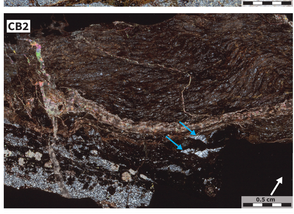
CB2
0.5 cm

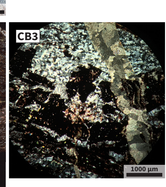
CB3
1000 µm


D1

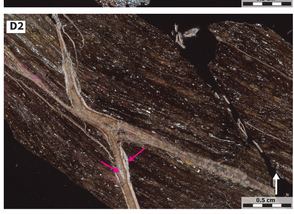
D2
0.5 cm

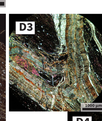
D3

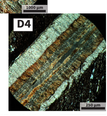
D4


E1

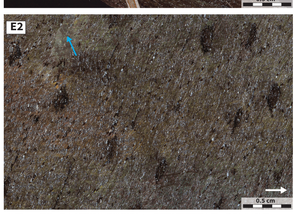
E2
0.5 cm

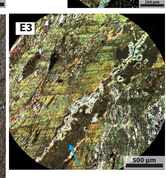
E3
500 µm


G1

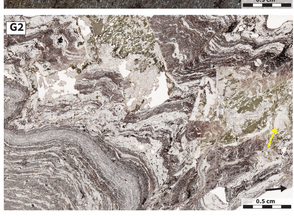
G2
0.5 cm

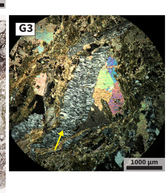
G3
1000 µm

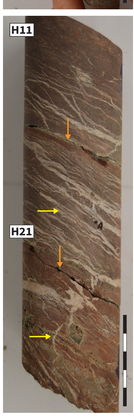
H11
H21

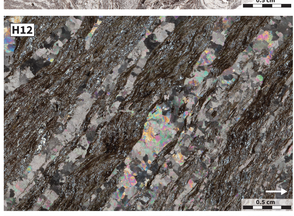
H12
0.5 cm

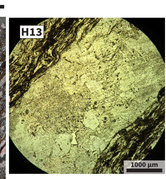
H13
1000 µm

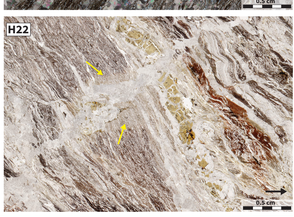
H22
0.5 cm

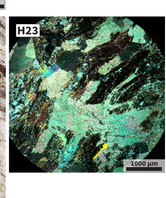
H23
1000 µm


I1

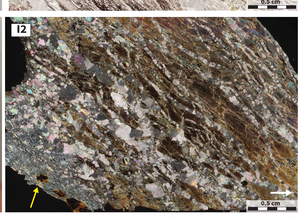
I2
0.5 cm

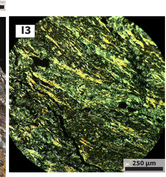
I3
250 µm


J1


J2
1 cm

Figure 23. Core photographs, thin section scans, and photomicrographs taken of core samples from core D9-08-20. Left: core photographs (ZZ1); Middle: thin section scans (ZZ2); Right: photomicrographs (ZZ3). Letters correspond to the sample label. Depth of samples increases from top to bottom (see Table 1 A, B). Scale bars on core photos represent 5 cm, and core photos are oriented relative to original core axis. Arrows on thin section scans mark upwards direction and long core axis.

D9-08-20A (A1) Relatively undeformed slate with thin layer and cleavage parallel carbonate veins with irregular fine-grained phyllosilicate margins (width ≤ 0.5 mm). (A2) Carbonate veins (red arrows) and opaque pressure solution seams (green arrows) crosscut subhorizontal oriented cleavage. Dark black cleavage lamellae are primarily composed of iron oxide. (PPL). (A3) Magnified view of fine-grained quartz- and phyllosilicate-rich domains and crosscutting carbonate vein at the base of thin section. Vein is crosscut by secondary anastomosing fractures or cleavage lamellae. Note variable extinction of carbonate grains. (XPL).

D9-08-20BB (BB1) Shear zone in slate (top). Yellow box marks border of thin section. (BB2) Clay- and carbonate-rich shear zone (top), and deflected carbonate veins. Previous quartz-rich layers are contorted, folded, and broken up. (BB3) Magnified view of shear fracture/zone infilled with a mixture of quartz, chlorite, and carbonate. (XPL).

D9-08-20BA (BA1) Microcrystalline cloudy-white quartz zone and red slate bisected by branching carbonate veins. Yellow box marks border of thin section. (BA2) Slate (left), microcrystalline quartz (right), and cubic iron oxide crosscut by chlorite, smectite, and calcite veins. Veins contain abundant inclusions of wall rock, and voids infilled with coarse-grained carbonate (lower right). (XPL). (BA3) Magnified view displaying crosscutting relationships. Veins with pale green chlorite and yellow fine-grained clay and/or iron oxyhydroxides. Veins contain inclusions of quartz and iron oxide and are crosscut by carbonate veins (red arrows). (PPL).

D9-08-20CA (CA1) Quartz-rich interval with shear fractures and branching calcite veins. (CA2) Microcrystalline quartz and blocky quartz veins or bands crosscut by shear fractures and dilatational jog structures with carbonate, chlorite, and iron oxyhydroxide infill. (XPL). (CA3) Magnified view of relict pyrite grain replaced by hematite with face-controlled quartz strain fringes, crosscut by chlorite, carbonate, and quartz veins. Note the edge of the grain is separated. (XPL).

D9-08-20CB (CB1) Quartz-and iron oxide-rich shear zone at bottom of core. (CB2) Large opaque grains with quartz strain fringes (blue arrow). Iron oxide and quartz grains crosscut by carbonate veins. (XPL). (CB3) Magnified view of blocky carbonate vein with inclusions crosscutting iron oxide. (XPL).

D9-08-20D (D1) Slate with layer parallel carbonate veins, and subvertical connecters. (D2) Polytextured fibrous and blocky carbonate veins. Intersection of veins is sigmodal shaped. Compositional layering runs NW-SE. Note fibrous veins cracked and separated a phyllosilicate-rich aggregate. (XPL). (D3) Magnified view at vein branch. Vein contains inclusions of wall rock and augen shaped aggregates of fine-grained phyllosilicates. (XPL). (D4) Magnified view of fibrous carbonate vein displaying roughly symmetrical habit. Fibers at vein margin are perpendicular to fracture margin.

D9-08-20E (E1) Purple slate with pale green reduction and/or alteration spots. (E2) Chlorite- and muscovite- rich slate with beard like opaque mineral growths, and patch clay alteration (blue arrow). (XPL). (E3) Magnified view of alteration to fine-grained illite and chlorite. Groundmass consists of chlorite and muscovite. (XPL).

D9-08-20G (G1) Leached interval with siliceous boxwork of dissolution voids. (G2) Folded and contorted quartz-rich layers. Large dissolution voids and vugs infilled with patchy quartz, calcite, and chlorite mineralization. (PPL). (G3) Magnified view of asymmetric antiaxial fibrous quartz vein with well-defined median plane. Quartz vein is bounded by coarse-grained carbonate infill (XPL).

D9-08-20H1 (H11) Slate with interconnected carbonate vein network. Slate is crosscut by chlorite-rich shear zones (orange arrows). Thin sections are from middle and bottom interval (yellow arrows). (H12) Blocky carbonate veins anastomosing subparallel to cleavage. Deformed iron oxide grains in clay-rich shear zone in the upper left (not pictured). (XPL). (H13) Magnified view of blocky carbonate vein. (PPL).

D9-08-20H2 (H21) Carbonate veins crosscutting chlorite-rich slate. Possibly chlorite rich shear zone. (H22) Layer parallel carbonate and chlorite veins crosscut by subperpendicular blocky carbonate vein. Note Alteration of wall rock adjacent to carbonate vein. Carbonate grains display slight undulatory extinction. (PPL). (H23) Magnified view of blocky carbonate grain. Note rhombohedral shaped dolomite grain (red arrow). (XPL).

D9-08-20I (I1) Chlorite- and phyllosilicate-rich shear zone with shear fabric and abundant carbonate veins. (I2) Clay-rich shear fracture with deformed opaque minerals (yellow arrow). (XPL). (I3) Magnified view of chlorite-rich shear zone with a feathery texture. (XPL).

D9-08-20J (J1) Transition zone from graphitic to non-graphitic slate. Slate and phyllosilicate aggregates surrounded by white carbonate. Groundmass color transitions from red to black. Interpreted as a shear zone with a network of highly interconnected and anastomosing carbonate veins. Note vein aperture increases with depth. (J2) Blocky carbonate veins and cement with abundant inclusions of wall rock. Veins also include sections composed of feathery chlorite and/or smectite (XPL).

J1). A 1.0 to 2.0 m zone of pervasive mineralization and a dense network of highly anastomosing carbonate veins (Fig. 23 H11, H21, I1, and J1) characterize the transition zone. Vein width it varies from 0.1 to 3.0 cm, and veins contain numerous inclusions of wall rock. The transition zone exhibits shear fabrics and contains a high percentage of carbonate minerals. Locally a breccia vein network cuts a highly anastomosing vein network. The slates grade from red-purple to red-purple-gray-green to dark gray-black (Table 4, 5). The carbonate veins dissipate as graphite content increases. The dark-gray to black graphitic slate has wavy layering and disseminated pyrite and iron oxide. Shear fractures in the graphitic slate exhibit highly polished and stepped graphite coated slip surfaces. The non-graphitic slate to graphitic slate transition zone intersects the nonconformity near drill hole D9-08-22 where the green clay-rich graphitic slate is cut by a mesh-textured vein network and stylolites. Drill hole D9-08-22 is over 150 m from drill holes D9-08-20 and D9-08-24, indicating the mineralization was widespread along the contact. The rock-quality designation (RQD) of the non-graphitic slate is generally less than or equal to 50%, and the RQD of the graphitic-slate is generally higher than or equal to 50% (Lynott, 2008) (Fig. 24), indicating they may be discrete mechanical and lithological units.

Optical Petrography

The least-altered slates are very fine- to fine-grained and consist of anastomosing compositionally layered quartz-rich and phyllosilicate-rich domains, and dark brown iron oxide cleavage lamellae and pressure solution seams (Fig. 23 A2). Mineral assemblages

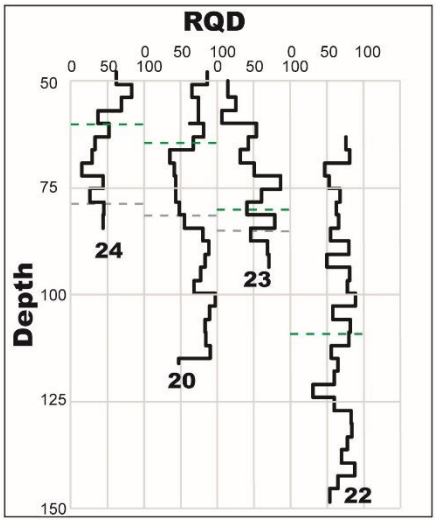

Figure 24. RQD versus depth for Michigan cores. Note that the RQD of graphitic slate is higher than the non-graphitic slate. Green dashed line: nonconformity; Gray dashed line: contact between non-graphitic slate and graphitic slate. Data from Lynott, 2008.

generally include a combination of quartz, muscovite, chlorite, and/or iron oxide (Table 4, 5). Thin carbonate veins, widths ≤ 0.5 mm, with fine-grained phyllosilicate margins cut parallel to subparallel to compositional layering and/or cleavage planes, with lesser veins occurring at moderate angles to layering connecting layer parallel veins (Fig. 23 A2). Locally pressure solution seams and/or secondary fractures overprint carbonate veins (Fig. 23 A3). Splitting and breakage during thin section preparation typically occurred along veins, pressure solution seams, cleavage planes, and compositional layers.

Carbonate veins occur adjacent to clay-rich gouge and fracture zones composed of chlorite, carbonate, and quartz (Fig. 23 BB2, BB3). Previous quartz-rich layers are broken up into quartz boudins. Locally shear fractures and branching veins cut a competent interval of alternating iron oxide-rich and microcrystalline quartz-rich rock (Fig. 23 BA2). Vein infill includes carbonate, chlorite, iron oxide-hydroxide, and quartz (Fig. 23 BA3). Quartz grains display undulatory extinction and sutured and bulging grain boundaries, and are overprinted by patches of feathery mica. Carbonate veins cut quartz, iron oxide-hydroxide, and chlorite veins. Dilatational jog structures and extensional fractures with carbonate infill are abundant (Fig. 23 CA2). Large hematite pseudomorphs after pyrite with mottled quartz-rich interiors are split by shear and dilatational fractures with quartz, chlorite, and carbonate infill (Fig. 23 CA3). Subhedral iron oxide grains commonly have face controlled fine-grained quartz strain fringes (Fig. 23 CA3, CB2, CB3). Iron oxide-rich samples typically have a weak magnetic attraction. Samples typically display slaty cleavage and S-C fabrics (Fig. 23 H12, H22). Carbonate veins display fibrous and blocky textures. Locally fibrous carbonate veins display a roughly symmetrical habit of alternating white and pale brown carbonate, and lesser chlorite and

quartz (Fig. 23 D2, D4). Carbonate grains towards the fracture median have a blocky texture and display slight undulose extinction. Towards the fracture margin, the carbonate is fibrous with fibers oriented perpendicular to the vein margin. The veins contain augen shaped ‘inclusions’ of aggregates of phyllosilicates, some that are split by carbonate veins (Fig. 23 D2, D3, D4). In hand sample, similar fibrous veins are bounded by slickensided surfaces. Carbonate veins and slickenfibres with variable composition implies multiple generations and a combination of crack-seal and slip mechanisms.

The preferred orientation of veins is parallel to subparallel to compositional layers and cleavage planes (Fig. 23). Locally pale green reduction and/or alteration spots, elongate parallel to cleavage planes, are composed of fine-grained clay minerals (Fig. 23 E2, E3). The anastomosing cleavage locally displays beard like growths and/or accumulations of iron oxide or graphite (Fig. 23 E2). Leached zones consist of large dissolution voids, occupying large relict porphyroblasts, infilled with patchy, mottled, and veined chlorite, carbonate, and quartz (Fig. 23 G2, G3). Cleavage is commonly subparallel to layering, however in sections layering and cleavage is folded and contorted (Fig. 23 G2). Vein density generally increases with depth up to the contact between non-graphitic slate and graphitic slate. The transition zone consists of a pervasive network of highly anastomosing carbonate veins with a preferred orientation parallel to subparallel to cleavage planes, with lesser veins occurring at moderate to high angles (Fig. 23 H12, H22, I2, J2). The veins display blocky texture and are composed of subhedral to euhedral coarse-grained calcite, and iron and magnesium carbonates with clear to turbid appearance (Fig. 23 H13, H23). Chemical and color variation may indicate multiple generations and/or growth stages. The blocky carbonate grains have abundant fluid

inclusions, and locally display tabular twin lamellae and slight undulatory extinction. The carbonate veins cut slate with iron oxide- and chlorite-rich bands, veins, and/or alteration patches and the wall rock adjacent to the veins is altered and discolored forming a halo around vein margins (Fig. 23 H22). Fine-grained chlorite-rich veins and secondary mineralization zones appear nearly black in hand sample, and in PPL, they are a translucent pale green (Fig. 23 H21, H22). The transition zone consists of a chlorite-rich shear zone (Fig. 23 I2, I3) with S-C fabrics, and lesser quartz grains. The vein network contains abundant inclusions of wall rock and splitting preferentially along phyllosilicate minerals and cleavage planes (Fig. 23 J2). Feathery patches of randomly oriented chlorite and/or smectite intermittently occur within the blocky carbonate vein cement.

X-ray Diffraction Results

Mineral assemblages in the slate generally consist of a combination of quartz, muscovite, chlorite, and/or iron oxide (Fig. 25a, 25b, 26) (Table 4, 5). Vein networks are composed of calcite and/or iron and magnesium carbonates that overprint chlorite, quartz, and iron oxide mineralization (Table 4, 5) (Fig. 23, 25, 26). Vein composition typically consists of a mixture of calcite and iron-magnesium carbonates with calcite-rich and ankerite- and/or dolomite-rich intervals (Table 4, 5). Calcite was distinguished by its strong reflections at approximately 3.05 Å (29.4 2θ), 2.29 Å (39.5 2θ), and 2.10 Å (43.2 2θ). Dolomite and ankerite were distinguished by their strong reflections at approximately 2.89 Å (30.9 2θ), 1.79 Å (51.1 2θ), and 2.19 Å (41.1 2θ). The iron and/or magnesium carbonate listed in Table 4, and Table 5 is the best match as determined using the High Score software. In sample D9-08-20 D calcite-rich veins where cut by iron and

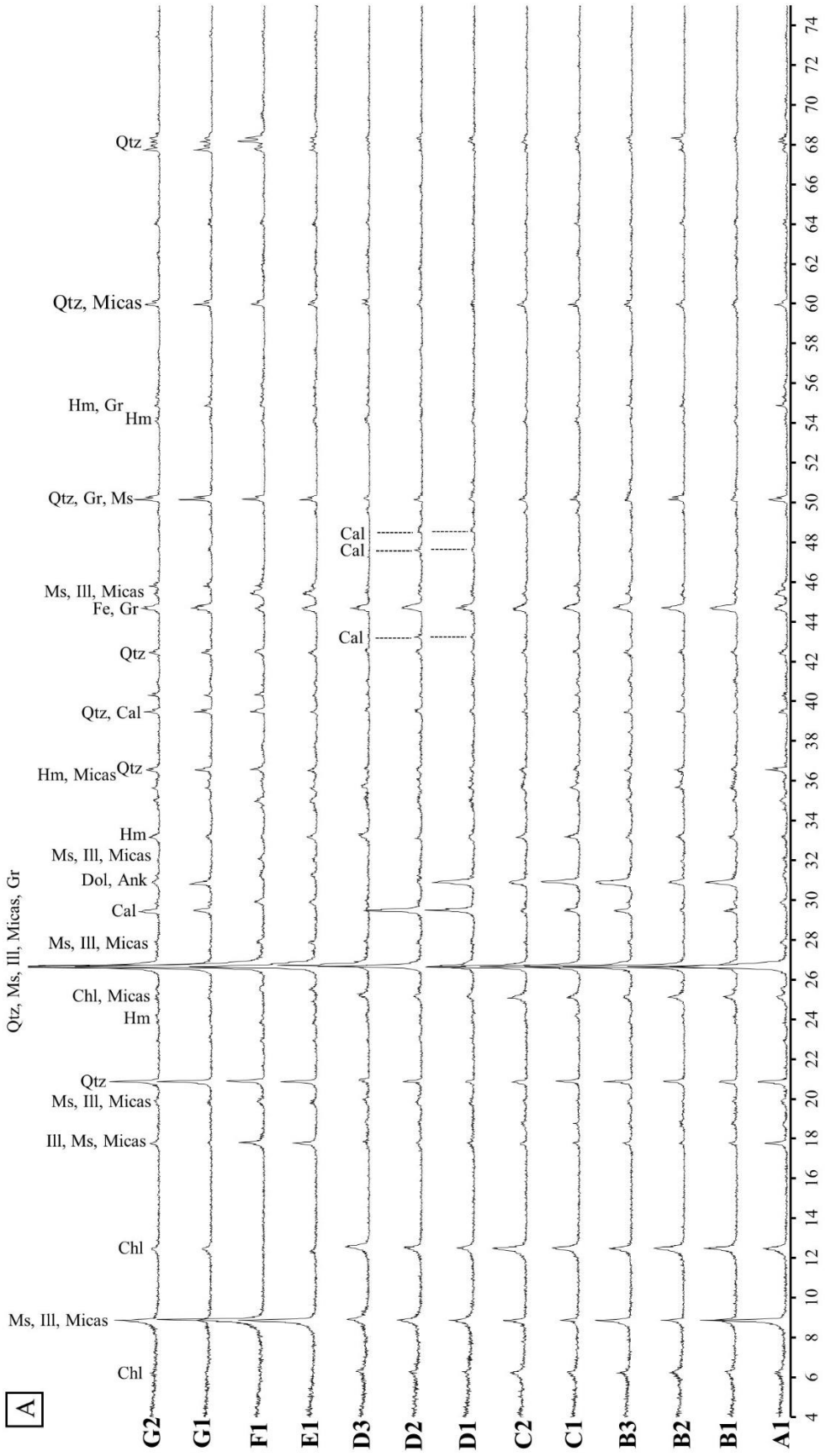

Figure 25. (A) continued next page.

B

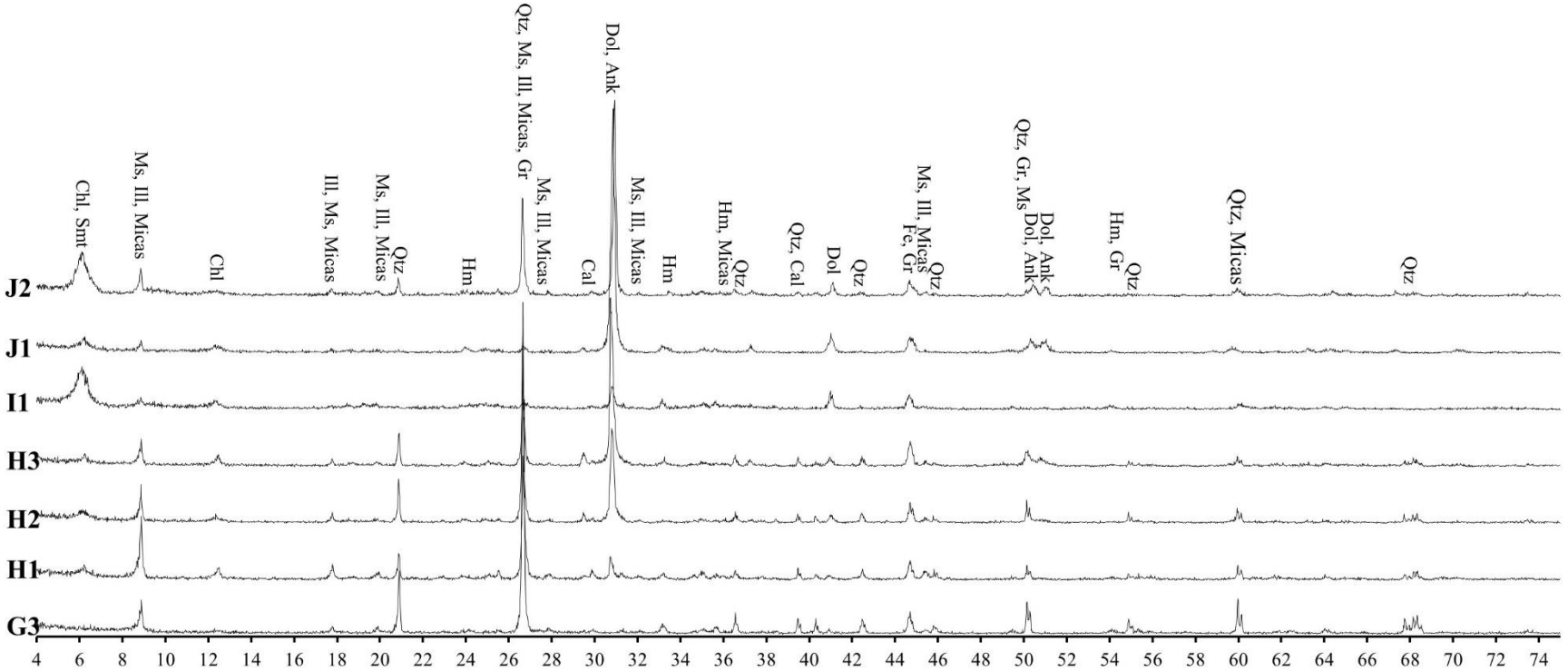

Figure 25 cont. XRD patterns of bulk powder samples from core D9-08-20 with mineral peak positions labeled.**(A)** Samples A1 through G2. **(B)** Sample G3 through J2. Intensity versus °2θ – Cu2α. Profiles have the same scale with a vertical offset of 200 counts between profiles. Note decrease in chlorite peak intensity and sharpness at 7.15 Å (12.35 2θ) with increasing depth. G note leached sample G1 with no chlorite reflection. A sharp increase in number of reflections attributed to ankerite and/or dolomite and decrease in number of reflections attributed to calcite occurs in samples within the transition zone (samples H1-J2). Note appearance of the broad high intensity reflection at 14.38 Å (6.15 2θ) in samples adjacent to the contact between graphitic slate and non-graphitic slate, and reduction of quartz peaks. Ank: ankerite; Cal: calcite; Chl: chlorite; Dol: dolomite; Fe: iron; Gr: graphite; Hm: hematite; Ill: illite; Micas: mica group; Ms: muscovite; Qtz: quartz. See Table 4.

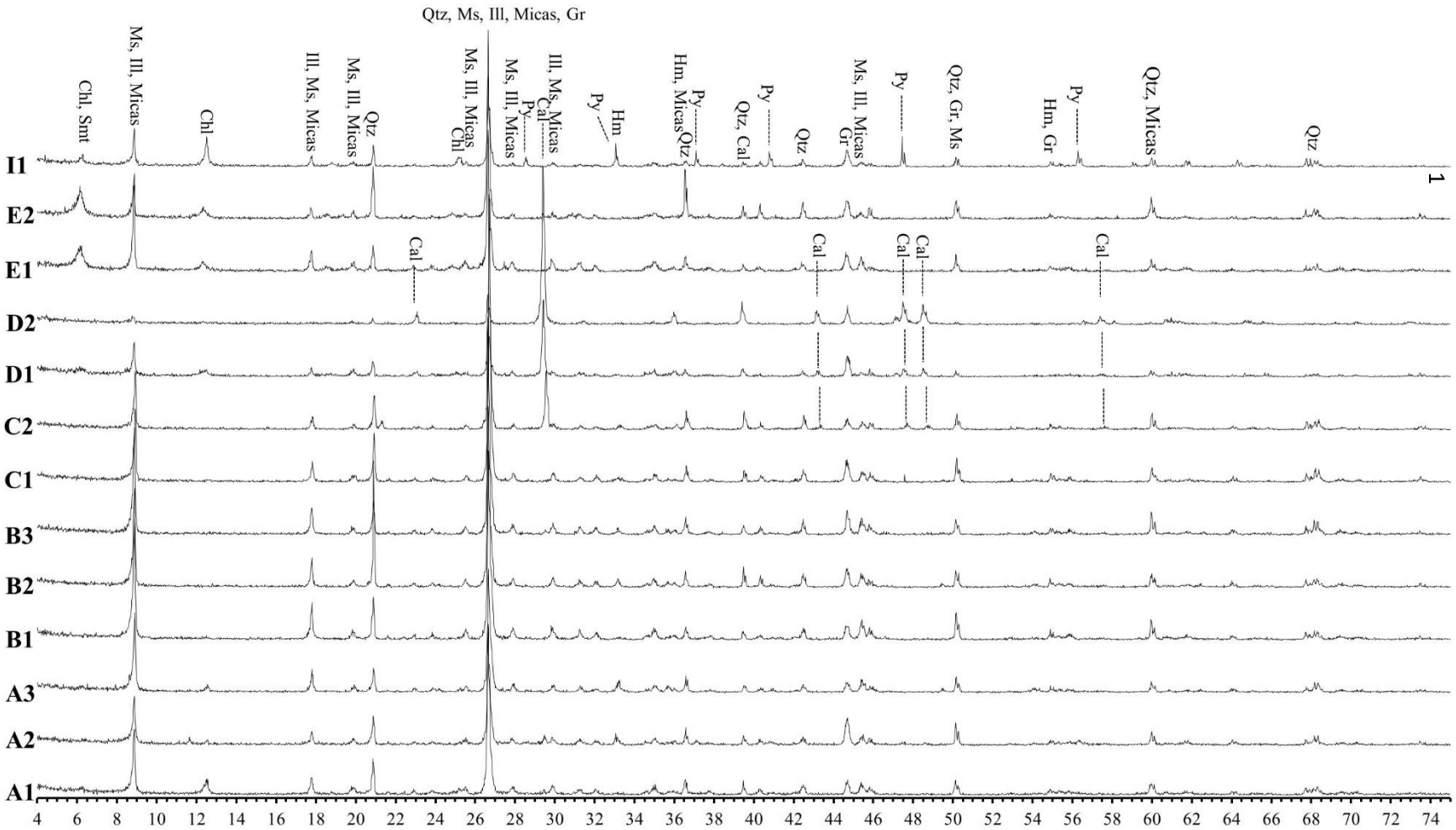

Figure 26. XRD patterns of bulk powder samples from core D9-08-24, samples A1 through I1, with mineral peak positions labeled. Intensity versus °2θ – Cu2α. Iron and/or magnesium carbonate peaks are not present in these samples, however, are present within the core. Profiles have the same scale with a vertical offset of 200 counts between profiles. Note highly leached samples, B1 through C2, have small and/or no reflections attributed to chlorite. Note appearance of the broad high intensity reflection at 14.38 Å (6.15 2θ) in graphitic slate samples (E1, E2) adjacent to the contact between graphitic slate and non-graphitic slate. Ank: ankerite; Cal: calcite; Chl: chlorite; Dol: dolomite; Fe: iron; Gr: graphite; Hem: hematite; Ill: illite; Micas: mica group; Ms: muscovite; Py: pyrite; Qtz: quartz. See Table 5.

magnesium carbonate-rich veins.

Hematite is distinguished by a low-intensity broad reflection at 2.69 Å (31.25 2θ). Quartz was distinguished by its strong reflections at 3.34 Å (26.65 2θ), 4.26 Å (20.85 2θ), and 1.82 Å (50.1 2θ). Graphitic slate samples have smaller quartz peak intensities. The primary graphite reflection occurs at 3.35 Å (26.6 2θ) which overlaps the primary quartz reflection. This overlap makes graphite detection, in low abundance samples, difficult. Peak intensity may have also been affected by graphite crystallinity. Graphite is more easily recognized by an intensity reduction and/or disappearance of the quartz 4.26 Å (20.85 2θ) peak; therefore the reflection at 3.35 Å (26.6 2θ) can be attributed to a combination of graphite and/or mica group minerals. The dense vein network at the non-graphitic to graphitic slate contact is primarily composed of iron and magnesium carbonate with lesser calcite (table 4, 5). Chlorite was distinguished by its primary reflection at 7.15 Å (12.35 2θ) and the reflection at 14.38 Å (6.15 2θ). The color of chlorite-rich rocks in hand sample ranges from pale green to dark green to black, possibly due to variation in iron content. The intensity of the chlorite reflection at 7.15 Å (12.35 2θ) decreases towards the contact between non-graphitic slate and graphitic slate (Fig. 25). Chlorite was present in the majority of the samples. However, leached and/or schistose intervals tended to have little to no chlorite. Green clay-rich shear surfaces and fault gouges were generally composed of chlorite, muscovite, and/or illite (Table 4, 5).

The graphitic slate is composed of graphite, quartz, chlorite, and illite and disseminated pyrite and iron oxide (Fig. 25, 26) (Table 4, 5). The samples from the non-graphitic to graphitic slate transition zone produced distinctive spectra (Fig. 25, 26). The samples produced a broad roughly symmetric reflection at 14.38 Å (6.15 2θ), while the

sharp mica reflection at 10.00 Å (8.85 2θ) was diminished. The broad reflection at 14.38 Å (6.15 2θ) is interrupted as a reflection produced by 14 Å chlorite, and/or mixed-layer chlorite-smectite. The intensity of the broad reflection at 14.38 Å (6.15 2θ) gradually increases towards the contact and decreases as graphite content increases. Transition zone samples tended to have less quartz. Sample D9-08-20J2 and D9-08-20I1 produced a reflection at approximately 28.9 Å (3.05 2θ) (Fig. 25b), which is also interpreted as mixed-layer chlorite-smectite reflection; however, it could also be produced by serpentine group minerals. The peak at 28.9 Å (3.05 2θ) is present, although less pronounced, in samples D9-08-24E1, and D9-08-24E2 (Fig. 26). Significant clumping occurred in the zirconia vessel while powdering sample D9-08-20I. Vermiculite and kaolinite minerals commonly appear as mineral matches as determined using the Highscore software. However, only the primary vermiculite reflection at approximately 14.38 Å (6.15 2θ) and/or the primary kaolinite reflection at approximately 7.15 Å (12.35 2θ) is well defined. The sample spectra lack secondary peaks that would be expected if vermiculite were present. Kaolin group minerals are structurally similar to serpentine group minerals, and its primary reflection overlaps with the primary chlorite reflection. Therefore, a more detailed clay-specific analysis, using XRF, XRD, and SEM, would be needed to help better understand clay and alteration mineralogy and textures.

Handheld X-ray Fluorescence Spectrometry Results

Eighty-eight spots on Michigan core samples were analyzed using a portable XRF spectrometer (Table 4, 5). It should be noted that the XRF data was collected with a low duration time of 30 seconds. Low duration times are associated with low precision and

high error; therefore, the data was used only for qualitative comparisons (see Table 4, 5). Furthermore, elements with high concentrations can decrease analytical precision and introduce error. These errors are associated with incorrect and/or low precision Ti and Ni counts, possibly attributed to high concentrations of K and Fe.

There is a strong positive correlation ($1.0 \geq Rs \geq 0.7$) between K and Ti, K and Zr, Ti and Zr, Fe and Rb, and Y and Zr. Samples with high K, Ti, Zr, and Cr generally correlate to samples with a high percentage of mica group minerals near schist layers and/or clay gouges. There is a moderate positive correlation ($0.7 \geq Rs \geq 0.6$) between Ca and Mn, and K and Y. The Ca and Mn correlation is possibly a result of the substitution of Mn into the crystal structure of carbonate minerals. There is a strong negative correlation ($1.0 \geq Rs \geq 0.7$) between Fe and Ni. The samples with the largest Fe peaks had smaller Ni peaks, possibly due to peak overlap and/or interference. Elevated Fe content appears to be primarily influenced by an increase in abundance of iron oxides. The highest Fe counts were recorded on spots with disseminated pyrite. There is a moderate negative correlation ($0.7 \geq Rs \geq 0.6$) between Ca and Fe, and Ca and Rb. The detection of Pb and As, with the portable XRF, is complicated by the overlapping of the K-alpha peak for arsenic and L-alpha peak for lead at approximately 10.5 KeV. The concentration and/or presence of Pb is usually determined by its L-Beta peak at 12.61KeV. However, the Fe-rich samples produced large Fe sum peaks at approximately 12.8 KeV, which made Pb detection difficult. Therefore, only samples with distinct Pb spectra were recorded.

Interpretation Whole-rock Drillcore Sites

The crystalline basement Michigamme slates display complex structural and textural relationships adjacent to the nonconformity at the Gogebic site (Fig. 23) (Table 4, 5). The nonconformity is cut by several small-displacement thrust faults in the hanging wall of larger thrust. The observations made here (Fig. 23-26) indicate hydrothermal alteration and fluid-rock interaction created leached, brecciated, and mineralized intervals in the Michigamme slate. Alteration mineral assemblages are composed of a combination of calcite, quartz, chlorite, smectite, iron oxide, and iron-magnesium carbonate (Table 4, 5). The slates are cut by multiple generations of carbonate veins. The carbonate veins consist of syntectonic and/or shear zone related shear and extensional veins and carbonate veins formed during earlier diagenesis. Fracture, fault, and vein formation and dilation was concentrated along cleavage planes, compositional contacts, fractures, and veins (Fig. 23) (Table 4, 5).

A transition zone at the contact between non-graphitic and graphitic slate is characterized by a widespread 1 to 2 m interval of pervasive carbonate veins (Fig. 23) (Table 4, 5). The transition zone has less quartz, and the clay mineralogy is dominated by chlorite and mixed-layer chlorite-smectite (Table 4, 5). Preferential deformation and alteration is widespread and concentrated adjacent to the contact, possibly related to mechanical and lithological contrast of the graphitic and non-graphitic slate (Fig. 24). I interpret that the graphitic and non-graphitic slates are discrete mechanical units and likely behaved differently during deformation. Smectite group clays and phyllosilicates are mechanically weak (e.g., Byerlee, 1978; Morrow et al., 1982, 1984; Olgaard et al.,

1997; Marone, 1998; Saffer & Marone, 2003; Morley et al., 2018), and smectite group minerals can weaken and expand during transformation to chlorite-smectite, or due to an addition of fluids and/or elevated temperatures (Morrow et al., 1982). The mixed-layer chlorite-smectite may have precipitated and/or occur as a result of transformation from smectite to chlorite-smectite during diagenesis and/or hydrothermal alteration. The contact between the graphitic slate and non-graphitic slate may have acted as a zone of mechanical weakness where fluids preferentially migrated.

The pervasive vein network with highly anastomosing, branching, and brecciated veins suggests high pore-fluid pressures and fluid-flow localization adjacent to the contact and faults (e.g., Parnell, 1999; Holland & Urai, 2010). Highly anastomosing vein networks have been interpreted to form during enhanced fluid flow related to structural weaknesses (e.g., Vandeginste et al., 2005; Holland & Urai, 2010). Variation in vein composition, cross-cutting relationships, and wall rock inclusion distribution may indicate multiple crack-seal events. Variation in clay mineralogy and graphite content may have impeded and/or focused fluid flow adjacent to the contact, with the graphite-rich slate serving as a barrier to flow. Faults and veins and implied elevated pore pressures might have facilitated fracture dilation and increased permeability (e.g., Moore et al., 1995; Morley et al., 2018). Potential weakening could have occurred by thermal pressurization of pore fluids (e.g., Ujiie & Tsutsumi, 2010; Faulkner et al., 2011), driven by the graphite-rich conductor. Slickensided and highly polished fault surfaces and clay smear, pressure solution seams, and S-C fabrics (Fig. 23) are evidence of slip localization. The drillcores are cut by multiple shear zones, including a shear zone oriented parallel to the contact between non-graphitic slate and graphitic slate, with the

weak chlorite- and smectite-rich and/or overpressured interval possibly serving as a "basal detachment".

The Michigan drillcores provide an example of deformation enhanced fluid flow and fluid flow localization along a structural weakness into crystalline basement rock. Enhanced fluid flow or permeability occurred parallel to layering and cleavage (e.g., Du Rouchet, 1981; Sibson, 1994). Hydrothermal alteration has clogged permeability pathways with fine-grained clay minerals and carbonate cement.

DISCUSSION

The nonconformities analyzed in this study consist of variably deformed, weathered, and altered Precambrian crystalline basement overlain by Paleozoic sedimentary rocks. The Paleozoic sedimentary rocks were deposited on a Precambrian rock surface shaped and molded by erosion, and physical and chemical weathering. At the New Mexico sites, the sedimentary rocks were deposited atop a phyllosilicate-rich weathered horizon, of variable thickness, that developed on top of fractured and deformed crystalline basement. The crystalline basement adjacent to the nonconformity at the Colorado site is relatively fresh and unweathered and overlain by low permeability sandstones. The nonconformity and adjacent crystalline basement and sedimentary rocks have undergone deformation and alteration associated with subsequent episodes of diagenesis, burial, and exhumation. Brittle deformation and alteration manifest as fractures, joints, veins, and outcrop- to map-scale faults that cut the nonconformity and adjacent rocks. The sedimentary and crystalline rocks are overprinted by dissolution and precipitation resulting from the circulation of fluids, laterally and vertically, and related fluid-rock interactions.

The nonconformity and underlying slates in the Michigan rock were overprinted by clay mineralization, carbonate veins, and dissolution voids during hydrothermal alteration. Fluid flow and alteration proximal to the nonconformities commonly occurred along preexisting structures, which now exhibit distinct mineralogy and/or are infilled with miscellaneous secondary minerals. The structures and lithological features observed proximal to the nonconformities likely impact the hydrological communication between

the sedimentary rocks and crystalline basement. Modeling the interface as a thin discrete boundary is potentially an oversimplification of nonconformity heterogeneities and their impacts on fluid flow.

Nonconformity Architecture

Utilizing the New Mexico, Colorado, and Michigan analogs we have developed several conceptual geological and hydrological models for basal nonconformities. The models consist of a basal sedimentary reservoir with moderate to high permeability and hydraulic conductivity situated atop the crystalline basement. The reservoir is capped by a low permeability and hydraulic conductivity unit, e.g., shale or limestone. With hypothetical fluid injection occurring in the basal reservoir, analogous to fluid injection occurring in Kansas and Oklahoma.

(1) Low permeability and hydraulic conductivity seal atop crystalline basement, e.g., a well-developed saprolite horizon, overlying sedimentary layer, or fresh crystalline basement.

(2) Faulted nonconformity with high permeability and hydraulic conductivity damage zone, and low permeability and hydraulic conductivity core.

(3) High permeability and hydraulic conductivity fractured crystalline basement. Structurally controlled rock mass permeability facilitated by the presence of discrete fracture network.

Fully coupled hydromechanical modeling of pore pressure migration proximal to nonconformities from Ortiz (2017), and Ortiz et al. (2018), indicate that the presence of a (1) continuous low permeability and hydraulic conductivity seal will reduce fluid

pressure transmission into the crystalline basement; (2) discontinuous low permeability and hydraulic conductivity seal may slightly increase reservoir pressures and fluid pressure transmission into the crystalline basement; (3) fault with high permeability and high hydraulic conductivity damage zone enhances fluid pressure migration into the crystalline basement, with a positive correlation between damage zone width and depth and magnitude of pore pressure transmission; (4) continuous high permeability and hydraulic conductivity layer will allow pore pressure dissipation (Ortiz, 2017).

Undeformed or "pristine" crystalline basement rocks typically have low hydraulic conductivity and/or permeability (Brace, 1980; Smith et al., 1990; Clauser, 1992), however, crystalline rocks can have higher permeabilities depending on tectonic setting, lithology, and fracture characteristics (Ranjram et al., 2015). Hydraulic conductivity can be several orders of magnitude higher for highly jointed and fractured crystalline basement (Brace, 1980; Clauser, 1992), however, the permeability generally decreases with depth (Manning & Ingebritsen, 1999; Stober & Bucher, 2015). Permeability in weathered crystalline rock and/or regolith can be several orders of magnitude greater than the fresh crystalline basement (Paasche et al., 2006; Riber et al., 2016, 2017; Lothe et al., 2018).

Regolith development and thickness at the Earth's surface depends on topography and drainage characteristics (Taylor & Eggleton, 2001; Clair et al., 2015). Hilltops and valleys, specifically broad elevated areas can develop thick regolith horizons (Taylor & Eggleton, 2001). Thickness variations in the weathered horizon, at the nonconformity, could potentially create permeability architectures that would enhance or decrease fluid migration into the crystalline basement. Saprolite typically has low bulk density, elevated

porosity, and low permeability while fresh crystalline rock has high bulk density, and low permeability and porosity (Lumb, 1975; McNally, 1992; Taylor & Eggleton, 2001). A well-developed saprolite zone, with high phyllosilicate content, may have low transmissivity and impede fluid pressure migration into the crystalline rock. However, the saprock zone and/or the zone containing abundant corestones can have elevated permeability and hydraulic conductivity, several magnitudes higher than fresh crystalline basement (Taylor & Eggleton, 2001; Riber et al., 2016, 2017; Lothe et al., 2018). This zone may allow for lateral pore pressure dissipation; however, it could also allow pore pressures to interact with and infiltrate more potentially weakened structures. Lithology, lithological contacts, faults, weathered and/or altered zones are important controls on permeability and strength heterogeneity and anisotropy proximal to nonconformities. Strength contrasts and associated fracture network heterogeneity may facilitate fluid flow localization.

A well-developed fine-grained phyllosilicate-rich weathered horizon atop the crystalline basement would likely reduce fluid and pore pressure transmission into the crystalline basement (Ortiz et al., 2018). However, this layer can be discontinuous juxtaposing the basal sedimentary units or reservoir and high permeability fractured crystalline basement. Faults that cut nonconformities with high permeability damage zones and low permeability cores which may focus fluid flow and allow increased pore fluid pressure transmission into the crystalline basement (e.g., Ortiz, 2017). Small-scale faults that offset the nonconformity, e.g., the map-scale faults at the New Mexico field sites, would be difficult to resolve in seismic data. Fault zones are primary conduits for fluid and pore fluid pressure migration (Cox, 1991).

The Pawnee earthquake, magnitude 5.8, was preceded by several moment magnitude 3 and greater earthquakes (Chen et al., 2017). These smaller magnitude earthquakes, sometimes occurring on unresolved faults, can alter the stress field of proximal faults (e.g., Sibson, 1994; Chen et al., 2017). Furthermore, shear failure may allow for transient increases in fault zone permeability and linkage and dilation of pre-existing structures (e.g., Sibson, 1994), and migration of pore fluid pressures to larger critically stressed structures whose failure can lead to more damaging earthquakes. Permeability and structural anisotropy and potential of fault failure depend on the tectonic regime and orientation of the stress field (e.g., Du Rouchet, 1981; Sibson, 1994; Ranjram et al., 2015). In an extensional regime, the amount of shear stress required for reactivation of a normal fault is approximately four times less than required for reactivation of thrust fault in a compressional regime, at the same depth and fluid pressure level (Sibson 1974; Sibson, 1994). The depth of the fluid injection in relation to the crystalline basement may also affect the seismic moment release (Hincks et al., 2018). These relationships can be complicated by faults with fault seal and fault valve behavior.

Low permeability fault zones, hydrothermally mineralized or phyllosilicate-rich zones may result in reservoir compartmentation, which may allow pore pressures to build-up in the Precambrian crystalline basement. Hydrofracturing will occur if the pore fluid pressures exceed the tensile strength of the surrounding rock mass. Strength contrasts and shear-failure induced permeability pathways may develop in the crystalline basement. Structural and lithological heterogeneities proximal to basal nonconformities likely result in hydro- and geomechanical anisotropy and heterogeneity at the micro- to megascopic scales. Micro- to megascopic scale ductile or brittle deformation structures

can be reactivated, resulting in changes in physical rock properties.

Highly fractured and jointed crystalline basement adjacent to the nonconformity may increase the hydraulic communication of the basal reservoir and basement rocks, and facilitate pore fluid pressure migration into the crystalline basement or lateral dissipation of pore fluid pressures. The hydromechanical behavior of the crystalline basement would be dependent on the fracture network and permeability heterogeneity and anisotropy. Physical weathering or brittle deformation of the crystalline basement can create interconnected joint, and fracture networks (e.g., New Mexico, Colorado, and Michigan) that may provide pathways for pore pressure transmission into the crystalline basement. If lateral dissipation of pore pressure were to occur, pore fluid pressures may interact with more critically stressed faults in a shorter period. Fractured crystalline basement hydrocarbon reservoirs occur throughout the world including in Kansas. In well logs from drill holes in Kansas, a sharp change in the physical rock proprieties is observed at the nonconformity. It is possible that fluid migration, associated with fluid injection, will follow similar pathways that the natural hydrocarbons followed into the crystalline basement reservoir. Fluid accumulation into a crystalline basement reservoir, with a structural or lithological trap, may eventually lead to pore pressure migration down into the crystalline basement along vertical fractures or joints. Additionally, juxtaposition associated with cutting faults and variable lithology may modify flow paths and result in architectures that enhance or reduce pore pressure migration into crystalline basement rocks.

CONCLUSIONS

We used structural, hydrological, geomechanical, and geochemical techniques to characterize and evaluate the rock properties and the interaction between mechanical, hydrological, and chemical processes proximal to exhumed nonconformities. The nonconformities analyzed in this study display a range of structural, lithological, mineralogical, and geochemical styles and characteristics which can vary significantly over relatively small spatial extents. The basal nonconformity can consist of variable lithology and fracture characteristics over short distances. Fluid injection may occur adjacent to zones of enhanced permeability within sedimentary rocks hydromechanically coupled to the crystalline basement. The lithological and structural heterogeneities, proximal to nonconformities, likely contribute to variable degrees of mechanical coupling between the basal sandstone and underlying crystalline basement. Highly fractured and jointed crystalline basement adjacent to the nonconformity may increase the hydraulic communication of the basal reservoir and basement rocks, and facilitate pore fluid pressure migration into the crystalline basement or lateral dissipation of pore fluid pressures. The hydromechanical behavior of the crystalline basement would be dependent on the fracture network and permeability heterogeneity and anisotropy. Our FracPaQ results show that fracture network heterogeneity within the crystalline basement may contribute to permeability anisotropy. The permeability architecture and fluid flow structure of nonconformities can be perturbed by faults, a weathered horizon, lithology, and dilation of preexisting structures. The analogs, observed in this study, also provide direct evidence of concentrated fluid flow along preexisting structures, and fluid-rock

interaction proximal to and along nonconformities.

We have identified several features that may account for permeability heterogeneity and anisotropy proximal to nonconformities including the presence and nature of saprolith, faults, shear zones, geomechanical and lithological disparities, grain-size variation, mineral precipitation, mineral dissolution, and fracture, joint, bedding, and foliation planes.

Further study including laboratory measurements of mechanical rock properties including porosity and permeability testing are required to gain a better understanding of the effects of the nonconformity zone on the migration of pore fluid pressures. Faults cutting the nonconformity, favorable structural and lithological architectures, and/or highly fractured crystalline basement may potentially facilitate pore fluid pressure migration into the crystalline basement. Minimizing risk of induced seismicity can be achieved by thorough injection site characterization, on a case by case basis, and targeting reservoirs or formations with ample buffering provided by sedimentary units (Hinicks et al., 2018), as seen in the Williston basin, and away from crystalline basement faults (Ortiz, 2017). The presence of a well-developed, phyllosilicate-rich, and low permeability weathered or altered zone atop the crystalline basement can significantly reduce pore pressure transmission into the crystalline basement rock (Ortiz, 2017). This thesis introduces some of the geologic factors that may control fluid flow structure adjacent to nonconformities and their possible significance to the interplay of deformation, fluid flow, and induced seismicity.

REFERENCES

Armstrong, A. K., & Mamet, B. L. (1974). Biostratigraphy of the Arroyo Penasco Group, Lower Carboniferous (Mississippian), north-central New Mexico. In C. T. Siemers, L. A. Woodward, J. F. Callender (Eds.), *New Mexico Geological Society, Ghost Ranch silver anniversary, guidebook 25, 1974* (pp. 145-158). Socorro, NM: New Mexico Geological Society, Inc.

Armstrong, A. K., Mamet, B. L., & Repetski, J. E. (1992). Stratigraphy of the Mississippian system, south-central Colorado and north-central New Mexico. *U.S. Geological Survey Bulletin*, (1787-EE). Retrieved from http://pubs.er.usgs.gov/publication/b1787EE

Baars, D. L. (1965). Pre-Pennsylvanian paleotectonics of southwestern Colorado (San Juan County and vicinity) and east-central Utah, (Doctoral dissertation). Boulder, CO: University of Colorado.

Baars, D. L. (1966). Pre-Pennsylvanian paleotectonics--key to basin evolution and petroleum occurrences in Paradox Basin, Utah and Colorado. *American Association of Petroleum Geologists Bulletin*, 50(10), 2082-2111. http://dx.doi.org/10.1306/5D25B70D-16C1-11D7-8645000102C1865D

Baars, D. L., & Ellingson, J. A. (1984). Geology of the western San Juan Mountains. In Brew D. C. (Ed.), *Rocky Mountain Section, Geological Society of America, Field trip guidebook: 37th Annual Meeting* (pp. 1-45). Durango, CO: Fort Lewis College & Four Corners Geological Society.

Baltz, E. H. (1972). Geologic map and cross sections of the Gallinas Creek area, Sangre de Cristo Mountains, San Miguel County, New Mexico *(MAP I-673*). Reston, VA: U.S. Geological Survey. https://doi.org/10.3133/i673

Baltz, E. H., & Read, C. B. (1960). Rocks of Mississippian and probable Devonian age in Sangre de Cristo Mountains, New Mexico. *American Association of Petroleum Geologists Bulletin*, 44(11), 1749-1774. http://dx.doi.org/10.1306/0BDA623C-16BD-11D7-8645000102C1865D

Baltz, E. H., & Myers, D. A. (1999). *Stratigraphic framework of upper Paleozoic rocks, southeastern Sangre de Cristo Mountains, New Mexico, with a section on speculations and implications for regional interpretation of Ancestral Rocky Mountains paleotectonics*. New Mexico, Bureau of Mines and Mineral Resources, memoir 48. Socorro, NM: Authority of State of New Mexico.

Baltz, E. H., & O'Neil, M. J. (1986). Geologic map and cross sections of the Sapello River area, Sangre de Cristo Mountains, Mora and San Miguel Counties, New Mexico (*MAP I-1575*). Reston, VA: U.S. Geological Survey. https://doi.org/10.3133/i1575

Barovich, K. M., Patchett, P. J., Peterman, Z. E., & Sims, P. K. (1989). Nd isotopes and the origin of 1.9-1.7 Ga Penokean continental crust of the Lake Superior region. *Geological Society of America Bulletin*, 101(3), 333-338. https://doi.org/10.1130/0016-7606(1989)101<0333:NIATOO>2.3.CO;2

Barton, C. A., Zoback, M. D., & Moos, D. (1995). Fluid flow along potentially active faults in crystalline rock. *Geology*, 23(8), 683-686. https://doi.org/10.1130/0091-7613(1995)023<0683:FFAPAF>2.3.CO;2

Bornhorst, T. J., & Barron, R. J. (2011). Copper deposits of the western Upper Peninsula of Michigan. In J. D. Miller, G. J. Hudak, C. Wittkop, P. I. McLaughlin (Eds.), *Geological Society of America,*

Archean to Anthropocene: Field guides to the geology of the Mid-Continent of North America (Vol. 24, pp. 83-99). Boulder, CO: Geological Society of America. http://dx.doi.org/10.1130/2011.0024(05)

Brace, W. F. (1980). Permeability of crystalline and argillaceous rocks. *International Journal of Rock Mechanics and Mining Sciences and Geomechanics Abstracts*, 17(5), 241-251. https://doi.org/10.1016/0148-9062(80)90807-4

Brace, W. F. (1984). Permeability of crystalline rocks: New in situ measurements. *Journal of Geophysical Research: Solid Earth*, 89(B6), 4327-4330. https://doi.org/10.1029/JB089iB06p04327

Byerlee, J. (1978). Friction of rocks. *Pure and Applied Geophysics*, 116(4-5), 615-626. https://doi.org/10.1007/BF00876528

Caine, J. S., Evans, J. P., & Forster, C. B. (1996). Fault zone architecture and permeability structure. *Geology*, 24(11), 1025-1028. https://doi.org/10.1130/0091-7613(1996)024<1025:FZAAPS>2.3.CO;2

Cannon, W. F. (1994). Closing of the Midcontinent rift-A far—field effect of Grenvillian compression. *Geology*, 22(2), 155-158. https://doi.org/10.1130/0091-7613(1994)022<0155:COTMRA>2.3.CO;2

Cannon, W. F., & Nicholson, S. W. (1992). Revisions of stratigraphic nomenclature within the Keweenawan Supergroup of northern Michigan. *U.S. Geological Survey Bulletin* (1970), A1-A8.

Cather, S. M., Chapin, C. E., & Kelley, S. A. (2012). Diachronous episodes of Cenozoic erosion in southwestern North America and their relationship to surface uplift, paleoclimate, paleodrainage, and paleoaltimetry. *Geosphere*, 8(6), 1177-1206. http://dx.doi.org/10.1130/GES00801.1

Chang, K. W., & Segall, P. (2017). Reduction of injection-induced pore-pressure and stress in basement rocks due to basal sealing layers. *Pure and Applied Geophysics*, 174(7), 2649-2661. https://doi.org/10.1007/s00024-017-1567-1

Chapin, C. E., Kelley, S. A., & Cather, S. M. (2014). The Rocky Mountain Front, southwestern USA. *Geosphere*, 10(5), 1043-1060. http://dx.doi.org/10.1130/GES01003.1

Chen, X., Nakata, N., Pennington, C., Haffener, J., Chang, J. C., He, X., Zhan Z., Ni S., & Walter, J. I. (2017). The Pawnee earthquake as a result of the interplay among injection, faults and foreshocks. *Scientific Reports*, 7, 4945. https://doi.org/10.1038/s41598-017-04992-z

Chester, F. M., & Logan J. M. (1986). Implications for mechanical properties of brittle faults from observations of the Punchbowl fault zone, California. *Pure and Applied Geophysics*, 124(1-2), 79-106. https://doi.org/10.1007/BF00875720

Clair, J. S., Moon, S., Holbrook, J. T., Perron, J. T., Riebe, C. S., Martel, S. J., Carr, B., Harman, C., Singha, K., & Richter deB. (2015). Geophysical imaging reveals topographic stress control of bedrock weathering. *Science*, 350(6260), 534-538. https://doi.org/10.1126/science.aab2210

Clauser, C. (1992). Permeability of crystalline rocks. *Eos, Transactions*, *American Geophysical Union*, 73(21), 233-238. https://doi.org/10.1029/91EO00190

Coney, P. J., & Reynolds, S. J. (1977). Cordilleran Benioff zones. *Nature*, 270(5636), 403-406. https://doi.org/10.1038/270403a0

Cox, S. F., Wall, V. J., Etheridge, M. A., & Potter, T. F. (1991). Deformational and metamorphic processes in the formation of mesothermal vein-hosted gold deposits - examples from the Lachlan Fold Belt in central Victoria, Australia. *Ore Geology Reviews*, 6(5), 391-423. https://doi.org/10.1016/0169-1368(91)90038-9

Craddock, J. P., Konstantinou, A., Vervoort, J. D., Wirth, K. R., Davidson, C., Finley-Blasi, L., Juda, N. A., & Walker, E. (2013). Detrital zircon provenance of the Mesoproterozoic Midcontinent Rift, Lake Superior region, U.S.A. *Journal of Geology*, 121(1), 57-73. https://doi.org/10.1086/668635

Cui, T., Yang, J., & Samson, I. M. (2012). Tectonic deformation and fluid flow: implications for the formation of unconformity-related uranium deposits. *Economic Geology*, 107, 147-163. https://doi.org/10.2113/econgeo.107.1.147

Cuong, T. X., & Warren, J. K. (2009). Bach Ho Field, A fractured granitic basement reservoir, Cuu Long basin, offshore SE Vietnam: A "Buried Hill" play. *Journal of Petroleum Geology*, 32(2), 129-156. https://doi.org/10.1111/j.1747-5457.2009.00440.x

Davis, G. H., & Coney, P. J. (1979). Geologic development of the Cordilleran metamorphic core complexes. *Geology*, 7(3), 120-124. https://doi.org/10.1130/0091-7613(1979)7<120:GDOTCM>2.0.CO;2

Degen, T., Sadki, M., Bron, E., König, U., & Nénert, G. (2014). The HighScore suite. *Powder Diffraction*, 29(S2), S13-S18. https://doi.org/10.1017/S0885715614000840

Delvigne, J. E. (1998). *Atlas of micromorphology of mineral alteration and weathering*. The Canadian Mineralogist. Special Publication, 3. Ontario, Canada: Mineralogical Association of Canada.

Deng, K., Liu, Y., & Harrington, R. M. (2016). Poroelastic stress triggering of the December 2013 Crooked Lake, Alberta, induced seismicity sequence. *Geophysical Research Letters*, 43(16), 8482-8491. https://doi.org/10.1002/2016GL070421

Dickinson, W. R. (1978). Plate tectonic evolution of North Pacific rim. *Journal of Physics of the Earth*, 26(Supplement), S1-S19. https://doi.org/10.4294/jpe1952.26.Supplement_S1

Dickinson, W. R., & Lawton, T. F. (2003). Sequential intercontinental suturing as the ultimate control for Pennsylvanian Ancestral Rocky Mountains deformation. *Geology*, 31(7), 609-612. https://doi.org/10.1130/0091-7613(2003)031<0609:SISATU>2.0.CO;2

Dickinson, W. R., & Snyder, W. S. (1978). Plate tectonics of the Laramide orogeny. In V. Matthews III (Ed.), *Geological Society of America memoir 151: Laramide folding associated with basement block faulting in the western United States* (pp. 355-366). Boulder, CO: Geological Society of America.

Du Rouchet, J. (1981). Stress fields, a key to oil migration. *American Association of Petroleum Geologists Bulletin*, 65(1), 74-85.

Eardley, A. J. (1951). *Structural geology of North America*. New York, NY: Harper and Brothers.

Eaton, G. P. (1987). Topography and origin of the southern Rocky Mountains and Alvarado Ridge. In M. P. Coward, J. F. Dewey., P. L. Hancock (Eds.), *Continental extensional tectonics, Geological Society, London, Special Publications no. 28* (pp. 355-369). London, ENG: The Geological Society by Blackwell Scientific Publications. https://doi.org/10.1144/GSL.SP.1987.028.01.22

Eaton, G. P. (2008). Epeirogeny in the Southern Rocky Mountains region: Evidence and origin. *Geosphere*, 4(5), 764-784. https://doi.org/10.1130/GES00149.1

Ellsworth, W. L. (2013). Injection-induced earthquakes. *Science*, 341(6142), 1225942. https://doi.org/10.1126/science.1225942

Ellsworth, W. L., Llenos, A. L., McGarr, A. F., Michael, A. J., Rubinstein, J. L., Mueller, C. S., Petersen, M. D., & Calais, E. (2015). Increasing seismicity in the U.S. midcontinent: Implications for earthquake hazard. *The Leading Edge*, 34(6), 618-626. https://doi.org/10.1190/tle34060618.1

Evans, J. P. (1988). Deformation mechanisms in granitic rocks at shallow crustal levels. *Journal of Structural Geology*, 10(5), 437-443. https://doi.org/10.1016/0191-8141(88)90031-4

Evans, J. P., Forster, C. B., & Goddard J. V. (1997). Permeability of fault-related rocks, and implications for hydraulic structure of fault zones. *Journal of Structural Geology*, 19(11), 1393-1404. https://doi.org/10.1016/S0191-8141(97)00057-6

Faulkner, D. R., Mitchell, T. M., Behnsen, J., Hirose, T., & Shimamoto, T. (2011). Stuck in the mud? Earthquake nucleation and propagation through accretionary forearcs. *Geophysical Research Letters*, 38, L18303. https://doi.org/10.1029/2011GL048552

Frohlich, C. (2012). Two-year survey comparing earthquake activity and injection-well locations in the Barnett Shale, Texas. *Proceedings of the National Academy of Sciences*, 109(35), 13934-13938. https://doi.org/10.1073/pnas.1207728109

Goebel, T. H. W., Hosseini, S. M., Cappa, F., Hauksson, E., Ampuero, J. P., Aminzadeh, F., & Saleeby, J. B. (2016). Wastewater disposal and earthquake swarm activity at the southern end of the Central Valley, California. *Geophysical Research Letters*, 43(3), 1092-1099. https://doi.org/10.1002/2015GL066948

Gonzales, D. A., (1997). Crustal evolution of the Needle Mountains Proterozoic complex, southwestern Colorado (Doctoral dissertation). Lawrence, KS: University of Kansas.

Gonzales, D. A., Stahr, D. W., & Kirkham, R. M. (2003). Geologic map of the Hermosa quadrangle, La Plata County, Colorado. Geologic. Open File Reports (*OF-02-01* with 28 p. text). Denver, CO: Colorado Geological Survey.

Goodman, R. E. (1989). *Introduction to rock mechanics*. New York, NY: John Wiley & Sons.

Graham, S. A., Ingersoll, R. V., & Dickinson, W. R. (1976). Common provenance for lithic grains in Carboniferous sandstones from Ouachita Mountains and Black Warrior Basin. *Journal of Sedimentary Research*, 46(3), 620-632. https://doi.org/10.1306/212F7009-2B24-11D7-8648000102C1865D

Gutmanis, J. (2009). Basement Reservoirs - A review of their geological and production characteristics. Paper presented at the International Petroleum Technology Conference, Doha, Qatar (IPCT 13156, 7 pp.). https://doi.org/10.2523/IPTC-13156-MS

Hartz, E. H., Martinsen, B. B., Øverli, P. E., Lie, H., Ditcha, E. M., Schmid, D. W., & Medvedev, S. (2013). Newly discovered giant oil fields of North Sea—The role of fractured basement highs. In First European Association of Geoscientists and Engineers (EAGE) and Brazilian Geophysical Society (SBGf) Workshop: *Fractures in Conventional and Unconventional Reservoirs, Extended Abstracts*: Rio de Janeiro, Brazil, 4 pp. https://doi.org/10.3997/2214-4609.20131805

Healy, D., Rizzo, R. E., Cornwell, D. G., Farrell, N. J. C., Watkins, H., Timms, N. E., Gomez-Rivas, E., & Smith, M. (2017). FracPaQ: A MATLAB™ toolbox for the quantification of fracture patterns. *Journal of Structural Geology*, 95, 1-16. https://doi.org/10.1016/j.jsg.2016.12.003

Healy, J. H., Rubey, W. W., Griggs, D. T., & Raleigh, C. B. (1968). The Denver earthquakes. *Scienc*e, 161(3848), 1301-1310. https://doi.org/10.1126/science.161.3848.1301

Hennings, P., Allwardt, P., Paul, P., Zahm, C., Reid, R., Alley, H., Kirschner, R., Lee, B., & Hough, E. (2012). Relationship between fractures, fault zones, stress, and reservoir productivity in the Suban gas field, Sumatra, Indonesia. *American Association of Petroleum Geologists Bulletin*, 96(4), 753-772. https://doi.org/10.1306/08161109084

Hesseltine, G., Evans, J. P., Kerner, K., & Mozley, P. S. (2016). Structural diagenesis and micro- to macro-scale structural architecture of basal nonconformities. *Geological Society of America Abstracts with Programs* (Vol. 48, No. 7). https://doi.org/10.1130/abs/2016AM-284922

Hincks, T., Aspinall, W., Cooke, R., & Gernon, T. (2018). Oklahoma's induced seismicity strongly linked to wastewater injection depth. *Science*, 359(6381), 1251-1255. https://doi.org/10.1126/science.aap7911

Hoeve, J., & Sibbald, T. I. I. (1978). On the genesis of Rabbit Lake and other unconformity-type uranium deposits in northern Saskatchewan, Canada. *Economic Geology*, 73(8), 1450-1473. https://doi.org/10.2113/gsecongeo.73.8.1450

Holdsworth, R. E. (2004). Weak faults--Rotten cores. *Science*, 303(5655), 181-182. https://doi.org/10.1126/science.1092491

Holland, M., & Urai, J. L. (2010). Evolution of anastomosing crack–seal vein networks in limestones: Insight from an exhumed high-pressure cell, Jabal Shams, Oman Mountains. *Journal of Structural Geology*, 32(9), 1279-1290. https://doi.org/10.1016/j.jsg.2009.04.011

Hornbach, M. J., DeShon, H. R., Ellsworth, W. L., Stump, B. W., Hayward, C., Frohlich, C., Oldham H. R., Olson J. E., Magnani M. B., Brokaw C., & Luetgert, J. H. (2015). Causal factors for seismicity near Azle, Texas. *Nature Communications*, 6, 6728. https://doi.org/10.1038/ncomms7728

Horton, S. (2012). Disposal of hydrofracking waste fluid by injection into subsurface aquifers triggers earthquake swarm in central Arkansas with potential for damaging earthquake. *Seismological Research Letters*, 83(2), 250-260. https://doi.org/10.1785/gssrl.83.2.250

Hubbert, M. K., & Willis, D. G. (1955). Important fractured reservoirs in the United States. In A. Barbier (Ed.), *Proceeding: Fourth World Petroleum Congress, Rome – June, 1955* (pp. 58-81). Moscow, RUS: Publishing House of the USSR Academy of Sciences.

International society for rock mechanics commission on standardization of laboratory and field tests, (1978). Suggested methods for the quantitative description of discontinuities in rock masses.

International Journal of Rock Mechanics and Mining Sciences and Geomechanics Abstracts (Vol. 15, No. 6, pp. 319-368). https://doi.org/10.1016/0148-9062(78)91472-9

Jefferson, C. W., Thomas, D. J., Gandhi, S. S., Ramaekers, P., Delaney, G., Brisbin, D., Cutts, C., Quirt, D., Portella, P., & Olson, R. A. (2007). Unconformity-associated uranium deposits of the Athabasca Basin, Saskatchewan and Alberta. *Geological Survey of Canada Bulletin*, 588, 23-68. http://dx.doi.org/10.4095/223742

Jørstad, A. (2012). Johan Sverdrup–Offshore Norway: The Story behind the Giant Sverdrup Discovery. *Search and Discovery Article* (20177). http://www.searchanddiscovery.com/pdfz/documents/2012/20177jorstad/ndx_jorstad.pdf.html

Keranen, K. M., Savage, H. M., Abers, G. A., & Cochran, E. S. (2013). Potentially induced earthquakes in Oklahoma, USA: Links between wastewater injection and the 2011 Mw 5.7 earthquake sequence. *Geology*, 41(6), 699-702. https://doi.org/10.1130/G34045.1

Keranen, K. M., Weingarten, M., Abers, G. A., Bekins, B. A., & Ge, S. (2014). Sharp increase in central Oklahoma seismicity since 2008 induced by massive wastewater injection. *Science*, 345(6195), 448-451. https://doi.org/10.1126/science.1255802

Kerner, K. R. (2015). *Permeability architecture of faulted nonconformities: Implications for induced seismicity.* (Master's thesis). Socorro, NM: New Mexico Institute of Mining and Technology.

Kim, W.-Y. (2013). Induced seismicity associated with fluid injection into a deep well in Youngstown, Ohio. *Journal of Geophysical Research: Solid Earth*, 118(7), 3506-3518. https://doi.org/10.1002/jgrb.50247

Kluth, C. F., & Coney, P. J. (1981). Plate tectonics of the Ancestral Rocky Mountains. *Geology*, 9(1), 10-15. https://doi.org/10.1130/0091-7613(1981)9<10:PTOTAR>2.0.CO;2

Kluth, C. F. (1986). Plate tectonics of the ancestral rocky mountains. In J. A. Peterson (Ed.), *American Association of Petroleum Geologists Memoir 41: Paleotectonics and sedimentation in the Rocky Mountain Region, United States* (pp. 353-369). Tulsa, OK: The American Association of Petroleum Geologists.

Kocurek, G., & Dott, R. H., Jr. (1983). Jurassic paleogeography and paleoclimate of the central and southern Rocky Mountain region. In M. W. Reynolds, E. D. Dolly (Eds.), *Mesozoic paleogeography of the west-central United States: Rocky Mountain paleogeography symposium, 2* (pp. 101-116). Denver, CO: The Rocky Mountain Section Society of Economic Paleontologists and Mineralogists.

Landes, K. K., Amoruso, J. J., Charlesworth, L. J., Jr., Heany, F., & Lesperance, P.-J. (1960). Petroleum resources in basement rocks. *American Association of Petroleum Geologists Bulletin*, 44(10), 1682-1691.

Lanson, B., & Champion, D. (1991). The I/S-to-illite reaction in the late stage diagenesis. *American Journal of Science*, 291(5), 473-506. https://doi.org/10.2475/ajs.291.5.473

Lee M. R., Waldron K. A., & Parsons, I. (1995). Exsolution and alteration microtextures in alkali feldspar phenocrysts from the Shap granite. *Mineralogical Magazine,* 59, 63-78.

Lemen, D., Lindline, J., & Bosbyshell, H. (2015). The Gallinas Canyon gneiss; a window into the nature of Paleoproterozoic events in northern New Mexico. In J. Lindline, M. Petronis, J. Zebrowski (Eds.), *New Mexico Geological Society, Geology of the Las Vegas Region, guidebook 66, 2015* (pp. 185-192). Socorro, NM: New Mexico Geological Society, Inc.

Lessard, R. H., & Bejnar, W. (1976). Geology of the Las Vegas area. In R. C. Ewing, B. S. Kues (Eds.), *New Mexico Geological Society, Vermejo Park, guidebook 27, 1976* (pp. 103-108). Socorro, NM: New Mexico Geological Society, Inc.

Lindline, J., Kues, B., Bentson, K., & Zebrowski, J. (2015). Las Vegas to Mineral Hill, Johnson Mesa, Gallinas Canyon, and Montezuma. In J. Lindline, M. Petronis, J. Zebrowski (Eds.), *New Mexico Geological Society, Geology of the Las Vegas Region, guidebook 66, 2015* (pp. 1-37). Socorro, NM: New Mexico Geological Society, Inc.

Liu, L., & Gurnis, M. (2010). Dynamic subsidence and uplift of the Colorado Plateau. *Geology*, 38(7), 663-666. https://doi.org/10.1130/G30624.1

Liu, S., Nummedal, D., & Gurnis, M. (2014). Dynamic versus flexural controls of Late Cretaceous Western Interior Basin, USA. *Earth and Planetary Science Letters*, 389, 221-229. https://doi.org/10.1016/j.epsl.2014.01.006

Lothe, A. E., Emmel, B., Bergmo, P. E., Akervoll, I., Todorovic, J., Bhuiyan, M. H., & Knies, J. (2018). Porosity, permeability and compaction trends for Scandinavian regoliths. *Marine and Petroleum Geology*, 92, 319-331. https://doi.org/10.1016/j.marpetgeo.2017.10.027

Lucia, F. J. (1983). Petrophysical Parameters Estimated From Visual Descriptions of Carbonate Rocks: A Field Classification of Carbonate Pore Space. *Journal of Petroleum Technology*, 35(03), 629-637. https://doi.org/10.2118/10073-PA

Lucia, F. J. (1999). *Carbonate reservoir characterization*. Verlag, Berline: Springer.

Lumb, P. (1975). Slope failures in Hong Kong. *Quarterly Journal of Engineering Geology and Hydrogeology*, 8(1), 31-65. https://doi.org/10.1144/GSL.QJEG.1975.008.01.02

Lynott, J. (2009). 2008 Matchwood Project summary report. Foth Infrastructure and Environment, Technical Report, 1-29.

Malone, D. H., Stein, C. A., Craddock, J. P., Kley, J., Stein, S., & Malone, J. E. (2016). Maximum depositional age of the Neoproterozoic Jacobsville Sandstone, Michigan: Implications for the evolution of the Midcontinent Rift. *Geosphere*, 12(4), 1271-1282. https://doi.org/10.1130/GES01302.1

Manning, C., & Ingebritsen, S. (1999). Permeability of the continental crust: Implications of geothermal data and metamorphic systems. *Reviews of Geophysics*, 37(1), 127-150. http://dx.doi.org/10.1029/1998RG900002

Marone, C. (1998). The effect of loading rate on static friction and the rate of fault healing during the earthquake cycle. *Nature*, 391(6662), 69-72. http://dx.doi.org/10.1038/34157

Mazdab, F. (2017). Thin section scans. Retrieved from https://www.rockptx.com/thin-section-scans/

McBride, E. F. (2016). Stratigraphy, petrography, and depositional history of the Ignacio Quartzite and McCracken Sandstone Member of the Elbert Formation, southwestern Colorado, U.S.A. *Rocky Mountain Geology*, 51(2), 23-68. https://doi.org/10.2113/gsrocky.51.2.23

McBride, J. H., & Nelson, W. J. (1999). Style and origin of mid-Carboniferous deformation in the Illinois Basin, USA—Ancestral Rockies deformation? *Tectonophysics*, 305(1-3), 249-273. https://doi.org/10.1016/S0040-1951(99)00015-3

McNally, G. H. (1992). Engineering geology of duricrusts. In D. F. Branagan, K. F. Williams (Eds.), *Papers of the Fifth Edgeworth David Day Symposium,* University of Sydney (pp. 89-96). Sydney, Australia: The Edgeworth David Society.

Min, K.-B., Rutqvist, J., Tsang, C.-F., & Jing, L. (2004). Stress-dependent permeability of fractured rock masses: a numerical study. *International Journal of Rock Mechanics and Mining Sciences*, 41(7), 1191-1210. https://doi.org/10.1016/j.ijrmms.2004.05.005

Mitchell, R. L., & Sheldon, N. D. (2016). Sedimentary provenance and weathering processes in the 1.1 Ga Midcontinental Rift of the Keweenaw Peninsula, Michigan, USA. *Precambrian Research*, 275, 225-240. https://doi.org/10.1016/j.precamres.2016.01.017

Moore, D. E., & Rymer, M. J. (2007). Talc-bearing serpentinite and the creeping section of the San Andreas Fault. *Nature*, 448(7155), 795-797. http://dx.doi.org/10.1038/nature06064

Moore, J. C., Moore, G. F., Cochrane, G. R., & Tobin, H. J. (1995). Negative-polarity seismic reflections along faults of the Oregon accretionary prism: Indicators of overpressuring. *Journal of Geophysical Research: Solid Earth*, 100(B7), 12895-12906. https://doi.org/10.1029/94JB02049

Morey, G. B., & Van Schmus, W.R. (1988). Correlation of Precambrian rocks of the Lake Superior region, United States. U.S. Geological Survey Professional Paper, 1241-F.

Morley, C. K., von Hagke, C., Hansberry, R., Collins, A., Kanitpanyacharoen, W., & King, R. (2018). Review of major shale-dominated detachment and thrust characteristics in the diagenetic zone: Part II, rock mechanics and microscopic scale. *Earth-Science Reviews*, 176, 19-50. https://doi.org/10.1016/j.earscirev.2017.09.015

Morrow, C. A., Shi, L. Q., & Byerlee, J. D. (1982). Strain hardening and strength of clay-rich fault gouges. *Journal of Geophysical Research: Solid Earth*, 87(B8), 6771-6780. https://doi.org/10.1029/JB087iB08p06771

Morrow, C. A., Shi, L. Q., & Byerlee, J. D. (1984). Permeability of fault gouge under confining pressure and shear stress. *Journal of Geophysical Research: Solid Earth*, 89(B5), 3193-3200. https://doi.org/10.1029/JB089iB05p03193

National Research Council. (2013). *Induced Seismicity Potential in Energy Technologies*. Washington, DC: The National Academies Press. https://doi.org/10.17226/13355

Nelson, P. H. (1994). Permeability-porosity relationships in sedimentary rocks. *Society of Petrophysicists and Well-Log Analysts*, 35(3), 38-62.

Nelson, P. H. (2009). Pore-throat sizes in sandstones, tight sandstones, and shales. *American Association of Petroleum Geologists Bulletin*, 93(3), 329-340. https://doi.org/10.1306/10240808059

Niemeijer, A., Marone, C., & Ellsworth, D. (2010). Fabric induced weakness of tectonic faults. *Geophysical Research Letters*, 37, L03304. https://doi.org/10.1029/2009GL041689

Ojakangas, R. W., & Dickas, A. B. (2002). The 1.1-Ga Midcontinent Rift System, central North America: sedimentology of two deep boreholes, Lake Superior region. *Sedimentary Geology*, 147(1), 13-36. https://doi.org/10.1016/S0037-0738(01)00185-3

Olgaard, D. L., Urai, J., Dell'Angelo, L. N., Nüesch, R., & Ingram, G. (1997). The influence of swelling clays on the deformation of mudrocks. *International Journal of Rock Mechanics and Mining Sciences*, 34(3), 235.e231-235.e215. https://doi.org/10.1016/S1365-1609(97)00182-2

Ortiz, J. P. (2017). The role of fault-zone architectural elements and basal altered zones on downward pore pressure propagation and induced seismicity in the crystalline basement. (Master's thesis). Socorro, NM: New Mexico Institute of Mining and Technology.

Ortiz, J. P., Person, M. A., Mozley, P. S., Evans, J. P., & Bilek, S. L. (2018). The role of fault-zone architectural elements on pore pressure propagation and induced seismicity. *Groundwater*. https://doi.org/10.1111/gwat.12818

Paasche, Ø., Strømsøe, J. R., Dahl, S. O., & Linge, H. (2006). Weathering characteristics of arctic islands in northern Norway. *Geomorphology*, 82(3), 430-452. https://doi.org/10.1016/j.geomorph.2006.05.016

Pain, C., Chan, R., Craig, M., Hazell, M., Kamprad, J. & Wilford, J. (1991). RTMAP BMR Regolith Database Field Handbook, BMR Record, 1991/29: 125pp.

Pang, M., & Nummedal, D. (1995). Flexural subsidence and basement tectonics of the Cretaceous Western Interior basin, United States. *Geology*, 23(2), 173-176. https://doi.org/10.1130/0091-7613(1995)023<0173:FSABTO>2.3.CO;2

Parnell, J. (1999). Petrographic evidence for emplacement of carbon into Witwatersrand conglomerates under high fluid pressure. *Journal of Sedimentary Research*, 69(1), 164-170. https://doi.org/10.2110/jsr.69.164

Petersen, M. D., Mueller, C., Moschetti, M. P., Hoover, S. M., Llenos, A. L., Ellsworth, W. L., Michael, A. J., Rubinstein, J. L., McGarr, A. F., & Rukstales, K. S. (2016). Seismic-hazard forecast for 2016 including induced and natural earthquakes in the central and eastern United States. *Seismological Research Letters*, 87(6), 1327-1341. https://doi.org/10.1785/0220160072

Petford, N., & McCaffrey, K. (2003). Hydrocarbons in crystalline rocks: an introduction. In N. Petford, K. McCaffrey (Eds.), *Hydrocarbons in crystalline rocks*, *Geological Society, London, Special Publications* no *214* (pp. 1-5). London, ENG: The Geological Society London. https://doi.org/10.1144/gsl.sp.2003.214.01.01

Raffensperger, J. P., & Garven, G. (1995). The formation of unconformity-type uranium ore deposits; 2. Coupled hydrochemical modeling. *American Journal of Science*, 295(6), 639-696. https://doi.org/10.2475/ajs.295.6.639

Ranjram, M., Gleeson, T., & Luijendijk, E. (2015). Is the permeability of crystalline rock in the shallow crust related to depth, lithology or tectonic setting? *Geofluids*, 15(1-2), 106-119. https://doi.org/10.1002/9781119166573.ch12

Riber, L., Dypvik, H., Sørlie, R., & Ferrell Jr, R. E. (2016). Clay minerals in deeply buried paleoregolith profiles, Norwegian North Sea. *Clays and Clay Minerals*, 64(5), 588-607. https://doi.org/10.1346/CCMN.2016.064036

Riber, L., Dypvik, H., Sørlie, R., Naqvi, S. A. A.-E.-M., Stangvik, K., Oberhardt, N., & Schroeder, P. A. (2017). Comparison of deeply buried paleoregolith profiles, Norwegian North Sea, with outcrops from southern Sweden and Georgia, USA—Implications for petroleum exploration. *Palaeogeography, Palaeoclimatology, Palaeoecology*, 471, 82-95. https://doi.org/10.1016/j.palaeo.2017.01.043

Rice, J. R. (1992). Fault stress states, pore pressure distributions, and the weakness of the San Andreas Fault. In B. Evans & T.-f. Wong (Eds.), *International Geophysics, Fault mechanics and transport properties of rocks* (Vol. 51, pp. 475-503). San Diego, CA: Academic Press Harcourt Brace Jovanovich.

Rubinstein, J. L., Ellsworth, W. L., McGarr, A., & Benz, H. M. (2014). The 2001–present induced earthquake sequence in the Raton Basin of northern New Mexico and southern Colorado. *Bulletin of the Seismological Society of America*, 104(5), 2162-2181. https://doi.org/10.1785/0120140009

Rubinstein, J. L., & Mahani, A. B. (2015). Myths and facts on wastewater injection, hydraulic fracturing, enhanced oil recovery, and induced seismicity. *Seismological Research Letters*, 86(4), 1060-1067. https://doi.org/10.1785/0220150067

Saffer, D. M., & Marone, C. (2003). Comparison of smectite- and illite-rich gouge frictional properties: application to the updip limit of the seismogenic zone along subduction megathrusts. *Earth and Planetary Science Letters*, 215(1), 219-235. https://doi.org/10.1016/S0012-821X(03)00424-2

Schulz, K. J., & Cannon, W. F. (2007). The Penokean orogeny in the Lake Superior region. *Precambrian Research*, 157(1), 4-25. https://doi.org/10.1016/j.precamres.2007.02.022

Shapiro, S. A., & Dinske, C. (2009). Fluid-induced seismicity: Pressure diffusion and hydraulic fracturing. *Geophysical Prospecting*, 57(2), 301-310. https://doi.org/10.1111/j.1365-2478.2008.00770.x

Sibson, R. H. (1974). Frictional constraints on thrust, wrench and normal faults. *Nature*, 249, 542-544. https://doi.org/10.1038/249542a0

Sibson, R. H. (1994). Crustal stress, faulting and fluid flow. In J. Parnell (Ed.), *Geofluids: Origin, migration, and evolution of fluids in sedimentary basins, Geological Society, London, Special Publications no. 78* (pp. 69-84). London, ENG: The Geological Society London. https://doi.org/10.1144/gsl.sp.1994.078.01.07

Sims, P. K., Card, K. D., Morey, G. B., & Peterman, Z. E. (1980). The Great Lakes tectonic zone—a major crustal structure in central North America. *Geological Society of America Bulletin*, 91(12), 690-698. https://doi.org/10.1130/0016-7606(1980)91<690:TGLTZA>2.0.CO;2

Sloss, L. L. (1963). Sequences in the cratonic interior of North America. *Geological Society of America Bulletin*, 74(2), 93-114.

Smith, L., Forster, C. B., & Evans, J. P. (1990). Interaction between fault zones, fluid flow and heat transfer at the basin scale. In S. Newman, I. Neretnieks, *Hydrogeology of low permeability environments, International Association of Hydrological Sciences selected papers in hydrogeology* (Vol. 2, pp. 41-67). Washington, DC: International Association of Hydrogeologists.

Stein, C. A., Kley, J., Stein, S., Hindle, D., & Keller, G. R. (2015). North America's Midcontinent Rift: When rift met LIP. *Geosphere*, 11(5), 1607-1616. https://doi.org/10.1130/GES01183.1

Stein, C. A., Stein, S., Merino, M., Randy Keller, G., Flesch, L. M., & Jurdy, D. M. (2014). Was the Midcontinent Rift part of a successful seafloor-spreading episode? *Geophysical Research Letters*, 41(5), 1465-1470. https://doi.org/10.1002/2013GL059176

Stober, I., & Bucher, K. (2015). Hydraulic conductivity of fractured upper crust: insights from hydraulic tests in boreholes and fluid-rock interaction in crystalline basement rocks. *Geofluids*, 15(1-2), 161-178. https://doi.org/10.1111/gfl.12104

Taylor, G., & Eggleton, R. A. (2001). *Regolith geology and geomorphology*. Baffins Lane, England: J. Wiley & Sons, Ltd.

Tong, K., Zhao, C., LÜ, Z., Zhang, Y., Zheng, H., Xu, S., Wang, J., & Pan, L. (2012). Reservoir evaluation and fracture characterization of the metamorphic buried hill reservoir in Bohai Bay Basin. *Petroleum Exploration and Development*, 39(1), 62-69. https://doi.org/10.1016/S1876-3804(12)60015-9

Townend, J., & Zoback, M. D. (2000). How faulting keeps the crust strong. *Geology*, 28(5), 399-402. https://doi.org/10.1130/0091-7613(2000)28<399:HFKTCS>2.0.CO;2

Trice, R. (2014). Basement exploration, West of Shetlands: progress in opening a new play on the UKCS. In S. J. Cannon, D. Ellis (Eds.), *Hydrocarbon exploration to exploitation west of Shetlands*, *Geological Society London, Special Publications no. 397* (pp. 81-105). London, ENG: The Geological Society London. https://doi.org/10.1144/sp397.3

Ujiie, K., & Tsutsumi, A. (2010). High-velocity frictional properties of clay-rich fault gouge in a megasplay fault zone, Nankai subduction zone. *Geophysical Research Letters*, 37, L24310. https://doi.org/10.1029/2010GL046002

Ulmer, D. S., & Laury, R. L. (1984). Diagenesis of the Mississippian Arroyo Penasco Group, north-central New Mexico. In W. S. Baldridge, P. W. Dickerson, R. E. Riecker, J. Zidek (Eds.), *New Mexico Geological Society, Rio Grande Rift: Northern New Mexico*, *guidebook 35*, *1984* (pp. 91-100). Socorro, NM: New Mexico Geological Society, Inc.

U.S. Geological Survey. (2010). Montezuma quadrangle, New Mexico. The National Map, U.S. Topo 7.5 Minute Series. Reston, VA: U.S. Geological Survey.

Vandeginste, V., Swennen, R., Gleeson, S. A., Ellam, R. M., Osadetz, K., & Roure, F. (2005). Zebra dolomitization as a result of focused fluid flow in the Rocky Mountains Fold and Thrust Belt, Canada. *Sedimentology*, 52(5), 1067-1095. https://doi.org/10.1111/j.1365-3091.2005.00724.x

Walker, F. D. L. (1990). Ion microprobe study of intragrain micropermeability in alkali feldspars. *Contributions to Mineralogy and Petrology*, 106(1), 124-128. https://doi.org/10.1007/BF00306413

Walker, F. D. L., Lee, M. R., & Parsons, I. (1995). Micropores and micropermeable texture in alkali feldspars: geochemical and geophysical implications. *Mineralogical Magazine*, 59(3), 505-534. https://doi.org/10.1180/minmag.1995.059.396.12

Walsh, F. R., & Zoback, M. D. (2015). Oklahoma's recent earthquakes and saltwater disposal. *Science Advances*, 1(5), e1500195. https://doi.org/10.1126/sciadv.1500195

Wieder, M., & Yaalon, D. H. (1974). Effect of matrix composition on carbonate nodule crystallization. *Geoderma*, 11(2), 95-121. https://doi.org/10.1016/0016-7061(74)90010-X

Wintsch, R. P., Christoffersen, R., & Kronenberg, A. K. (1995). Fluid-rock reaction weakening of fault zones. *Journal of Geophysical Research: Solid Earth*, 100(B7), 13021-13032. https://doi.org/10.1029/94JB02622

Worden, R., David L. Walker, F., Parsons, I., & L. Brown, W. (1990). Development of microporosity, diffusion channels and deuteric coarsening in perthitic alkali feldspars. *Contributions to Mineralogy and Petrology*, 104(5), 507-515. https://doi.org/10.1007/BF00306660

Younes, A. I., Engelder, T., & Bosworth, W. (1998). Fracture distribution in faulted basement blocks: Gulf of Suez, Egypt. In M. P. Coward, T. S. Daltaban, H. Johnson (Eds.), *Structural geology in reservoir characterization*, *Geological Society, London, Special Publications no. 127* (pp. 167-190). London, ENG: The Geological Society London. https://doi.org/10.1144/gsl.sp.1998.127.01.13

Zartman, R. E., Nicholson, S. W., Cannon, W. F., & Morey, G. B. (1997). U – Th – Pb zircon ages of some Keweenawan Supergroup rocks from the south shore of Lake Superior. *Canadian Journal of Earth Sciences*, 34(4), 549-561. https://doi.org/10.1139/e17-044

Zhang, Y., Edel, S. S., Pepin, J., Person, M., Broadhead, R., Ortiz, J. P., Bilek, S. L., Mozley, P., & Evans, J. P. (2016). Exploring the potential linkages between oil-field brine reinjection, crystalline basement permeability, and triggered seismicity for the Dagger Draw Oil field, southeastern New Mexico, USA, using hydrologic modeling. *Geofluids*, 16(5), 971-987. https://doi.org/10.1111/gfl.12199

Zhang, Y., Person, M., Rupp, J., Ellett, K., Celia, M. A., Gable, C. W., Bowen, B., Evans, J., Bandilla, K., Mozley, P., Dewers, T., & Elliot, T. (2013). Hydrogeologic Controls on Induced Seismicity in Crystalline Basement Rocks Due to Fluid Injection into Basal Reservoirs. *Groundwater*, 51(4), 525-538. https://doi.org/10.1111/gwat.12071

Zoback, M. D., Zoback, M. L., Mount, V. S., Suppe, J., Eaton, J. P., Healy, J. H., Oppenheimer D., Reasenbery, P., Jones, L., Raleigh C. B., Wong, I. G., Scott, O., & Wentworth, C. (1987). New Evidence on the State of Stress of the San Andreas Fault System. *Science*, 238(4830), 1105-1111. https://doi.org/10.1126/science.238.4830.1105